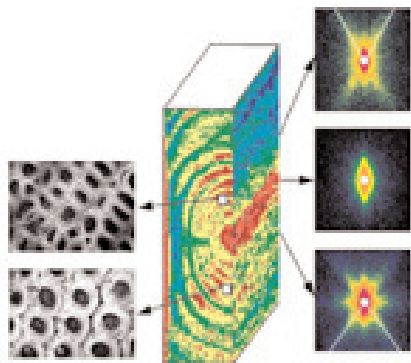


FIBRE DIFFRACTION

REVIEW

Software Development for Fibre Diffraction

A CCP13 / NCD Publication



11th Annual Fibre Diffraction and Non-Crystalline Diffraction Workshop

19th-21st June 2002

Keele University

Speakers include:

M. H. F. Wilkins FRS (tbc)	King's College, London
W. Fuller	Keele, UK
S. Arnott FRS	ICRF / Imperial, UK
J. Blackwell (tbc)	Case Western, USA
D. Caspar	Florida, USA
K. Gardner	DuPont, USA
H. Gleeson	Manchester, UK
G. Grossmann	Daresbury, UK
I. Hamley	Leeds, UK
D. Kirschner	Boston, USA
N. Koubassova	Moscow, Russia
P. Langan	Los Alamos, USA
A. Mahendrasingam	Keele, UK
D. A. Marvin	Cambridge, UK
J. Penfold	Rutherford, UK
M. J. Rodman	Daresbury, UK
A. J. Ryan	Sheffield, UK
D. Sivia	Rutherford, UK
J. Squire	Imperial, UK
N. Terrill	Daresbury, UK
V. Urban	ESRF, France
L. Yu	NIH Washington, USA

For further information and registration,
see the web pages at
<http://www ccp13.ac.uk>
or contact a.mutch@dl.ac.uk

(supported by CCP13, DARTS and Daresbury Laboratory)

Contents, Cover Caption and Production	1
The CCP13 Committee Members	2
Chairman's Message	3
Summary of Available CCP13/NCD Software	5
New CCP13 Members	6

Meeting Reports

Alpbach Workshop	8
223rd National American Chemical Society	10

Technical Reports

Current limits of x-ray microdiffraction in soft condensed matter experiments, C. Riek <i>et al</i>	11
---	----

Mini-Reviews

Scattering studies of plant cell walls, A. M. Donald and O. M. Astley	19
Characterising natural fibre composites with hierarchical structure, P. Fratzl	31
Recent insights into three-dimensional molecular packing structure of native type I collagen, J.P.R.O. Orgel, <i>et al</i>	40

Contributed Articles

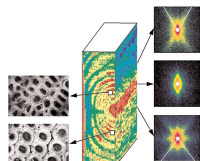
Real time SAXS/stress-strain studies of thermoplastic polyurethane - A fibre diffraction approach to a non-crystalline material, D. J. Blundell, <i>et al</i>	50
Structure determination from screw-disordered fibres, R. P. Millane and J. L. Eads	57

10th Annual Workshop Prize-Winning Posters

Evidence of spinodal decomposition in semi-crystalline polymers, E. L. Heeley, <i>et al</i>	63
Folded-back solution structure of monomeric Factor H of human complement by scattering, ultracentrifugation and modelling, M. Aslam and S. J. Perkins	72
10th Annual Workshop Abstracts	78
Forthcoming Meetings	96
<i>Fibre Diffraction Review</i> : Instructions to Authors	97

Front Cover Image

SAXS patterns from a spruce branch (Peter Fratzl)



Newsletter Production

Editor: Prof. J. Squire, Biological Structure and Function Section, Biomedical Sciences Division, Imperial College, London SW7 2AZ.

Production: Dr M.J. Rodman, Daresbury Laboratory, Warrington WA4 4AD.

The CCP13 Committee Members (As at April 2002)

Chairman

Dr Trevor Forsyth (to 2002),
Institut Laue-Langevin, BP 156 F-38042, Grenoble Cedex 9, France, and Physics Dept, Keele University, Staffordshire ST5 5BG,
Phone +33 4 (0) 76207158 **Fax** +33 4 (0) 76483906 **Email** tforsyth@ill.fr

Prof. John Squire (From June 2002)
Biomedical Sciences Division, Imperial College, London SW7 2AZ,
Phone 0207 594 3185, **Fax** 0207 594 3169, **Email** j.squire@ic.ac.uk

Research Assistants (Ex Officio)

Dr Matthew Rodman (from January 2001),
Daresbury Laboratory, Daresbury, Warrington WA4 4AD,
Phone 01925 603626 , **Email** m.j.rodman@dl.ac.uk

Dr David Dover,
Biomedical Sciences Division, Imperial College, London SW7 2AZ,
Phone 0207 4331071, **Email** sdd@doversoft.co.uk

Dr Andrew He,
Biomedical Sciences Division, Imperial College, London SW7 2AZ,
Email andrew.he@ic.ac.uk

Ganeshalingam Rajkumar,
Biomedical Sciences Division, Imperial College, London SW7 2AZ,
Email g.rajkumar@ic.ac.uk

Dr Jane Crawshaw,
Polymer Group, Department of Materials Science and Metallurgy, University of Cambridge, Pembroke St., Cambridge CB2 3QZ
Phone 01223 334335, **Email** jc10027@hermes.cam.ac.uk

Members

Dr David Blundell (to 2002)
Physics Department, Keele University, Keele, Staffordshire, ST5 5BG,
Phone 01782 583330

Dr Patrick Fairclough (to 2002)
Department of Chemistry, The University of Sheffield, Dainton Building, Brookhill, Sheffield, S3 7HF,
Phone 0114 2229411 **Fax** 0114 2229303, **Email** p.fairclough@sheffield.ac.uk

Dr Mike Ferenczi (to 2004)
Biomedical Sciences Division, Imperial College, London SW7 2AZ,
Phone 0207 594 3139, **Fax** 0207 594 3169, **Email** m.ferenczi@ic.ac.uk

Dr Steve King (to 2004)
Rutherford Appleton Laboratory, Chilton, Didcot, OX11 0QX,
Phone 01235 446437, **Fax** 01235 445720, **Email** s.m.king@rl.ac.uk

Dr Tim Wess (to 2002)
Department of Biological and Molecular Sciences, University of Stirling, Stirling, FK9 4LA,
Phone 01786 467775, **Fax** 01786 464994 **Email** tzw3@stir.ac.uk

Prof. Alan Windle FRS (to 2004)
Department of Materials Science and Metallurgy, University of Cambridge, Pembroke Street, Cambridge CB2 3QZ.
Phone 01223 334335 **Fax** 01223 335637, **Email** ahw1@cam.ac.uk

Prof. Struther Arnott FRS (to 2004)
Biomedical Sciences Division, Imperial College, London SW7 2AZ,
Phone 0207 594 3185, **Fax** 0207 594 3018, **Email** s.arnott@ic.ac.uk

Members (Co-opted)

Dr Greg Diakun
Daresbury Laboratory, Daresbury, Warrington WA4 4AD,
Phone 01925 603343 **Email** g.diakun@dl.ac.uk

Dr Tom Irving
CSRRI, Dept BCPS, Illinois Institute of Technology, 3101 s. Dearborn, Chicago IL. 60616, USA.
Phone (312) 567-3489 **Fax** (312) 567-3494 **Email** irving@biocat1.iit.edu

Dr Rob Lewis
Daresbury Laboratory, Daresbury, Warrington WA4 4AD
Phone 01925 603544 **Email** r.a.lewis@dl.ac.uk

Dr Geoff Mant
Daresbury Laboratory, Daresbury, Warrington WA4 4AD
Phone 01925 603169 **Email** g.r.mant@dl.ac.uk

Prof. Rick Millane
Dept of Electrical and Computer Engineering, University of Canterbury, Christchurch, New Zealand.
Email rick@elec.canterbury.ac.nz

Dr Keiichi Namba
Matsushita Electric Industrial Co. Ltd., 3-4 Hikaridai, Seika 619-0237, Japan.
Phone 81-774-98-2543 **Fax** 81-774-98-2575 **Email** keiichi@crl.mei.co.jp

Prof. Gerald Stubbs
Dept of Molecular Biology, Vanderbilt University, 2200 West End Avenue, Nashville, TN 37235
Phone (615) 322-7311 **Email** stubbs@ctrvax.vanderbilt.edu

Chairman's Message

The past year has seen many important developments for CCP13. Three appointments have just been made to fill the posts funded by the recent BBSRC/EPSRC grant. In addition to Matthew Rodman, who continues his joint CCP13/NCD appointment based at Daresbury Laboratory, we welcome Jane Crawshaw, as well as Rajkumar Ganeshalingam (Raj) and Andrew He to the project. Jane is based at Cambridge and involved principally in the development of software for the analysis of synthetic polymer systems. Both Raj and Andrew are at Imperial College, with Raj having a particular involvement in data extraction procedures and Andrew taking on the task of molecular modelling for biological systems. It is also a great pleasure to welcome the involvement of David Dover in CCP13 modelling activity. The appointment of new staff has also allowed a redistribution of some of the administrative tasks - the workload associated with the organisation of the annual meeting, Fibre Diffraction Review and web site has gradually increased over the years and in recent times have all been shouldered by Matthew. As part of this, it is planned that the bulk of the work associated with the production of Fibre Diffraction Review will shift to Imperial College.

With the new personnel in post, CCP13 is poised to deliver high quality software solutions that will be badly needed by the Fibre Diffraction and Non

Crystalline Diffraction (NCD) communities as the field continues to expand. This growth is self evident: at the same time as rapid developments in biochemistry, molecular biology, and polymer chemistry are producing new types of problem, major developments in instrumentation are widening the scope of experimental methods and therefore the range of samples that can be studied. For synchrotron x-ray studies, in addition to beamlines 2.1, 16.1 and 14.1 at the SRS, the ESRF microfocus beamline ID13 can be used to study fibres as small as ~2mm diameter, while the high flux beamline ID2 provides for simultaneous low and high angle fibre diffraction experiments. At the Institut Laue Langevin (ILL) the EPSRC has just funded a major development for high-angle neutron fibre diffraction on instrument D19, opening up completely new areas. In parallel with this, an initiative for the preparation of deuterium labelled samples has occurred at the ILL with the award of a major grant (funded through Keele) from EPSRC for the support of a number of flagship projects (including three neutron fibre diffraction projects) that will exploit a new Deuteration Laboratory at the ILL & the EMBL Grenoble Outstation. The future also promises further major development with the construction of DIAMOND and also of the second target station at ISIS.

The implications of these developments for CCP13

are very significant. Not only are there continuous requirements for CCP13 to maintain compatibility with the various data formats that arise from the different facilities, but as the range of experiments extends, there is also a clear need for data extraction software to be able to cope with many different types of sample disorder. In addition to the "standard" cases (eg solutions/amorphous polymer, crystalline diffraction, continuous diffraction), there exist many situations where complex types of sample order/disorder make data extraction protocols more difficult. Examples include diffraction from "doubly oriented" samples (see previous issue of Fibre Diffraction Review) or other situations where diffraction may contain complex mixtures of crystalline and continuous diffraction (see paper by Millane et al, this issue). On the molecular modelling side it is unlikely that the needs of CCP13 will be accommodated by any single modelbuilding/refinement package. For some problems it is clear that programs such as SHELX are very effective. For others, programs such as X-PLOR are more suitable - fibre diffraction functionality has already been built into a modified version of X-PLOR and will be carried through to an analogous version of CNS. At the same time the linked atom least squares (LALS) programme is being rebuilt to include a user friendly front end - with the particular involvement of David Dover.

Over and above the scientific issues that form the main brief of CCP13 activity, the technical plan for the CCP13 software is to move towards a single Java based interface that will permit an easy route from data extraction through to model building and refinement. The large increases in computing power that we all now take so much for granted mean that the development of such an interface for CCP13 should not be restricted to Unix based platforms and that considerable emphasis should be placed on making all programs operable on standard Windows and Macintosh desktop/laptop machines.

It has been very pleasing to see the steady build up of activity within the CCP13 community over the last four years or so. The last CCP13 conferences at St. Andrew's, Sheffield, and Stirling Universities have been very well attended (with steadily increasing numbers of overseas delegates), with extremely interesting programmes. At the time of writing, the number of registrations for the next meeting at Keele makes it look as though the same will be true in June 2002. See you there!

Trevor Forsyth
Institut Laue Langevin, Grenoble
and
Keele University

19th April 2002

Summary of Available CCP13/NCD Software

Program	Description
XOTOKO	1-D data manipulation
BSL	2-D data manipulation
v2A	vax to unix data conversion
A2V	unix to vax data conversion
OTCON	ascii to otoko data conversion
RECONV	otoko to ascii data conversion
TIFF2BSL	image plate (tiff) to bsl conversion
BSL2TIFF	bsl to tiff conversion
i2A	ieee to ansi data conversion (DEC)
XCONV	file format conversion (GUI-driven)
XFIT	1-D fitting and plotting (GUI-driven)
XFIX	fibre pattern analysis (GUI-driven)
CONV	file format conversion (cmd line)
FTOREC	reciprocal space transformation
LSQINT	2-D integration and background fitting
CORFUNC	correlation function analysis
SAMPLE	Fourier-Bessel smoothing
FDSCALE	scaling and merging of intensities
FD2BSL	intensity to bsl conversion

Program	Solaris 2.7	Irix 6.2	OSF 3.2	Linux
XOTOKO	28/11/97	30/05/96	29/04/97	-
BSL	02/05/97	21/03/97	27/04/97	-
v2A	19/05/95	-	-	-
A2V	19/05/95	-	-	-
OTCON	06/06/95	08/07/94	-	08/05/97
RECONV	06/06/95	31/10/94	-	08/05/97
TIFF2BSL	01/2002	01/2002-	-	01/2002-
BSL2TIFF	21/03/97	-	-	-
i2A	n/a	n/a	29/04/97	02/05/97
XCONV	04/06/99	04/06/99	-	04/06/99 *
XFIT	10/07/98	10/07/98	10/07/98	10/07/98 *
XFIX	09/04/99	09/04/99	09/04/99	09/04/99 *
CONV	09/04/99	09/04/99	09/04/99	09/04/99
FTOREC	12/04/99	12/04/99	12/04/99	12/04/99
LSQINT	12/04/99	12/04/99	12/04/99	12/04/99
CORFUNC	26/10/95	26/10/95	-	26/10/95
SAMPLE	05/11/96	04/11/96	04/11/96	04/11/96
FDSCALE	05/11/96	04/11/96	04/11/96	04/11/96
FD2BSL	05/11/96	04/11/96	04/11/96	04/11/96

The tables list the currently distributed CCP13/NCD programs, available as executable modules. The dates refer to the last creation of the executable.

A LOQ2BSL conversion program, for ISIS neutron data to BSL format, is also available for Solaris platforms.

* These programs have been tested on Slackware 3.4, SuSE 5.3 and RedHat 5.0 distributions of Linux.

New CCP13 Members

Dr Jane Crawshaw

Jane studied for her PhD at the Department of Materials Science and Metallurgy in Cambridge where she was supervised by Ruth Cameron. Her brief was to investigate how hydration, dehydration and mercerisation affect the microstructure of cellulose textile fibres. Small angle X-ray scattering was used to make dynamic observations of structural changes. The water composition of hydrated fibres was investigated using small angle neutron scattering. The X-ray work was done at the Daresbury Laboratory, and the neutron scattering at the Rutherford Appleton Laboratory.

Next, Jane worked as a PDRA for Athene Donald at The Cavendish Laboratory in Cambridge. Once again she used small angle X-ray scattering, this time to investigate deformation mechanisms in rubber toughened PMMA.



Now Jane is moving into the field of polymer modelling working as a CCP13 funded PDRA for Alan Windle at the Materials Science Department in Cambridge.

Dr Andrew He

Andrew He is both a software engineer and a computer scientist with a wealth of academic and commercial experience and rich hands-on technical skills to draw upon. In the middle 80s, he started working on designing and developing real-time control systems, electronic systems and medical equipment using microprocessors, assembly language and C language. During the 90s, he was an experienced computer engineer with solid commercial experience in C/C++, Java, e-commerce, real-time data visualization, biomedical signal processing and image processing. More recently, Andrew has worked on the real-time message-oriented middleware system and Java message service. As a computer scientist, his research interests include parallel and distributed computing techniques, design and analysis of string algorithms and algorithms for molecular sequences, as well as combinatorial optimisation, global optimisation and modelling for the biological molecular structures. Since March 2002, he has been a CCP13-funded research associate in the Biological Structure and Function Section, Biomedical Science Division, Imperial College of Science, Technology & Medicine, London. His interests within CCP13 are



to update and develop programs for modelling biological systems, both at the molecular level using software such as LALS (Smith, P.J.C. & Arnott, S., *Acta Cryst.* (1978) A34, 3-11) and at the molecular assembly level using programs like MOVIE (Hudson, L. et al., 1997, *J. Mol. Biol.* 273, 440-455). Andrew will be involved along with Matthew Rodman in producing the CCP13 Journal "Fibre Diffraction Review".

Ganeshalingam Rajkumar

Ganeshalingam Rajkumar ("Raj") received his B.Sc.Eng. degree in Electrical Engineering from the University of Moratuwa, Sri Lanka, in 1999 and his M.Sc. degree in Information Technology from Loughborough University, UK, in October 2001. His expertise is in stereo image compression, video coding, software engineering and programming. In March 2002 he joined Imperial College as a research assistant funded by the CCP13 project. His research interests within CCP13 include updating and developing programs for stripping and modelling fibre X-ray diffraction patterns, prior to structure determination. He will be responsible for the CCP13 mirror website at Imperial College and will be the main CCP13 contact in matters of data extraction from observed diffraction patterns (g.rajkumar@ic.ac.uk).



Meeting Reports

Alpbach Workshop "Coiled-Coils, Collagen and Co-Proteins"

A Workshop on "Coiled-Coils, Collagen and Co-Proteins" is held every four years at the Boglerhof Hotel in Alpbach, Austria. The latest of these Workshops was held from September 16-21, 2001. Alpbach is a small Tyrolean town set between beautiful hills and mountains. In winter, it is a favourite spot for skiers. At other times it is an ideal place for walks, hill climbing, or taking rides on the cable car to experience the spectacular mountaintop views. The Böglerhof Hotel is well known for its friendly ambience, its very comfortable amenities and its rather too tempting cuisine. The Workshop consisted of a judicious mix of morning and evening sessions of talks and discussions, with the afternoons being free for more informal chats over walks or a glass of beer.

As on previous occasions the aim of the Workshop was to foster interaction between research workers active in all aspects of the structure and function of fibrous proteins. A particular feature of the Alpbach Workshops has been the deliberate attempt to bring together scientists who work on intracellular proteins with those whose work centres on the extracellular. The "membrane" has often proved to be a substantial barrier, not only at the cellular level, but also at the research level where it appears to inhibit collaboration and understanding between scientists. The Alpbach Workshops have been designed to lower the energy barrier between these different communities and in many ways they have achieved their aims. The cross-fertilisation of ideas that has arisen from the formal and informal discussions at the Workshops has far exceeded expectations. Alpbach 2001 was no exception.

The 2001 Alpbach Workshop was held very soon after the terrorist attacks on the World Trade Center in New York and on the Pentagon in Washington DC. Many scientific meetings were cancelled around that time and, indeed, many others were cancelled in the following months. The Alpbach Fibrous Protein Workshop, however, carried on virtually as planned and proved to be just as successful as its predecessors. The attendance of delegates was in excess of 90% of those who had registered - a tremendous tribute to all who came, especially those who made major efforts to fly from the USA by

whatever route they could find. The latter faced some real challenges, but showed great determination to participate. Very few decided not to come. This really is a great tribute to scientists in general and to the individuals concerned in particular in that they refused to be intimidated.

As with previous Alpbach Workshops, we selected an eminent scientist as our Guest of Honour to whom we could pay special tribute. This time we were fortunate to have with us Jürgen Engel from the Biozentrum in Basel. Jürgen has established himself as a truly international figure in the fields of connective tissue and a-fibrous protein research. Not only is he a notable scientist, but he is a very special person - a humanitarian who really cares about the way society treats all its citizens. It was a privilege for all us to have him with us at Alpbach and to hear his presentation.

The main scientific sessions were carefully organized by the nominated Chairpersons to be up-to-the-minute reflections of their particular topics. Richard Kammerer (Manchester, UK) chaired the first session on "Coiled-Coils/ Triggers" including talks from Dek Woolfson and Andrei Lupas. On Monday morning Ueli Aebi (Biozentrum, Basel) chaired a session on "Coiled-Coil Structures: Crystals and Models" with Peter Burkhard, David Helfman, Bob Hodges, Marcus Meier, Jenny Shipway and Valeria de Marco. At the start of the evening session, because he had to leave early in the Workshop, Reinhard Jahn gave an interesting talk on vesicle fusion complexes. There followed two muscle sessions chaired by John Squire (Imperial College, London). The first on Monday evening covered "Myosin Filaments, including Titin, C-protein and Paramyosin" with talks by John, Siegfried Labeit and Mathias Gautel. The second on Tuesday morning was on "Actin Filaments, including Tropomyosin, Troponin, Nebulin, a-actinin" with talks by Toshiro Oda, Robin Maytum, Wolfgang Linke, Olga Mayans, Henk Granzier, Annalisa Pastore, Pradeep Luther and Dieter Furst. We then concentrated on Tuesday evening on "3-Strand Coiled-Coils and Non-Muscle Actin Motors" chaired by John Kendrick-Jones, with Dieter Furst, Steve Winder, Martin Bahler and Andrew



Juergen Engel (left) starting to open his Guest of Honour 'Gift' from one of the organisers David Parry.

Sutherland-Smith. On Wednesday morning we moved on from myosin motors to a session on "Microtubules and Non-Myosin Motors" chaired by Eckhard Mandelkow (Max Planck, Hamburg) with Michel Steinmetz, Keiichi Namba and Andy Hoenger. After this long series on coiled-coils and motor proteins in their great varieties we then moved away from motors with an evening session chaired by Alasdair Steven (NIH, Washington) on "Coiled-Coils in Molecular Recognition/ Beta Structures" with Anna Mitraki, Vadim Mesyazhinov, Mark van Raaij, Ismael Moraefi and Andrei Lupas.

By this time it was Thursday, which started with sessions on "Intermediate filaments" chaired jointly by Peter Steinert (NIH, Washington) and David Parry (Massey University, New Zealand). Apart from their own contributions, their main speakers included, in the first part of the session, Sergei Strelkov, Harald Herrmann and Laurent Kreplak, and in an early



Juergen Engel (left) responding to his introduction as the Guest of Honour at the Alpbach Workshop, with the organisers David Parry (right) and John Squire.

afternoon session, Gerhard Wiche, Sakuhei Fujiwara, Roland Foisner and Joseph Gruenbaum. We then enjoyed Juergen Engel's "Special Lecture", when he spoke about an unusual collagen in Hydra. After the lecture we indulged in what the Boglerhof Hotel call a "Romantik Dinner", with splendid food served along with live musical accompaniment in a very friendly atmosphere. On Friday we came back to other serious business with two sessions on "Collagen and Connective Tissue". The first was chaired by Andrew Miller (then at the University of Stirling, Scotland) who had as speakers Kenji Okuyama, Hans Peter Bachinger, David Hulmes, Tim Wess and Carlo Knupp. The afternoon session, kindly chaired at short notice by David Hulmes (Institute of Biology and Chemistry of Proteins, Lyon, France) had contributions from Ruggero Tanni, Barry Oakes and John Ramshaw.

Many of the fascinating fibrous protein studies reported at the Workshop are being collected in a special issue of the Journal of Structural Biology to be published in the summer of 2002. The previous Workshop gave rise to a similar, very successful, special issue (J. Structural Biology 122, 1998). We are grateful to the publishers of the Journal, Academic Press, as well as to the Biological Structure and Function Section, Faculty of Medicine, Imperial College, London, UK for generously sponsoring the Workshop.

In summary, although we very much missed those who in the end could not come, the Workshop proved to be a splendid occasion, both scientifically and socially, in which many new friendships and collaborations were developed. It was agreed that there should definitely be another "Coiled-Coils, Collagen and Co-Proteins" Workshop in September, 2005. Make a note in your diaries.

John Squire

223rd National American Chemical Society Meeting, Orlando, Florida, April 2002

223rd National American Chemical Society Meeting, Orlando, Florida, April 2002

The 223rd national ACS meeting was held in the Orange County Convention Centre on International Drive in Orlando. With more than 11,000 delegates and countless parallel sessions, the meeting covered a huge diversity of scientific activity. Of particular interest to the fibre diffraction and NCD communities were the sessions connected to the Division of Polymer Chemistry organised by John Blackwell (Case Western Reserve University) and Kenn Gardner (Dupont, USA). The sessions were very well organised and the quality of the presentations was extremely high throughout.

The topics covered a wide range of technical issues in fibre/polymer diffraction as well as recent scientific results. Perhaps the most striking thing about the meeting was the fact that just about every presentation highlighted the importance of combining different techniques in probing structure/function/property relationships. In addition to a number of presentations illustrating how x-ray, neutron and electron diffraction methods can provide powerful insights into polymer structure (Takahashi, Langan, Forsyth, Puigalli, Martin) there were many talks describing how results from electron microscopy (Namba)/spectroscopy are brought to bear on these problems. The presentation from Mahendrasingam on biaxial deformation of polymers also illustrated the importance of being able to record both low and high angle data simultaneously (as did that of Baltá Calleja). In the Biopolymers session Kirschner and Mitraki both gave exciting reports on amyloid structures, and Zugenmaier, Chandrasekaran, and French talked

about fibre diffraction work on polysaccharides. There were also some excellent presentations in the Structure Evolution session. Harrison's presentation on Teaching Diffraction Methods with Flash Movies was very well received as were the talks of Kornfield (shear induced crystallisation), and Chvalun (deformation studies of polyethylene). The talk of Riekel on Kevlar fibres and of the variation of crystallite orientation and of the skin-core effect was a reminder of the remarkable scope of microbeam x-ray diffraction studies that are now possible. The Polymer Blends session also contained some excellent talks: Ryan and Xu talked about crystallisation in block copolymers and there were interesting presentations from Cheng, Borsali, Zhu and Kwon. In the final sessions on Structure Determination there were presentations from Farmer, Marchessault, Lotz, Winokur, Dosiere, Cebe, Ran, and Burger.

Trevor Forsyth



Left to right: Trina Gardner, Kenn Gardner, Anna Mitraki, Dan Kirschner, Trevor Forsyth wield minigolf clubs during an informal breakout session in Orlando.

Technical Reports

Current Limits of X-ray Microdiffraction in Soft Condensed Matter Experiments

C. Riekel, M. Burghammer and S. Roth

European Synchrotron Radiation Facility, B.P. 220, F-38043 Grenoble Cedex, France

Received 14th December 2001; accepted in revised form 16th April 2002.

Introduction.

The ID13 beamline is providing microbeams for wide-angle (WAXS) and small-angle (SAXS) X-ray scattering experiments. An appreciable fraction of experiments is performed in the area of synthetic and biopolymeric materials. In the following review an overview on existing instrumentation, its limitations and the ongoing refurbishment program is given.

Generation of microbeams

The ID13 beamline is installed at a low- β section [1]. The current radiation source is a 46mm period undulator (U46), which provides a large spectral tuning range. An 18mm period in-vacuum undulator (U18) will be installed in 2002 [2, 3]. Its fundamental will provide at 12.9 keV about a 7-fold flux increase as compared to U46. The optical system comprises a liquid N₂ cooled Si-111 double monochromator and a condensing (ellipsoidal) mirror (Fig.1). The photon source point of $134_{\text{hor}} \times 23_{\text{vert}}$ μm fwhm (full-width at half maximum) is geometrically demagnified by a factor of 10 by the condensing mirror [4]. The observed focal spot of about $20_{\text{hor}} \times 40_{\text{vert}}$ μm fwhm is, however, considerably larger than the expected $13_{\text{hor}} \times 2_{\text{vert}}$ μm fwhm. This is mainly due to mirror slope errors of $4.2_{\text{meridional}} \times 12.6_{\text{tangential}}$ μrad [5]. Smaller beam sizes at the sample position are defined by add-on optics such as a capillary, collimator or waveguide.

Currently available tapered capillaries provide about a 2 μm fwb (full-width at base) spot with a divergence of 2.3 mrad at 13 keV. Capillaries are used for ultra-low background WAXS experiments but require a short (<0.5 mm) sample-to-capillary exit distance [6]. The divergence and shielding of the capillary exit limits low-angle applications in practice to $Q_{\min} \approx 0.4 \text{ nm}^{-1}$ ($Q = 4\pi \sin\Theta/\lambda$) [7].

Collimating optics based on Pt/Rh electron microscopy apertures permits a reduction of the minimum beam size to about 5 μm fwhm. For a divergence of 0.2 mrad in the vertical plane one can reach $Q_{\min} \approx 0.06 \text{ nm}^{-1}$ by using an electron microscopy guard aperture. The horizontal divergence at the sample position of about 2.1 mrad can be further reduced by slits in front of the collimating system. On-going instrumental developments aim at reducing the beam size to about 2 μm by apertures while maintaining the Q_{\min} limit.

X-ray waveguide optics is used without the ellipsoidal condensing mirror and provides a coherent slab-like beam with $\leq 100 \text{ nm}$ size in the vertical direction [8]. At 13 keV the TE₀-mode has a divergence of about 1 mrad. Horizontal beam compression to about 3 μm by a cylindrically bent multilayer mirror has been demonstrated [9]. It is expected that other hard x-ray optics, which provides a two-dimensional sub-mm spot (e.g. zone plates), will become available in the future.

The second experimental hutch, which is currently being refurbished with a Kirkpatrick-Baez (KB) mirror-system, will be used principally for scanning SAXS/WAXS applications (Fig.1) This KB-system is based on two cylindrically bent, 170 mm long mirrors [10]. Mirror slope errors of $\leq 0.9 \mu\text{rad}$ fwhm are now technologically feasible [11]. Spot sizes expected from ray-tracing calculations assuming a 0.9 μrad fwhm slope error are shown in Fig.1 [6]. These calculations do not, however, take beam instabilities due to the source and monochromator vibrations introduced by the liq. N₂ cooling system into account. A beam defining collimating system will therefore be used in order to obtain a stable beam at the sample position.

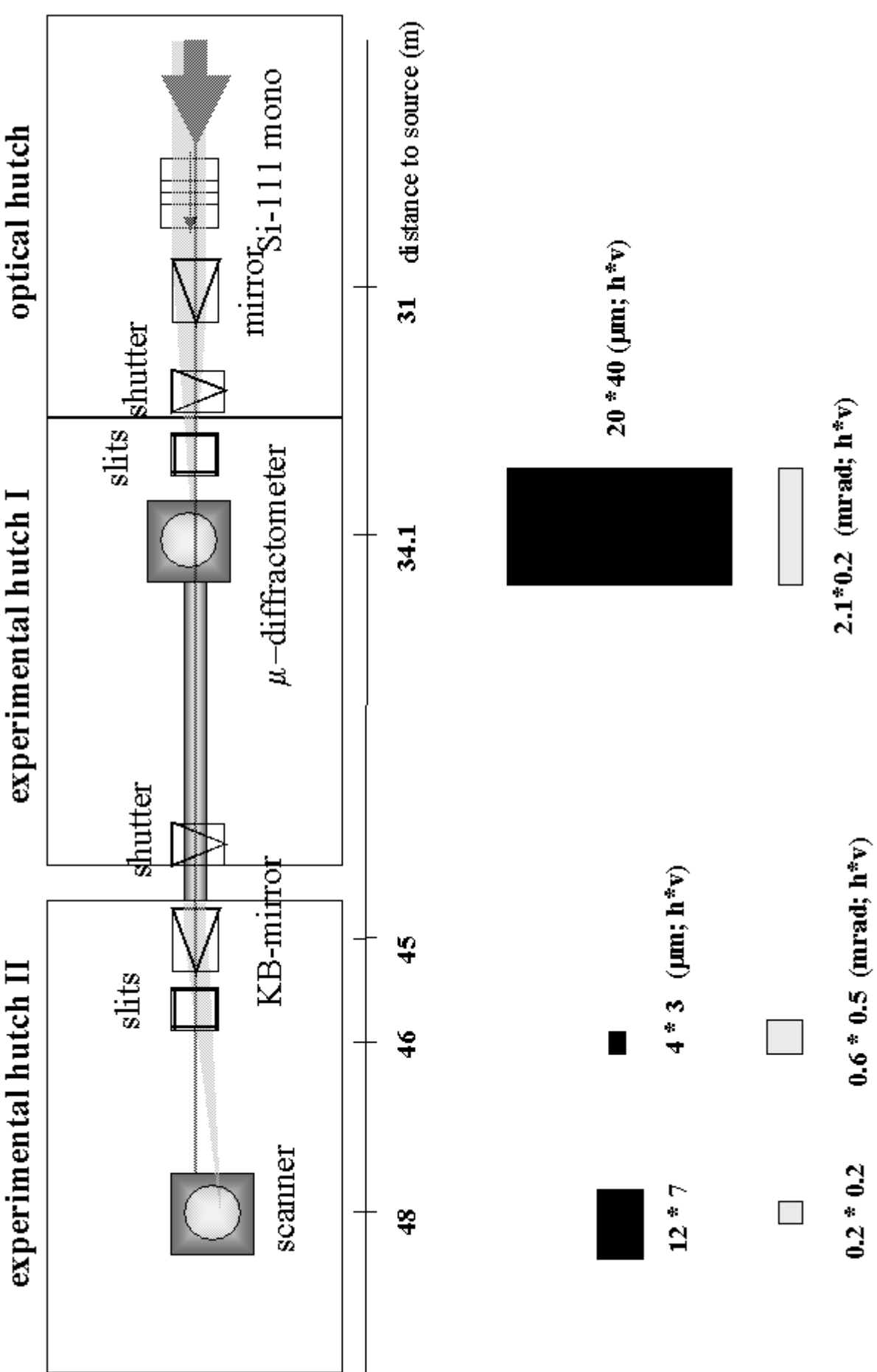


Figure 1: Schematic design of ESRF microfocus beamline (ID13). The size (experimental value) and divergence of the focal spot in the first experimental hutch as well as the calculated values in the second experimental hutch are indicated.

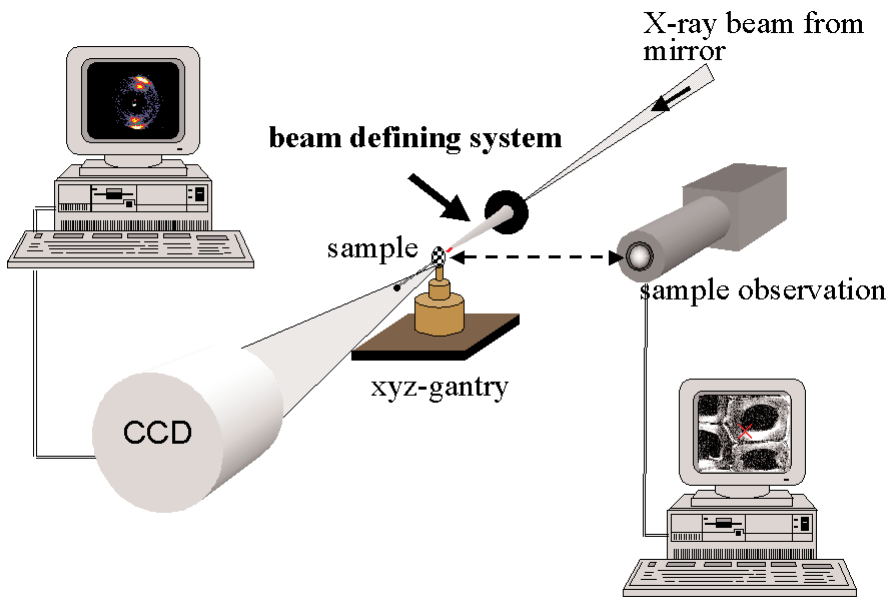


Figure 2: Schematic design of scanning setup [4]. The sample is pre-aligned with a video microscope and transferred into the beam via an x/y/z gantry.

Sample environment

The range of microdiffraction applications has led to the development of different setups for scanning diffractometry and single crystal diffractometry [4]. These setups are currently used in the first experimental hutch and will be installed in separate hutches after the refurbishment [4].

The scanning setup is shown schematically in Fig.2. The distance x-ray beam-to-optical microscope is calibrated by a polymer fibre cross to about ± 1 mm. The scanning setup is principally used for experiments on extended samples and complex sample environments with beam sizes down to about 2 μm . Sub-mm beams will require the development of a more precise positioning and sample observation system than currently available [9].

An interesting feature of the micro-collimating optics is that one can record SAXS and WAXS with the same detector provided its angular resolution at a given opening angle is sufficient [12]. This is the case for a 16-bit slow-scan MAR-CCD detector with a 130 mm diameter converter-screen and a point spread function of about 0.1 mm. At the level of a few mm beam size thermal drifts reduce the long-term stability of the collimating system which is currently composed of individually motorized apertures. This can be improved by controlling the temperature of the experimental hutch to $\pm 0.5^\circ\text{C}$ but is not very practical for routine user operation. A more stable block collimating system incorporating

the apertures is therefore currently being developed.

The SAXS/WAXS pattern of a collagen fibre recorded with a 5 μm beam at 13 keV demonstrates that the first order ($d=65$ nm) can be resolved from the beamstop (Fig.3). Fig.4 shows SAXS/WAXS patterns of single fibres from the minor (*MI*) and major (*MA*) ampullate glands of a *Nephila senegalensis* spider recorded with a 10 μm beam during an in-situ extrusion experiment [13]. The equatorial streak and the meridional 8nm peak in *MA*-silk suggest a fibrillar morphology composed of crystalline and amorphous domains [13, 14]. WAXS data show that the crystalline domains consist of poly(alanine) chains [15, 16]. The absence of a meridional 8 nm peak in *MI*-silk could be due to an increase in the size of the crystalline domains, which would shift the meridional peak to smaller Q-values. This is corroborated by *MI*-sequencing data showing larger alanine repeats as compared to *MA*-silk [17-19].

A limitation for scanning diffractometry is the exposure time of up to several seconds per frame (single pattern in a sequence) of slow-scan CCD cameras. This is not a problem for the collection of high-resolution fibre diffraction data which may take up to several minutes. If, however, data collection can be limited to a few statistically significant reflections (e.g. determination of Herman's orientation function [20]), then the framing rate should be matched to the frame exposure time. Framing rates of 5-10 Hz can be obtained with 12-

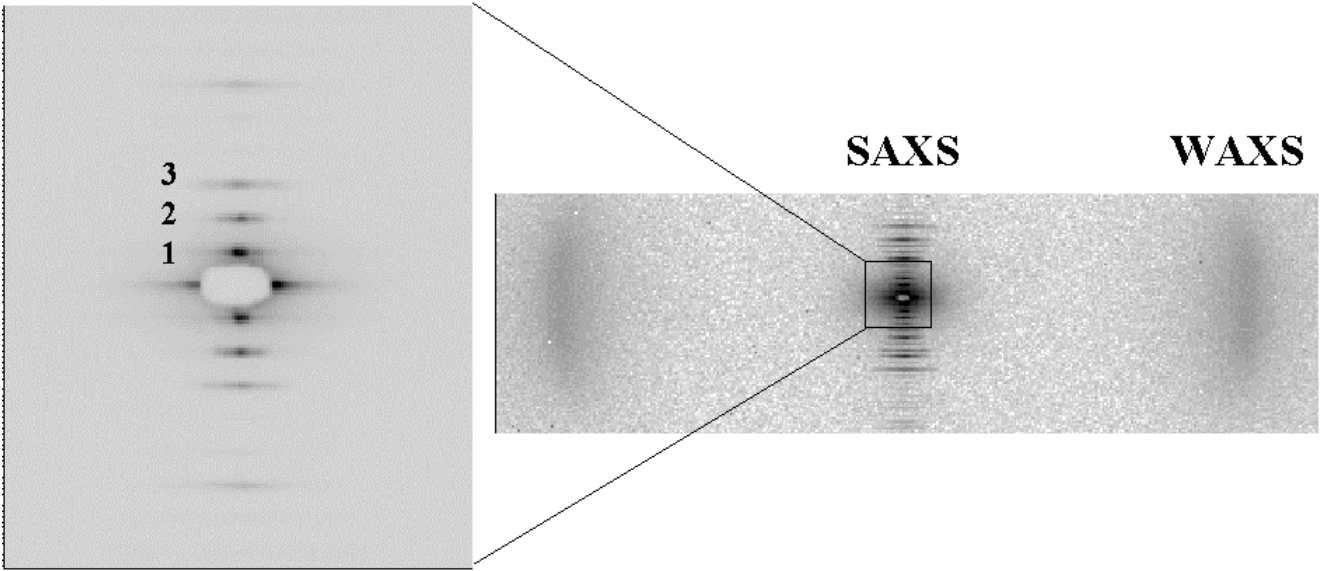


Figure 3: Combined SAXS/WAXS experiment for a dry rat's tail collagen fibre. The first order reflection (65 nm) is well separated from the beamstop.

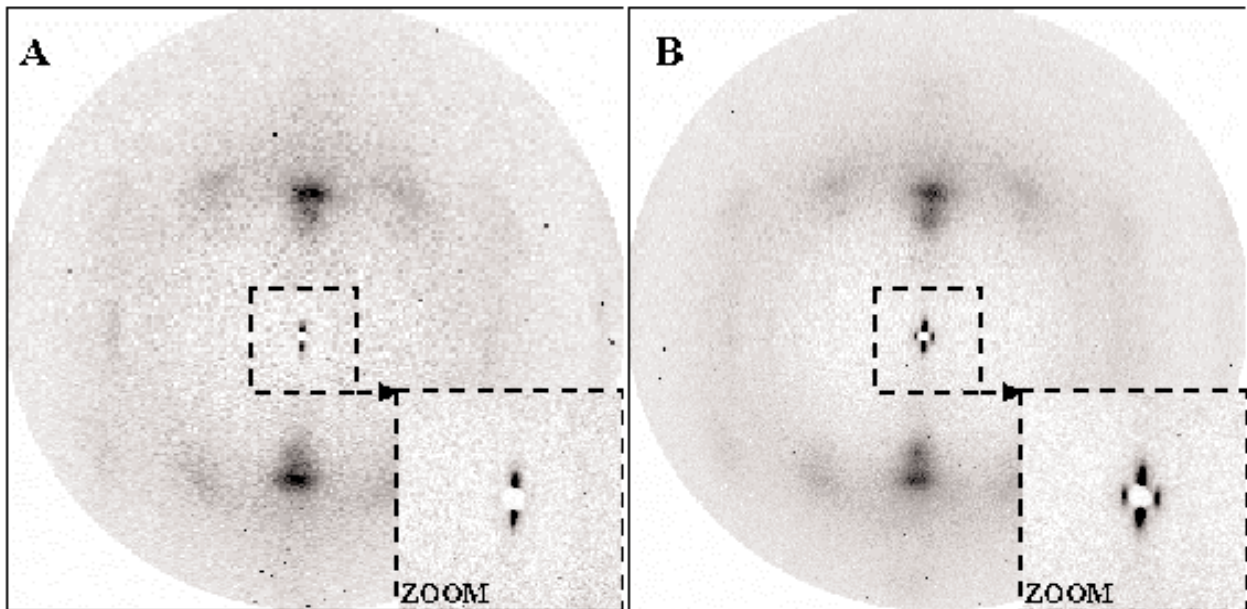


Figure 4: Combined SAXS/WAXS of minor and major ampullate *Nephila senegalensis* silk fibres during in-situ spinning [13]. The fibre axis is horizontally oriented. Note the difference in meridional scattering of the two fibres. The meridional major ampullate peak has a d spacing of about 8 nm. The edge of the beamstop defines $Q_{\text{min}} >> 0.6 \text{ nm}^{-1}$.

14-bit image-intensified CCD detectors. Selective area readout allows further increasing the framing rate. Fig.5 shows the variation of the relative integrated intensity and relative azimuthal width of the (200) reflection of a 12 μm diameter p(paraphenylene terephthalamide) fibre for three sub-second frame exposure times. Data were recorded with a 10Hz, 12 bit GemStar detector (Photonic Science). The data suggest that statistically significant profile parameters can be recorded for strong reflections at the 0.1 sec exposure level. The angular resolution at a given opening angle and

hence SAXS/WAXS capability of such systems is, however, currently more limited as compared to slow-scan systems. The quest for large-area detectors with high framing rate, high dynamic range, single photon counting capability and angular resolution is shared with biocrystallography. The pixel detector technology is an option for such applications [21]. Although fast framing detectors and the possibility for fast analysis of selected reflections [22] are becoming available, an integration in a dedicated scanning system will be required. This could for example allow determining Herman's orientation

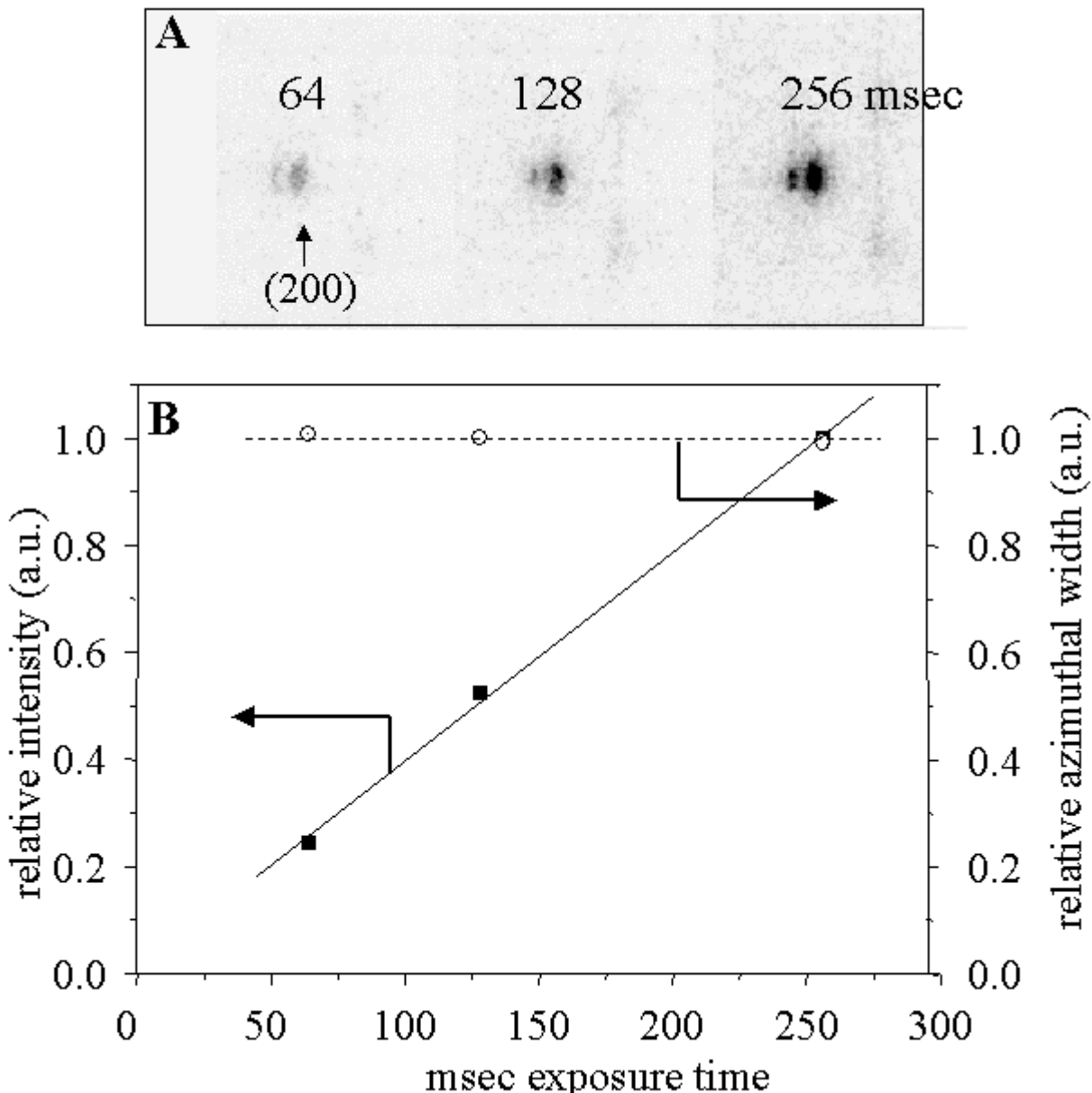


Figure 5: Single fibre diffraction for a 12 mm diameter PPTA-fibre recorded with a 12 bit image intensified CCD (Photonic Science). A: strongest equatorial reflections for three sub-second exposure times. B: relative integrated intensity and relative azimuthal width of (200) reflection.

function [20] for a fibre in "real time" during a stress/strain experiment.

Flux densities of ≈ 108 ph/s/ $\mu\text{m}^2/\text{mA}$ at the exit of a glass capillary allow recording WAXS patterns from an about 1 μm thick MI-silk fibre [23]. Averaging of several frames recorded along the fibre axis was, however, necessary. SAXS/WAXS patterns of such fibres at a one position should become accessible with a further increase of flux densities due to the use of an in-vacuum undulator (see above) and more efficient focusing optics. Primary radiation damage (PRD) due to breaking of chemical bonds is the ultimate limit for diffraction experiments while secondary radiation damage (SRD) due to the propagation of PRD-products can be reduced by cryo-cooling techniques [24, 25]. Single photon

counting capability (see above) is important in particular for in-situ experiments where SRD plays a role.

Single fibre diffraction experiments can also be performed using a micro-diffractometer which has been developed for protein crystallography [26]. A 5 μm beam and the possibility for on-axis observation of the sample is particularly useful for rapidly selecting specific points on a fibre or for examining a mixture of fibres. A He-filled tube can be used for low-angle applications down to $Q_{\min} \approx 0.21 \text{ nm}^{-1}$ (Fig.6). Improvements in the collimating system will be required in order to reduce this value. It is expected that ongoing instrumental development will allow the combination of scanning features with on-line observation capabilities. Techniques for sample

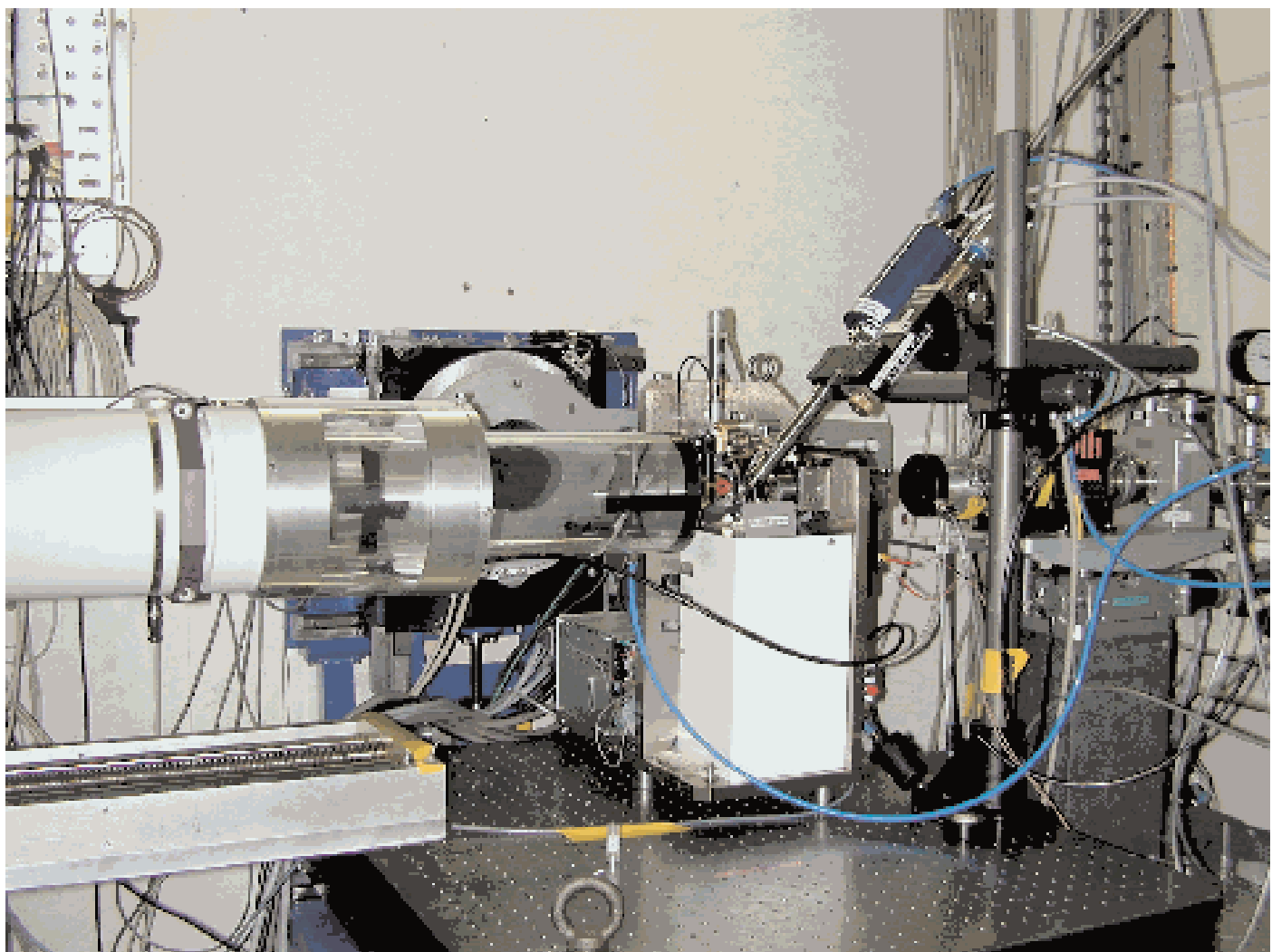


Figure 6: Microgoniometer with He-tube attached to CCD detector for low-angle applications.

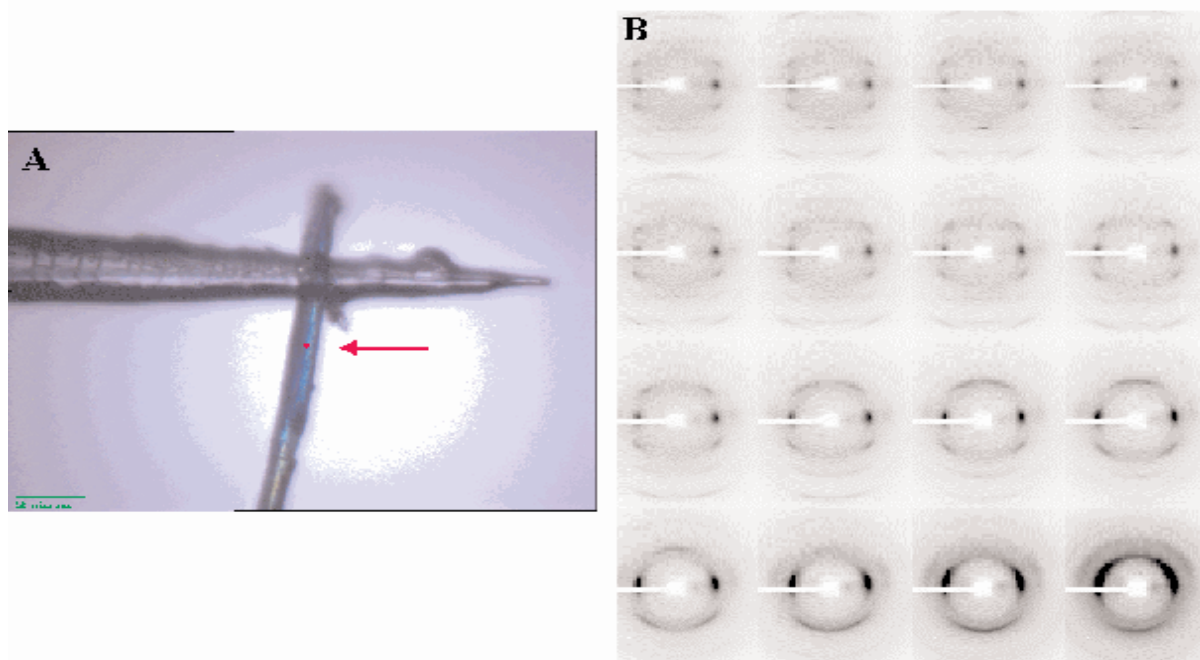


Figure 7: A: Optical image of *Bombyx mori* fibre glued to a glass capillary tip recorded on the microgoniometer. The red circle corresponds to a 5 mm diameter X-ray beam. B: WAXS frames recorded during the rotation of a *Bombyx mori* fibre around an axis normal to the fibre axis. Every rotational step was 50 with a recording time of 30 sec.

manipulation are similar to single microcrystal diffractometry. Thus an image of a short piece of *Bombyx mori* cocoon fibre glued to a glass tip prior to alignment is shown in Fig.7.a. Fig.7.b shows a sequence of frames recorded during the rotation of such a fibre around an axis normal to the fibre axis. Individual frames correspond to a 5° rotation within 30 sec. The beam is nearly orthogonal to the fibre axis in the first frame but nearly parallel in the last frame.

Conclusions

The current generation of microbeams available at ID13 allows WAXS experiments on fibres down to about 1 mm diameter in exceptional cases [23]. The use of cryo-cooling techniques, higher flux densities by in-vacuum undulators, better polished mirrors and single photon counting detectors should make SAXS/WAXS experiments at this level become routinely available. Critical issues like long-term beam stability, intensity monitoring or absolute intensity scaling have to be addressed but there is no reason why these technical problems could not be resolved. On-going X-ray optical developments allow extending beam sizes to the 100 nm range [9]. This will pose new challenges to sample environment setups including sample observation.

Acknowledgements

The development of the microbeam setup at ID13 is a team effort. We would like to mention in particular the contributions of P. Engström (Göteborg) and M. Müller (Kiel). The microgoniometer has been developed as a common project between EMBL-Grenoble and ESRF. We wish to thank in particular S. Cusack and F. Cipriani (EMBL) for their collaboration. The ESRF optics group (O. Hignette et al. has developed the KB-system.

References

- [1] http://www.esrf.fr/exp_facilities/ID13/index.html.
- [2] VanVaerenbergh, P., J. Chavanne, and P. Elleaume. Recent Developments of Insertion Devices at the ESRF. in *1999 Particle Accelerator Conference*. 1999. New York.
- [3] Chavanne, J., P. Elleaume, and P. VanVaerenbergh, In-Vacuum Undulators. *ESRF Newsletter*, 2000. **34**: p. 29-31.
- [4] Riekel, C., New Avenues in X-ray microbeam experiments. *Rep. Prog. Phys.*, 2000. **63**: p. 233-262.
- [5] Riekel, C., P. Bösecke, and M.S.d. Rio, Two High Brilliance Beamlines at the ESRF for Microfocus. *Rev. Sci. Instrum.*, 1992. **63**(1): p. 974-981.
- [6] Riekel, C. and L. Vincze, *Status and Perspectives of Capillary Optics at a 3rd Generation Synchrotron Radiation Source*. in press, 2002.
- [7] Engström, P. and C. Riekel, Low-Angle Synchrotron Radiation Diffraction with Glass Capillary Optics. *J. Synchr. Rad.*, 1996. **3**: p. 97-100.
- [8] Jark, W., et al., Submicrometer beamsize observed at the exit of an x-ray waveguide. *J. of Appl. Phys.*, 1996. **80**(9): p. 4831-4836.
- [9] Müller, M., et al., Microcrystallography with an X-ray waveguide. *J. Appl. Cryst.*, 2000. **33**: p. 1231-1240.
- [10] Hignette, O., et al. Submicron focusing of hard X-rays with reflecting surfaces at the ESRF. in *SPIE Conference Proceedings* 4499. 2001. San Diego.
- [11] Hignette, O., et al. Towards the preparation of optical surfaces preserving the coherence of hard X-rays. in X-ray mirrors, crystals and multilayers II. 2001: *SPIE Conference Proceedings*.
- [12] Riekel, C., M. Burghammer, and M. Müller, Microbeam Small-Angle Scattering Experiments and their Combination with Microdiffraction. *J. Appl. Cryst.*, 2000. **33**: p. 421-423.
- [13] Riekel, C. and F. Vollrath, Spider silk fibre extrusion: combined wide- and small-angle X-ray microdiffraction experiments. *Int. J. Biol. Macrom.*, 2001. **29**(3): p. 203-210.
- [14] Yang, Z., D.T. Grubb, and L.W. Jelinski, Small-Angle X-ray Scattering of Spider Dragline Silk.

Macromolecules, 1997. **30**: p. 8254 - 8261.

Science Published Ltd: London. p. 57-145.

- [15] Grubb, D.T. and L.W. Jelinski, Fiber Morphology of Spider Silk: The Effects of Tensile Deformation. *Macromolecules*, 1997. **30**(10): p. 2860-2867.
- [16] Bram, A., *et al.*, X-ray diffraction from single fibres of spider silk. *Journal of applied crystallography*, 1997. **30**(Pt3): p. 390-392.
- [17] Guerette, P., *et al.*, The spider silk fibroin gene family: gland specific expression controls silk properties. *Science*, 1996. **272**(5258): p. 112-115.
- [18] Colgin, M.A. and R. Lewis, Spider minor ampullate silk proteins contain new repetitive sequences and highly conserved non-silk-like "spacer regions". *Protein Sci.*, 1998. **7**: p. 667-672.
- [19] Gosline, J.M., *et al.*, The mechanical design of spider silks: from fibroin sequence to mechanical function. *J. of Exp. Biol.*, 1999. **202**: p. 3295-3303.
- [20] Stein, R.S. and G.L. Wilkes, *Physico-Chemical Approaches to the Measurement of Anisotropy, in Structure and Properties of Oriented Polymers*, I.I. Ward, Editor. 1975, Applied
- [21] Brönnimann, C., *et al.*, http://pc2462.psi.ch/pix_gen.html.
- [22] Riek, C., *et al.*, An X-ray Microdiffraction Study of Chain-Orientation in Poly(p-phenylene terephthalamide). *Macromolecules*, 1999. **32**: p. 7859-7865.
- [23] Riek, C., *et al.*, Microstructural homogeneity of support silk spun by Eriophora fuliginea (C.L. Koch) determined by scanning X-ray microdiffraction. *Naturwissenschaften*, 2001. **88**: p. 67-72.
- [24] Henderson, R., Cryo-protection of protein crystals against radiation damage in electron and X-ray diffraction. *Proc. Roy. Soc. B*, 1990. **241**: p. 6-8.
- [25] Teng, T. and K. Moffat, Primary radiation damage of protein crystals by intense synchrotron X-ray beam. *J. Synchrotron Rad.*, 2000. **7**: p. 313-317.
- [26] Perrakis, A., *et al.*, Protein microcrystals and the design of a diffractometer: current experience and plans at EMBL and ESRF/ID13. *Acta Cryst.*, 1999. **D55**: p. 1765-1770.

Mini-Reviews

Scattering Studies of Plant Cell Walls

A M Donald and O M Astley

Cavendish Laboratory, Madingley Road, Cambridge CB3 0HE, UK

Received 10th December 2001; accepted in revised form 14th March 2002.

Introduction

Cellulose - a polysaccharide - is the major component of plant cell walls, and is the commonest of all biopolymers. $\sim 10^{11}$ tonnes of cellulose are produced every year, and its uses are myriad. It is a linear polymer with a high level of internal hydrogen bonding (both interchain and intrachain). The interchain H bonding renders it insoluble in water and many common solvents, whereas the intrachain hydrogen bonding renders the molecule stiff; it is known to exist in extended microfibrils within the cell wall. This paper uses both small and wide angle x-ray scattering to examine the organisation of the cellulose within the cell wall and the response of the system to tensile deformation. In order to understand the cellulose itself, flax was chosen for study, because its secondary cell wall is thick and is fairly pure cellulose. However many plants contain substantial amounts of minority polysaccharides. To mimic such cell wall composites, the model system of acetobacter-produced cellulose fermented with appropriate minor polysaccharides has been chosen for study. Finally, to explore the supramolecular organisation within the cell wall, microfocus WAXS experiments on the algae *chara* - which has giant cells - were carried out.

A typical structure for a plant cell is shown in Figure 1. All cells have a primary wall, which is soft and flexible so that it can expand as the cell grows. After growth has stopped, many cells develop a secondary cell wall, which is much more rigid and provides structural support. In flax, this secondary cell wall is particularly thick, making up to 90% of the total cross section of the cell. It is about 70-75% cellulose, and the plant is therefore particularly suitable for studying the cellulose microfibrils. These microfibrils are always locally highly oriented. However, it is generally believed [1], that

through the thickness of the secondary cell wall the orientation rotates systematically, the alignment with each plane of microfibrils being rotated slightly with respect to its neighbours. This arrangement - equivalent to plywood but on a much smaller scale - is known as helicoidal (Figure 2).

The microfibrils are the smallest building block in the cell wall, but there is a whole hierarchy of structures present as shown in Figure 1. Any of these structures can be many microns across and up to mm in length: their cross sectional area increases in the order microfibril (also known in flax as an elementary fibre), technical fibre, bast fibre bundle, up to the whole stem.

Experimental

Materials

Flax (*linum usitatissimum*) came from both unkinked flax stems and extracted fibres from Cebeco, The Netherlands, and were kindly provided by ATO-DLO, Wageningen. The fibres had been extracted by warm water retting, or by soaking in ethanol for 24 hours at room temperature, and then the technical fibres removed by laboratory scale hackling. To position the fibres in the x-ray beam, approximately five to ten technical fibres were aligned, lightly stressed at each end with a small bulldog clip and glued onto a cardboard mount with Araldite. The unstretched fibre length was 20-30 mm.

Acetobacter-produced cellulose and its composites were kindly supplied by Dr Elisabeth Chanliaud, Unilever Research, Colworth, and were made as described in [2-4]. The strain *Acetobacter aceti* subspecies *xylinum* was used and was grown on a culture medium of glucose and salts. The composites grown were sheets or discs of several cm² area, up to 5mm thick, and containing up to 99%

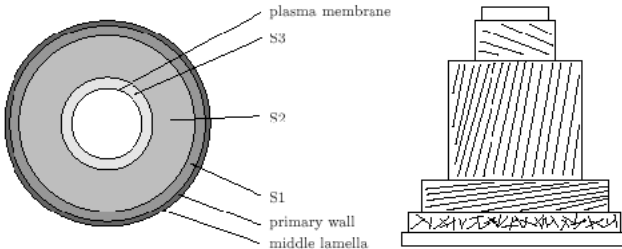
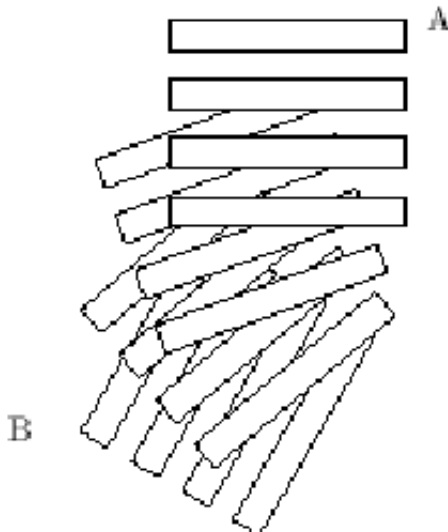


Figure 1: The traditional model of the plant cell wall of e.g. wood cells, showing the different layers: S1, S2 and S3. The cellulose microfibrils are unaligned in the primary wall, and strongly aligned with different orientations in the S1, S2 and S3 wall layers.



water by weight. Composites were stored in 0.02% sodium azide solution in a refrigerator to prevent degradation. The composites used were incubated with either tamarind seed xyloglucan or apple pectin (DE 30 or 37).

Chara corallina var *australis* was kindly supplied by Professor Enid MacRobbie and grown by John Banfield at the Department of Plant Sciences, University of Cambridge. The plants had been grown in artificial pond water made up of 1mM NaCl, 0.4mM KCl and 0.1 mM CaSO₄. Cells were harvested from almost full grown plants, and pieces of the cell wall removed from both the internodal cells and the leaf cells. To remove the cell wall, the end of the cell was cut and the contents washed out with artificial pond water. The edge of the cylindrical cell was cut with a razor blade in the direction of the cell axis, and the cell was laid out flat onto a washer. Finally the cell wall was held in position by attaching pieces of mica over the ends of the cell wall and fixing these with Araldite.

Methods

Experiments were carried out on flax and acetobacter materials at the Daresbury synchrotron source, using stations 2.1, 8.2 and 16.1. A camera length of 3m was used for the acetobacter studies, and of 9m for the flax work. Data were collected with two dimensional gas-filled detectors. Where it was desirable to maintain the state of hydration, the flax fibres were wet before exposure by spraying with deionised water and using an environmental chamber. Tensile experiments were carried out either using a Minimat straining rig, or a purpose built tensometer in which both grips moved, permitting the region under study to remain centred

Figure 2 Surface view of a helicoid between layer A and layer B. The rectangles represent cellulose microfibrils and A and B might represent different layers in the cell wall. The angle between the layers in this case has been chosen to be 20°.

under the beam. Straining rates of 1mm/min were used for the acetobacter composites, and rates between 0.01 and 0.5 mm/min for the flax.

The experiments on *chara* were carried out at the ESRF, Grenoble on beamline ID13. A beam size of 2μm was used, with a wavelength of $\lambda=0.787\text{\AA}$. The scattering patterns were collected on a two-dimensional CCD camera in time steps of 30s to minimise beam damage. Using the movable sample stage with an optical microscope on ID13 allows positioning of the sample. For these cell wall samples, diffraction patterns were recorded either across the wall in a direction perpendicular to the cell axis, or around interesting features in the optical microscope in a grid. Step sizes of 10 and 20μm were used, with grid sizes of up to 200 x 200 μm².

Results and Discussion

Figure 3 shows a typical SAXS pattern from a horizontal bundle of flax fibres. A strong vertical (equatorial) streak is seen, which is broader in the wet sample (Figure 3b) than in the dry (Figure 3a). This streak arises from the microfibril scattering, and quantitative analysis of it can provide detail on the shape and dimensions of the microfibrils. From such figures, the one-dimensional small angle scattering intensity can be found by summing the intensity over a horizontal (or vertical) slice. $\hat{I}(q)$ is therefore equivalent to a slit-smeared scattering pattern, although slit smearing does not occur for the

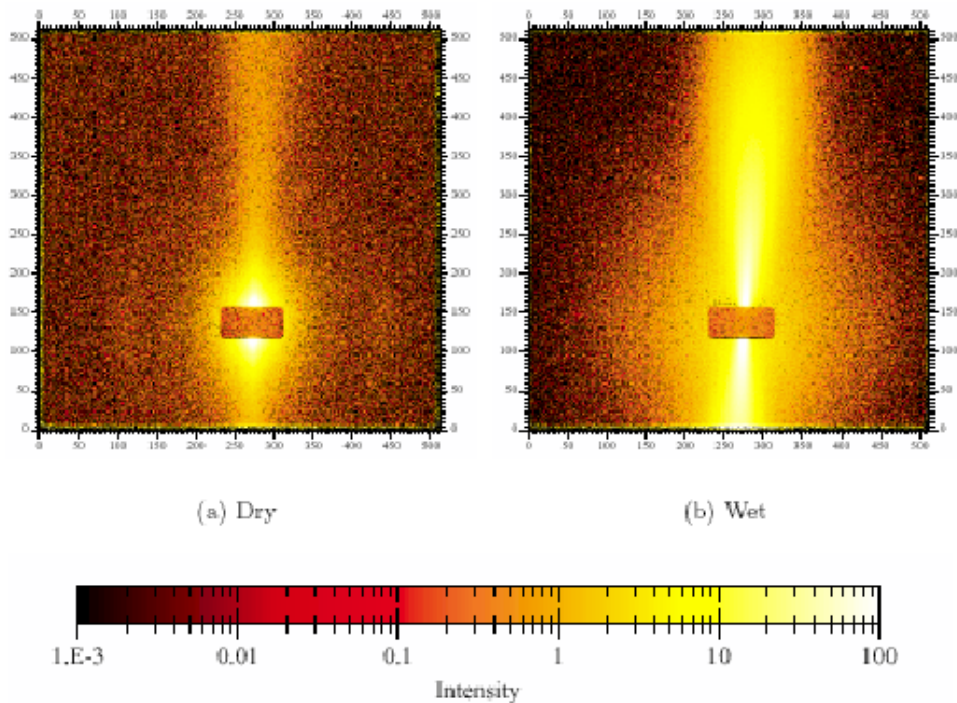


Figure 3 Typical SAXS patterns from flax fibres, recorded at $\lambda=1.4\text{\AA}$ with a camera length of approximately 3m, giving a q range of approximately $0.01\text{\AA}^{-1} < q < 0.20\text{\AA}^{-1}$. The fibre direction is horizontal. The two patterns are from the same sample, hydrated between exposures, of 2 min each.

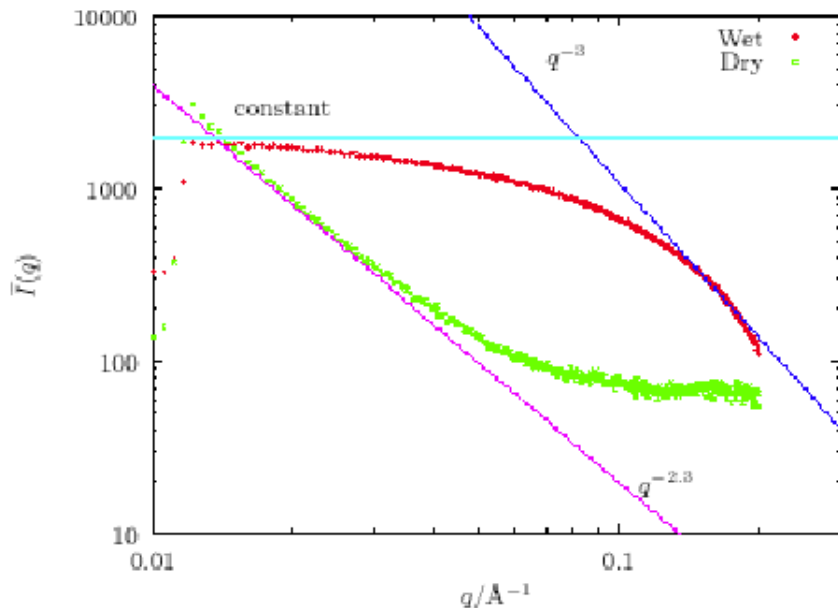


Figure 4 Plots of $\hat{I}(q)$ against q for very wet and very dry fibres, together with the $\hat{I}(q) = \text{constant}$ dependency predicted for long rods at low q , and the $\hat{I}(q) \propto q^{-3}$ dependency predicted by Porod's law at high q . The actual q dependency found at low q is also shown for the dry fibres.

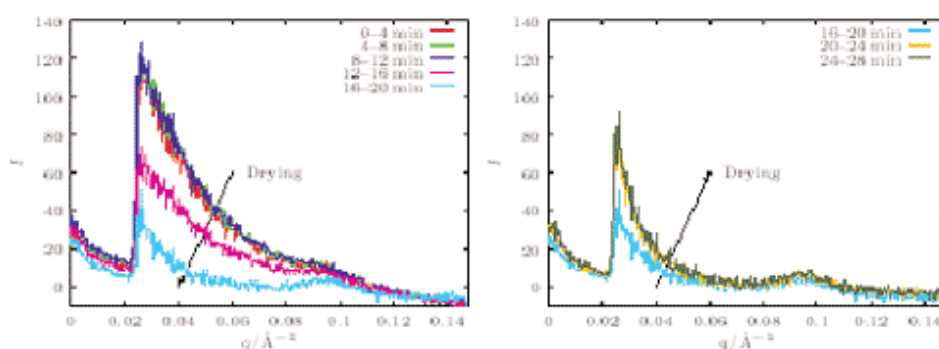


Figure 5 Meridional scattering patterns from drying flax fibres. The fibres were wet by spraying with deionised water and then letting them dry. The beam stop starts at $q = 0.24\text{\AA}^{-1}$, and the intensity below this value is due to a reduced direct beam.

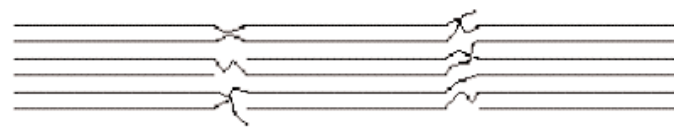
Method	Minimum r/Å	Maximum r/Å
Guinier	18.7 ± 0.4	26.9 ± 0.3
Porod, $\phi = 0.47$	12.4 ± 0.2	15.6 ± 0.2
Via S	12.1 ± 0.1	19.3 ± 0.2
Via I_c	24.7 ± 0.1	28.3 ± 0.1

Table 1.

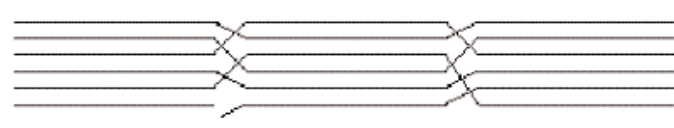
geometry of the Daresbury synchrotron (q is the scattering vector).

For a system of long rods, regardless of cross sectional shape, theory predicts that at low q , $\hat{I}(q) = \text{constant}$ [5]. At the other limit of large q , Porod's law states that $\hat{I}(q) \propto q^{-3}$. For the hydrated samples (Figure 4) shows that these expectations are borne out; however this is not the case for the dry fibres, where the shape of the $\hat{I}(q)$ vs q curve is very different. This is thought to be due to the microfibrils not scattering independently as assumed in arriving at these limiting laws (this has been shown to occur in other systems [6]): once the water is removed the microfibrils are no longer separated by water molecules. This leads to changes in the diffraction interference due to the concomitant changes in local scattering density.

If one starts off by making the further assumption that the rods are circular in cross section, with a radius of gyration r_c , and a cross sectional area S , then theory predicts the form of the scattering in the



(a)



(b)

Figure 6 The postulated periodicity along the flax fibre axis, consisting of a crystalline region 6nm long followed by ~1nm of non-crystalline material. In a) the long period would be expected to increase on stretching since the molecules in the non-crystalline regions are not taut, but in b) this would not be expected. The lack of change in the long period upon stretching suggests b) is correct for flax.

two limits of small and large q . The Guinier approximation leads to

$$\hat{I}(q) = \text{const} \exp(-q^2 r_c^2/2) \quad [1]$$

and the Porod approximation at high q yields

$$\hat{I}(q) = \lim_{q \rightarrow \infty} \frac{1}{q^3} \quad \frac{\hat{Q} C}{4S(1-\phi)} \quad [2]$$

where \hat{Q} is the invariant, C the circumference and ϕ the volume fraction of scattering elements. The invariant is defined by

$$\hat{Q} = \int_0^\infty q \hat{I}(q) dq \quad [3]$$

Alternative ways of calculating the dimensions of the fibrils also exist [7] using the invariant

$$S = \lim_{q \rightarrow \infty} \frac{2\pi \hat{I}(q)}{\hat{Q}} \quad [4]$$

and

$$l_c = \frac{2}{\hat{Q}} \int_0^\infty \hat{I}(q) dq \quad [5]$$

where l_c is the average chord length.

Table 1 shows the values of the radius obtained by these four different methods, with the spread of values obtained within a single method arising from data obtained on different samples. In order to use the Porod analysis to extract r , it is necessary to

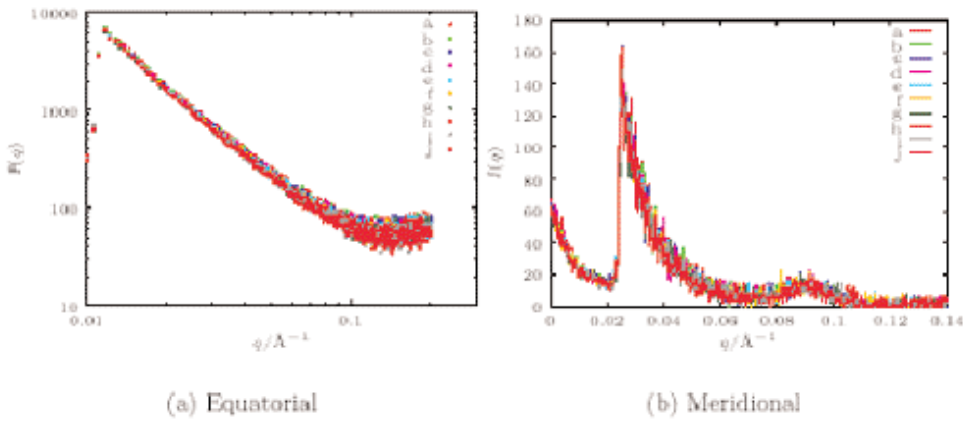


Figure 7 Plots of the equatorial and meridional intensities against q show no change in the scattering curves during stretching. Sample was dry flax stretched at 0.05mm/min. Curves $a-j$ correspond to data taken at intervals of extension of 0.1mm, with a corresponding to 0.05mm and j to 0.95mm extension.

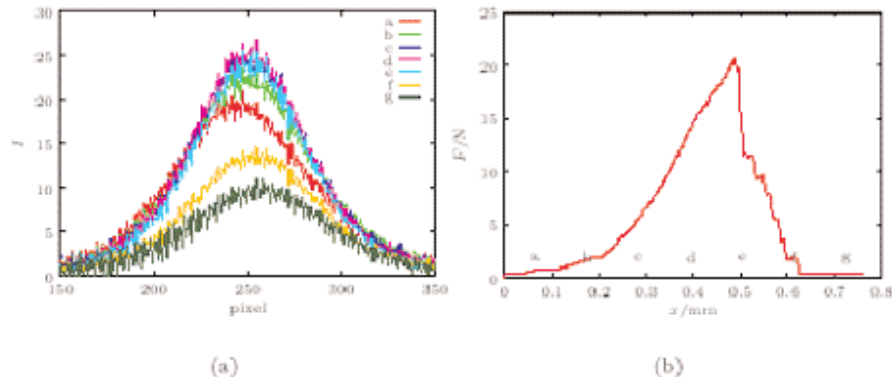


Figure 8 Changes in the (002) meridional peak of flax cellulose crystals as dry flax is stretched at 0.011mm/min. a) the orientation distribution, found by recording the variation in intensity along a line perpendicular to the meridian, at the position along the meridian of maximum breadth of the reflection across the wide angle detector; the letters indicate the position on the load-extension curve shown in b). As the WAXS detector in this set-up (simultaneous SAXS/WAXS) is off axis, the geometry is not precise.

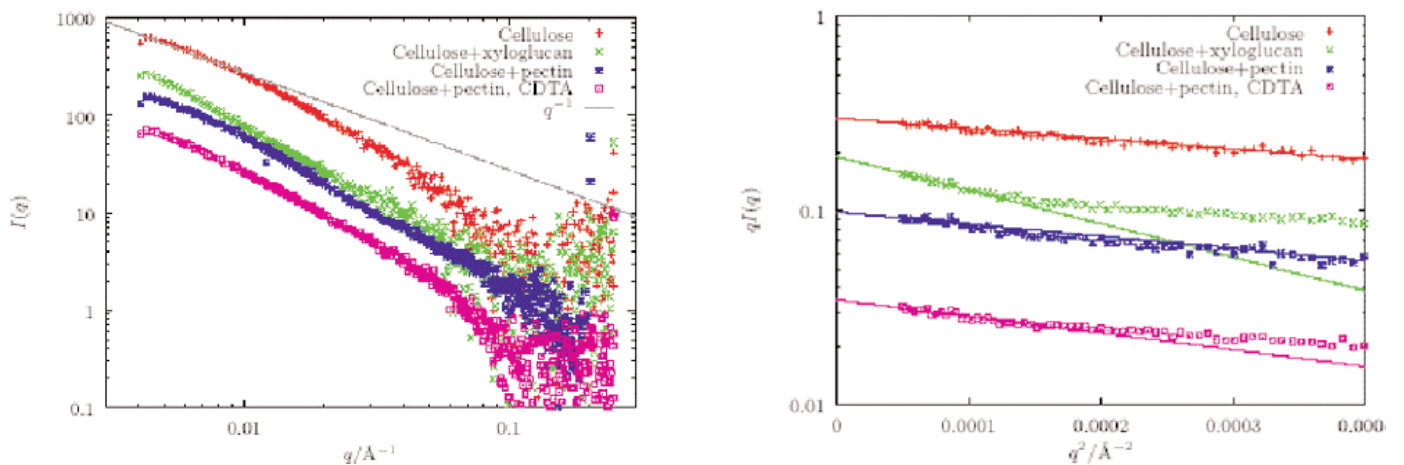


Figure 9:

- Scattering curves from *acetobacter* composites. The data were collected from both 3m and 9m camera lengths and normalised to allow for different beam intensities. Data have been offset for clarity. Also shown is the scattering function $I(q)\alpha q^{-1}$, which is predicted for long rods.
- Guinier plot of $qI(q)$ against q^2 for low q for different *acetobacter* composites. Points are experimental data lines are Guinier fits over the range $0.007 < q < 0.01 \text{ Å}^{-1}$, with a slope of $r_c^2/2$. The data have been offset for clarity.

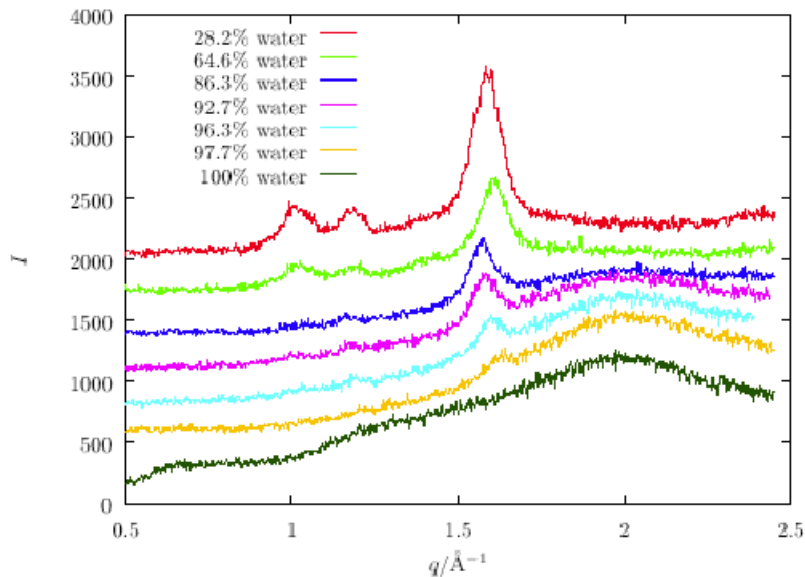


Figure 10 Powder X-ray diffractograms of *acetobacter* cellulose at different levels of hydration. Samples were dried by filter paper and by freeze drying; percentage of water is shown. Curves are offset for clarity. The pure water curve was obtained by holding between 2 sheets of mica.

assume both that the fibrils are cylindrical (i.e. have circular cross section) and a value for ϕ . This has been taken to be 0.47, an upper estimate based on the relative densities of the flax and crystalline cellulose [8]. As can be seen from the table, agreement between the different approaches is not good. This suggests that the original assumption of a circular cross section is not likely to be correct. A similar analysis can be carried out on the assumption the fibrils are rectangular. Based on this cross section values of $\sim 50 \times 10\text{\AA}$ are obtained, which is consistent with TEM evidence [9], but not with other SAXS data [10]. Thus the precise shape remains unclear. This section highlights the problem of trying to use SAXS to extract quantitative information on fibril shape and dimensions. Each method of analysis uses different approximations which affect the absolute numbers obtained. However TEM, although providing a more direct visualisation, introduces other problems such as potential artefacts during specimen preparation including the necessary dehydration and subsequent embedding in resin to permit cutting of ultrathin sections, and so is also not able to provide a reliable estimate of size.

So far we have only looked at the equatorial scattering. If we look at the meridional we find changes occurring during drying, as seen in Figure 5. In the scattering for the wet sample a faint shoulder is visible at $q \sim 0.1\text{\AA}^{-1}$, which becomes more pronounced upon drying. This position suggests a periodicity of 6-7 nm, presumably arising from alternating crystalline and amorphous regions along the chain direction. How this might arise is shown in

Figure 6. This model is discussed more fully in [11]. This meridional peak does not appear to have been observed in previous studies of cellulose I fibres, presumably because it is obscured by water scattering if the fibres are wet. Figure 5 demonstrates very clearly how the peak becomes more apparent as drying out occurs. It should be noted that hydrolysis studies of cellulose I have suggested much larger lengths for the crystallites in native cellulose. It therefore seems possible that two different crystal populations are coexisting in the fibre. The small crystals showing up here have a small dimension along the fibre, and a well-defined crystalline/non-crystalline repeat, unlike the larger crystals ($\sim 10\text{nm}$) previously reported [12]. Clearly the larger crystals dominate the scattering in general, and the 6nm crystals are only seen in rather dry fibres. Further discussion of this point is given in [11].

Let us now look at what happens when a tensile stress is applied to the flax fibre bundle. Figure 7 shows the results from the SAXS patterns. From this figure it is seen that no changes occur. Thus realignment of the microfibrils does not occur - they

Sample	$r_c/\text{\AA}$
Cellulose only	49 ± 9
Cellulose and xyloglucan	89 ± 4
Cellulose and pectin	54 ± 9
Cellulose and pectin, CDTA treated	63 ± 7

Table 2.

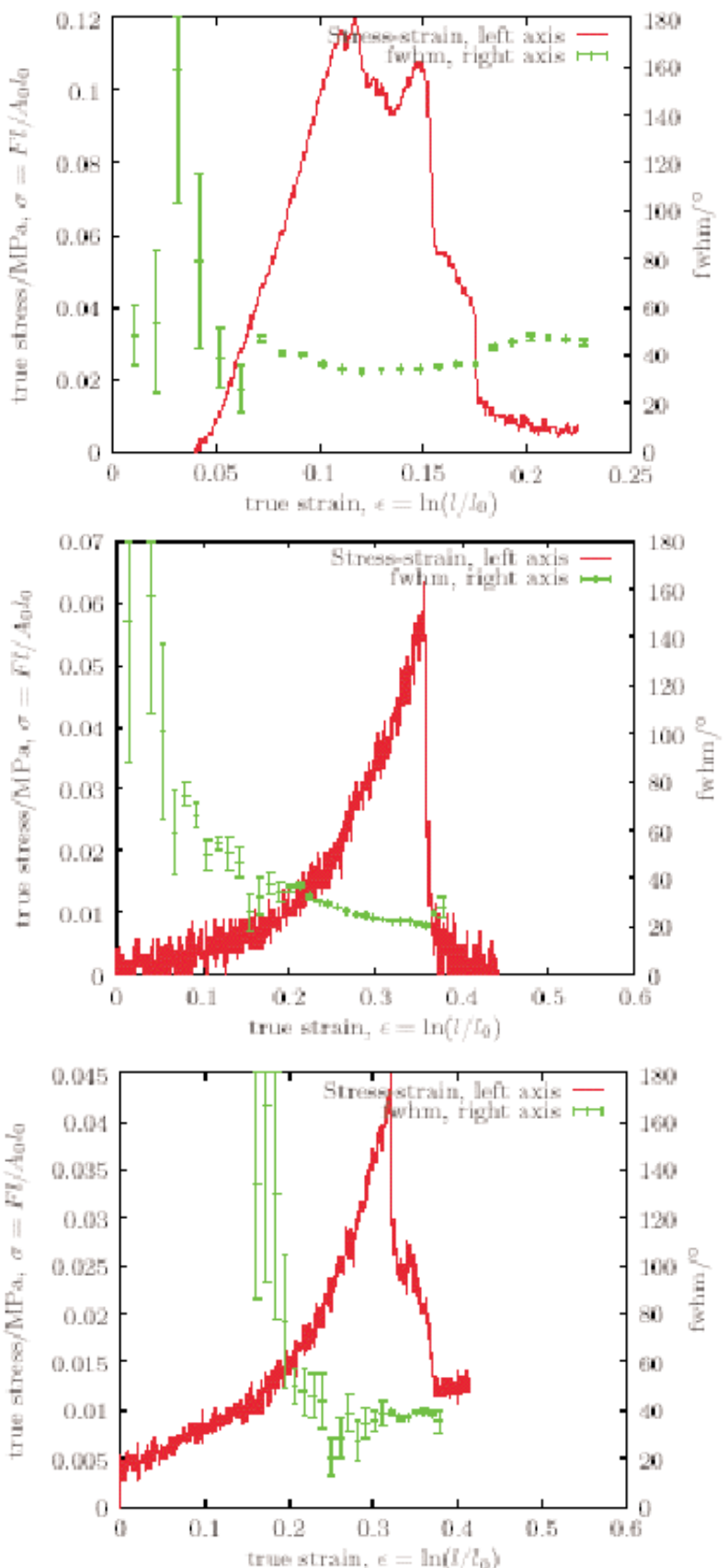


Figure 11 True stress-strain and misorientation (fwhm) curves for different *acetobacter* composites.

are already very well aligned - and the absence of changes in the meridional repeat means that this spacing is constant with stress. However changes are seen in the wide angle regime (Figure 8). Initially the intensity increases as the load increases up to the point where fracture occurs. Thereafter the intensity falls off, presumably due to some of the sample

having fallen out of the beam. Now since the SAXS signal has not changed, the overall repeat must be unchanged. Hence the increase in WAXS intensity seems likely to be related to strain induced crystallinity. Figure 8 shows how this can be achieved. The initial 6-7 nm repeat comprises a certain (unknown) percentage of amorphous

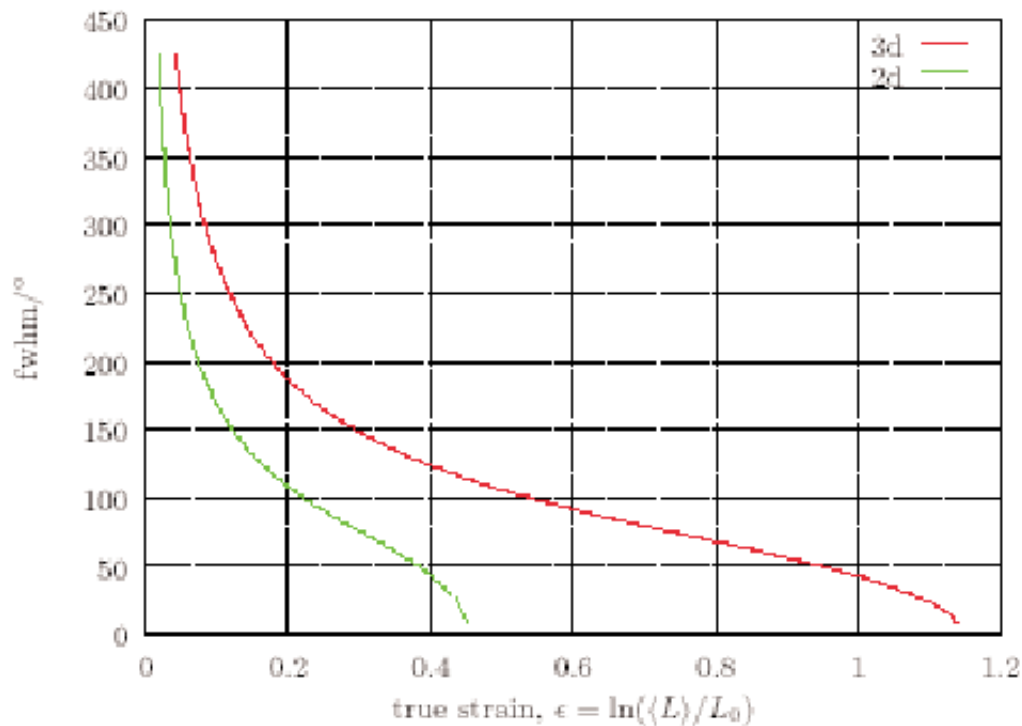


Figure 12 The expected strain produced by a Gaussian distribution of fibril orientations in two and three dimensions. Perfect orientation corresponds to $\langle L \rangle = 1$.

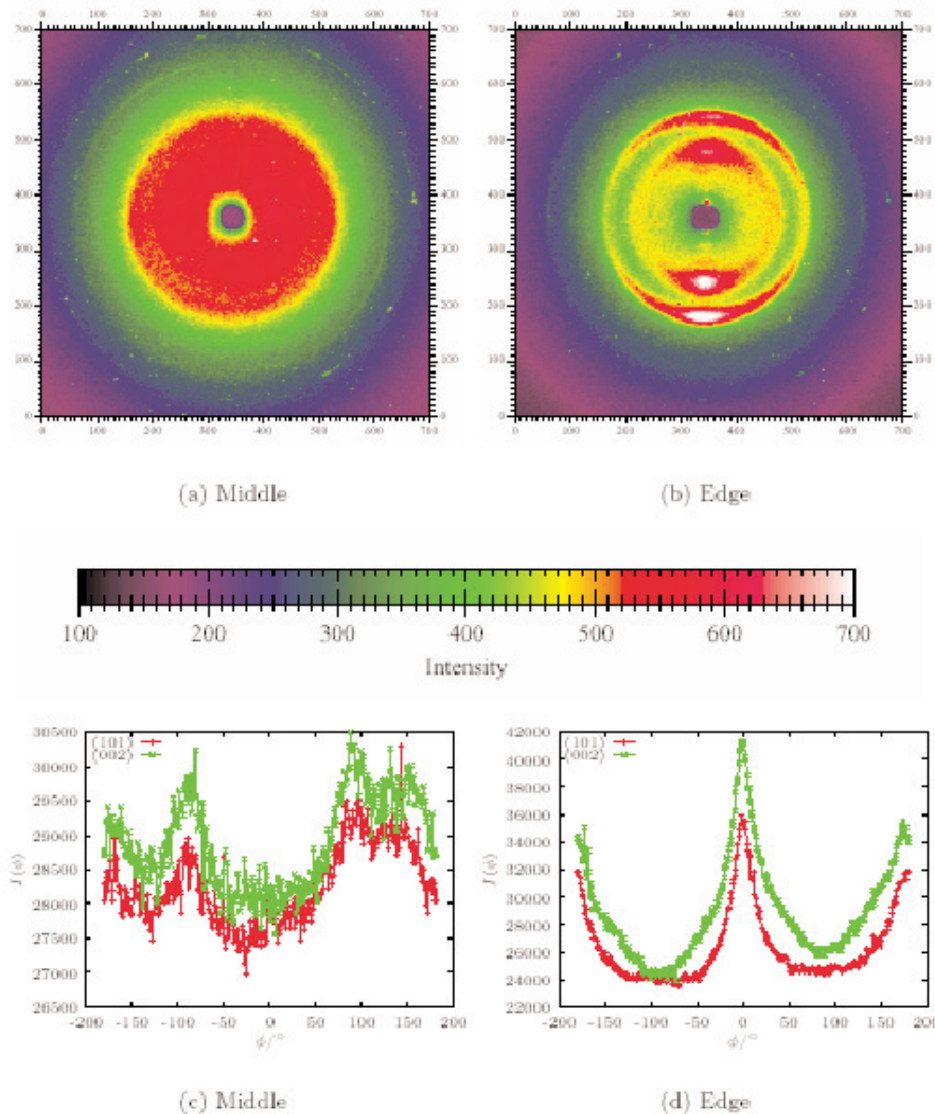


Figure 13 Scattering patterns taken from the middle and edge of a sample of a *chara* internodal cell wall. The two-dimensional images recorded on the detector are shown, together with the variation of the intensities for the (101) and (002) peak positions with angle. The meridional direction is horizontal.

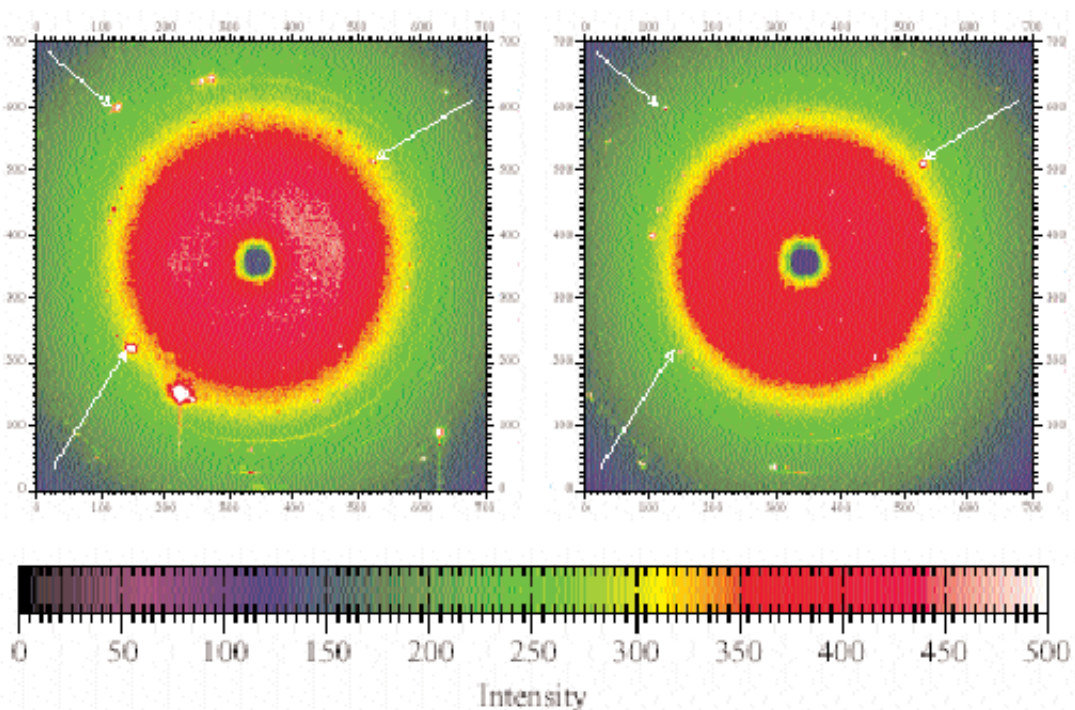


Figure 14 Diffraction patterns from the cell wall of a piece of *chara* leaf taken from adjacent 2 μm regions. Crystal peaks from the calcium carbonate in the same position in the two patterns are shown.

material. Under stress, some of this material can be pulled into better alignment and becomes incorporated into the crystals, thus increasing the overall level of crystallinity, without changing the overall repeat.

Acetobacter Results and Discussion

The bacterium *acetobacter xylinum* is known to produce cellulose in ribbon form usually in the cellulose I polymorph. By incubating the bacteria in a medium containing sugar and salt, pellicles of cellulose (incorporating water) can be produced. The inclusion of other polysaccharides in the incubation medium has been shown to lead to their incorporation in the pellicle [2].

SAXS of the different composites produced in this way are shown in Figures 9a. The Guinier approximation at low q was used to determine the radii of gyration for the microfibrils in each composite (Figure 9b) and the values obtained are shown in Table 2. It can be seen that the r_c determined is significantly larger for the xyloglucan composite than for the other systems. As in the work on flax, one presumes the fibrils are circular in cross section, which may not be a correct assumption. However, the differences between the different fibrillar building blocks for the different composites are small, and the difference in mechanical properties described below cannot be attributed to an

altered basic microstructure [13].

WAXS patterns on the as-produced pellicles showed no strong peaks, in contrast to previously obtained data (M Gidley, private communication). However these previous data had been obtained on freeze dried material. Figure 10 shows how the WAXS data (for pure cellulose) change as the water content is reduced, with the clear signature of cellulose I being visible below about 65 wt% water content (above this the peak is obscured). By using the Scherrer equation [14] on the (002) peak to estimate the size of the crystals

$$L_{002} = \frac{0.89\lambda}{\beta \cos \vartheta} \quad [6]$$

where λ is the wavelength of the radiation scattered through an angle 2θ , and β is the peak width in radians, it is found that the crystal size increases (non-linearly) with water content, with most of the increase occurring for water contents greater than 90%. The observed size for the (002) plane ranges from 5 nm when dry to 10 nm (assuming the crystals are perfect) when wet. This is in agreement with previous research on acetobacter cellulose [15]. Similar effects have also been seen on cotton [16], but in this case the crystal size increased at much lower water contents. It is suggested that the size increase arises from increased chain mobility in the

presence of water, permitting a higher percentage of the chains to move into the perfect register of the crystals. It cannot be due to recrystallisation, as this would occur in the more stable polymorph cellulose II.

The mechanical properties of the various composites are substantially different, as shown in Figure 11. The pure cellulose has a much higher breaking stress, and lower extensibility, than the composites. From the SAXS curves, it is possible to correlate the stress-strain curves with the reorientation revealed in the scattering patterns. Whereas for the fresh pellicle the scattering curves are isotropic, as loading proceeds the scattering starts to concentrate on the equator. The scattering intensity can be described by a Gaussian curve of the form

$$I(\phi) = A \exp\left(\frac{-(\phi - \langle \phi \rangle)^2}{2\sigma^2}\right) + \text{const} \quad (7)$$

where $\langle \phi \rangle$ is the mean fibril angle (normally essentially zero), σ is the standard deviation of the Gaussian and the constant is needed to take residual background scattering into account. Figure 11 shows the change in the full width half maximum of the $I(\phi)$ curves, equivalent to σ , for the different composites correlated with the stress strain curves. Despite the quantitatively very different stress-strain curves for the different samples, the shapes of the reorientation curves are very similar. Thus the rationale for the different mechanical properties cannot lie simply in the way the fibrils reorient.

However, if the system is modelled as a set of non-interacting rods it is possible to calculate the expected strain produced for different Gaussian distributions. To outline how this can be done, consider the simplest, if unrealistic, case of the fibrils (of length l) lying in a two-dimensional plane, with a distribution of fibril misorientations ϕ in the plane. The probability of the fibril lying at an angle between ϕ and $\phi + d\phi$ is given by

$$P(\phi)d\Phi = \frac{(I(\phi) - c)}{\int_{-\pi/2}^{\pi/2} (I(\phi) - c)d\phi} d\phi \quad (8)$$

where c represents a constant to allow for residual background scattering. In this two dimensional case, the average length of a fibril in a direction parallel to

the tensile axis is given by

$$\langle L^{2d} \rangle = \int_{-\pi/2}^{\pi/2} l P(\phi) \cos \phi d\phi \quad (9)$$

The true strain of such an assembly of fibrils can therefore be calculated, and related to the standard deviation of the fibril misorientation σ . This permits the dependence of σ , and hence the fwhm of a peak in the scattering pattern, to be directly related to the strain (further details can be found in [17]). A similar calculation can be carried out in three dimensions. The form of such curves (Figure 12) is qualitatively different from those experimentally determined. It therefore appears that the microfibrils are not independent. Hence one possible explanation for the differences observed mechanically between the composites is that there are changes in the frequency of entanglement or crosslinking.

It is known that xyloglucan can form chemical crosslinks with cellulose [16] and the specific behaviour of any composite will depend on the comparative strengths of the cross links and entanglements which can form, with better alignment of the cellulose microfibrils tending to prevent entanglement. Thus it would seem that the detailed response of these composites is driven by the precise way in which entanglements or other constraints form between the cellulose and added biopolymer, and not differences in reorientation of the underlying fibrillar morphology.

Results and Discussion for Algae

Cells from the green algae *chara corallina* var. *Australis* were sliced open so that microfocus experiments could be carried out at different positions within the cell wall. Figure 13 shows WAXS patterns taken at the middle and edge of such a cell wall from regions 2μm across. These patterns confirm that cellulose I is present, as previously reported for the similar algae *nitella* [18]. Clear differences are seen in orientation between the two patterns, but these cannot be related to the occurrence of helicoids. Indeed, no signature of helicoids was seen in these microfocus experiments. In general the predominant orientation is perpendicular to the long axis of the cell. The strong orientation seen at the edge of the sliced-open cell wall is attributed to orientation induced by the cutting process.

The absence of any sign of helicoids does not in this case mean they are not present. It would appear that because the main microfibril orientation dominates the scattering pattern they cannot be resolved. This assumption is supported by plotting the expected azimuthal scans from a helicoid with different degrees of orientation (assumed to be Gaussian) and different angles between the layers. Such curves show that the ability to resolve the Gaussian peaks depends on both of these variables, and hence on the experimental signal to noise ratio. It is also interesting to note that striations are visible on the surface of the cell. These striations are attributed to alternating acid and base regions [19]. The absence of any systematic changes in the microfocus patterns possibly indicates that these striations are not related to simple orientational changes. Alternatively, as evidenced by the lack of observed helicoidal structures, the fact that one is examining a projection through the cell wall may wash out subtle variations in packing.

However what is observed to vary between different regions of the sample is the presence of sharp diffraction spots arising from crystals, which are clearly not due to cellulose. Figure 14 shows patterns obtained from two neighbouring regions (~20 μm apart); some spots are seen to be common between these two patterns, but some spots also differ. Based on the total dataset obtained (50 different regions) it has proved possible to identify the crystals as calcium carbonate, and more specifically the calcite form. That calcium carbonate deposits exist on *chara* is well known - hence its common name of stonewort - but this study uniquely identifies the polymorph. Correlation of the crystal orientation with the underlying cellulose pattern also demonstrates that the presence of the calcite crystals does not affect the orientation of the microfibrils.

Conclusions

Using three rather different types of systems combined with both small and wide angle (including microfocus) scattering, it has been possible to probe different properties of the plant cell wall. The dimensions of the basic fibrillar building block can be established by fitting the SAXS curves. However, there is still some ambiguity about the precise dimensions, since the fit is model-dependent. It is also clear that there is some long-range periodicity, at the 6-7nm length scale, associated with regions of

good and poorer packing along the fibril direction. The meridional peak associated with this repeat in flax can only be seen in rather dry fibres.

Looking at cellulose composites provides an additional level of complexity, compared with the rather pure cellulose of flax. In this case it becomes clear that the differences in the fibrillar morphology between the different composites and in comparison with pure cellulose are small. Nevertheless the mechanical properties, as revealed by load extension curves collected simultaneously with SAXS/WAXS show substantial differences. These differences have been attributed to different degrees of connectivity between the fibrillar building blocks, associated with entanglements or crosslinking.

Finally, microfocus experiments have proved that the optical striations seen on the surface of the giant cells of the algae *chara* cannot be related to periodic variations in the underlying orientation of the cellulose fibrils. The only orientational differences observed appeared to be artefactual due to the cutting required during sample preparation. Using microfocus it has been possible to study the polymorphs of the small calcium carbonate crystals known to form on the surface of the plant. These have been shown to be of the calcite polymorph.

Acknowledgements

The authors are grateful to the BBSRC for funding. The assistance of all the beamline scientists is gratefully acknowledged (Anthony Gleeson, Günter Grossman, Sue Slawson, Nick Terrill, Martin Müller and Christian Riekel). The assistance of Drs Gidley, Chanliaud, John Banfield and Harriette Bos with sample supply is also acknowledged with thanks.

References

- [1] Neville, A.C., *Biology of Fibrous Composites: development beyond the cell membrane*. 1993, Cambridge: CUP.
- [2] Whitney, S.E.C., Brigham, J.E., Darke, A.H., Reid, J.S.G., and Gidley, M.J., *The Plant Journal*, (1995) **8** 491-504.
- [3] Whitney, S.E.C., Brigham, J.E., Darke, A.H., Reid, J.S.G., and Gidley, M.J., *Carbohydrate Research*, (1998) **307** 299-309.

- [4] Chanliaud, E. and Gidley, M., *The Plant Journal*, (1999) **20** 25 - 35.
- [5] Gawronski, M., Aguirre, G., Conrad, H., Springer, T., and Stahmann, K.-P., *Macromols*, (1996) **29** 1516-1520.
- [6] Heyn, A.N.J., *J Appl phys*, (1955) **26** 1113-20.
- [7] Glatter, O. and Kratky, O., *Small angle X-ray scattering*. 1982: Academic Press.
- [8] Astley, O.M., *Scattering studies of cell wall polymers*, . 2000, Cambridge University.
- [9] Näslund, P., Vyong, R., and Chanzy, H., *Textile Res J*, (1988) **58** 414-7.
- [10] Müller, M., Czihak, C., Vogl, G., Fratzl, P., Schober, H., and Riekel, C., *Macromols*, (1998) **31** 3953-57.
- [11] Astley, O.M. and Donald, A.M., *Biomacromols*, (2001) **2** 672-80.
- [12] Scallan, A.M., *Textile Res J* (1971) **41**, 647-53.
- [13] Astley, O.M., Chanliaud, E., Donald, A.M., and Gidley, M.J., *Int J Biol Macromol*, (2001) **29** 193-202.
- [14] Randall, J.T., *The diffraction of X-rays and electrons by amorphous solids, liquids and gases*. 1934, London: Chapman and Hall.
- [15] Fink, H.-P., Purz, H.J., Bohn, A., and Kunze, J., *Macromol Symp*, (1997) **120** 207-17.
- [16] Nakamura, K., Hatekeyama, T., and Hatekeyama, H., *Text Res J*, (1983) **53** 682-8.
- [17] Astley, O.M., PhD Thesis, University of Cambridge 2000.
- [18] Probine, M.C. and Preston, R.D., *J Exp Bot*, (1961) **12** 261-82.
- [19] Lucas, W.J. and Smith, F.A., *J Exp Bot*, (1973) **24** 1-14.

Characterising natural fibre composites with hierarchical structure

Peter Fratzl

Erich-Schmid-Institute of Materials Science, Austrian Academy of Sciences & University of Leoben, Jahnstr.12, 8700 Leoben, Austria

E-mail: fratzl@unileoben.ac.at

Received 2nd January 2002; accepted in revised form 16th April 2002.

Many biological tissues, such as wood and bone, are fibre composites with a hierarchical structure. Their exceptional mechanical properties are believed to be due to an optimisation of the structure at all levels of hierarchy. Wood, for instance, is essentially made of parallel hollow tubes, the wood cells. The cell walls are a composite of cellulose fibres in a matrix of lignin and hemicellulose. Bone, on the other hand, is a composite of collagen fibrils reinforced with calcium-phosphate mineral nano-particles. These mineralised fibrils are assembled into laminates which are the basis for a large variety of structures at higher hierarchical levels in bone.

X-ray fibre diffraction and/or small-angle scattering are ideal tools to characterise the fibre orientation (texture) and the size and arrangement of the components in the nanocomposite. Given the hierarchical nature of natural tissues, it is essential to use position-resolved diffraction methods. By such an approach, it is possible to scan a specimen and obtain information on several hierarchical levels simultaneously: the diffraction experiment yields information on the nanometer level, while the scanning procedure visualises the specimen with a resolution corresponding to the x-ray beam diameter, that is, in the micrometer range. The present paper reviews some recent experiments carried out with the goal to elucidate the relation between structure and mechanical function in wood, bone and dentin.

Introduction

Biological tissues such as wood, bone or tooth are hierarchically structured to provide maximum strength with a minimum of material. This is the reason why these materials are cellular solids (e.g., cancellous bone or wood) or gradient materials (e.g., dentin). At the lowest level of hierarchy (that is, in the nanometer range), they are fibre composites. A powerful approach to study such hierarchical materials is scanning x-ray diffraction [1] or scanning small-angle x-ray scattering [2]. The

principle is shown in Fig. 1.

A thin section of the material is scanned across a narrow x-ray beam. The diameter of the x-ray beam defines the lateral resolution of the scanning procedure. It is in the order of 100 micrometer on a laboratory x-ray source [1] and in the order of 1 micrometer (or even below) at synchrotron sources [2,3]. Ideally, the thickness of the specimen should be the same as the beam diameter, d . Then the scattering volume for each individual measurement will be about d^3 . Depending on the type of measurement - fibre diffraction or small-angle scattering - the evaluation of the scattering patterns yields information on the nanocomposite, within each d^3 -volume separately. Such local information from x-ray scattering can be advantageously combined with local information from other techniques, e.g. microspectroscopy or nanoindentation. The following examples are chosen to illustrate the capabilities of position-resolved x-ray diffraction methods for characterising hierarchically structured materials.

Mineral particles in calcified tissue, such as bone and dentin

The mechanical properties of calcified tissues cannot be understood without taking into account all structure levels [4]. Some anatomical features known to be important for the strength of the tissue are given on a dimensional scale in Fig. 2.

Even though the list is certainly not complete, it is obvious that the structures are spread over at least eight orders of magnitude. Clearly, no single technology can cover such a wide range. While all structures down to about a micrometer in size are accessible to light microscopy, higher resolution can be achieved by other probes, such as scanning- or transmission-electron microscopy, x-ray diffraction

**two
scales
in
one**

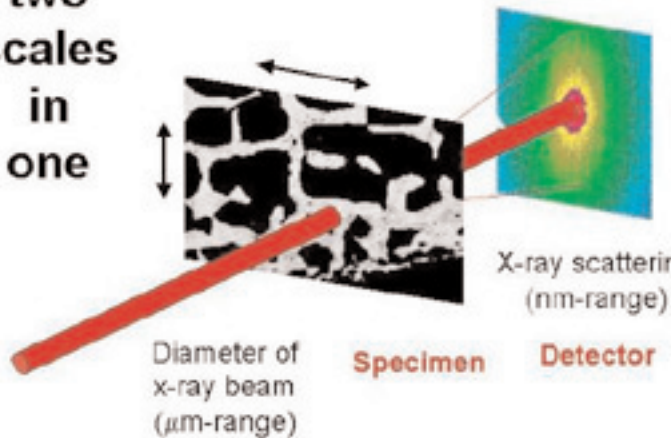


Figure 1: Sketch of a scanning diffraction experiment. Structural information in the nanometer range is obtained from the evaluation of the diffraction (or scattering) pattern. The micrometer range is covered by scanning the specimen across the narrow x-ray beam.

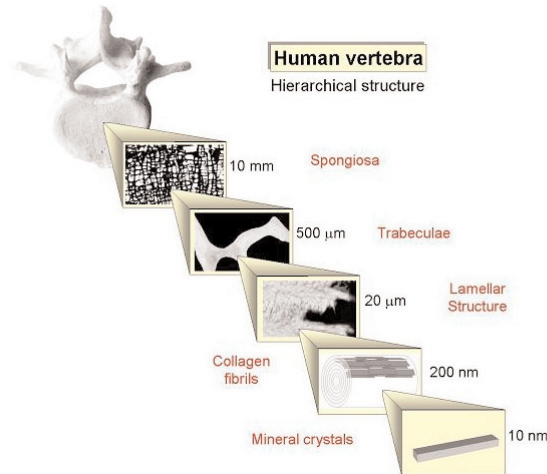
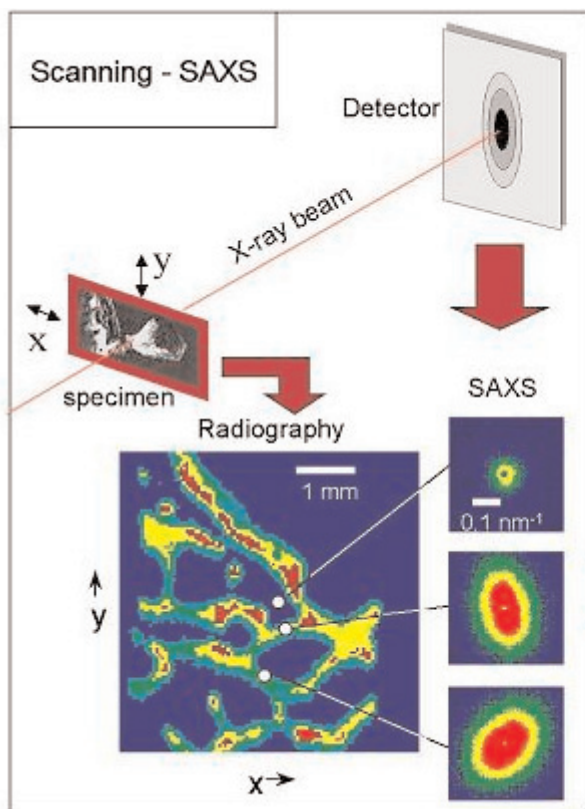


Figure 2: Hierarchical structure of the human vertebra, as an example of cancellous bone. The human vertebra is filled with a highly porous structure of spongy appearance. The trabeculae forming this cellular material are typically 200 micrometer wide and made of a composite of collagen and calcium phosphate mineral. This composite has a lamellar structure, where each lamella consists of a layer of parallel mineralised collagen fibrils. The orientation of the fibrils turns from lamella to lamella in way similar to a plywood structure. Individual collagen fibrils have a diameter of a few hundred nanometers, while the individual reinforcing mineral particles have a thickness of only a few nanometers.



Typical orientation of mineral crystals in human cancellous bone

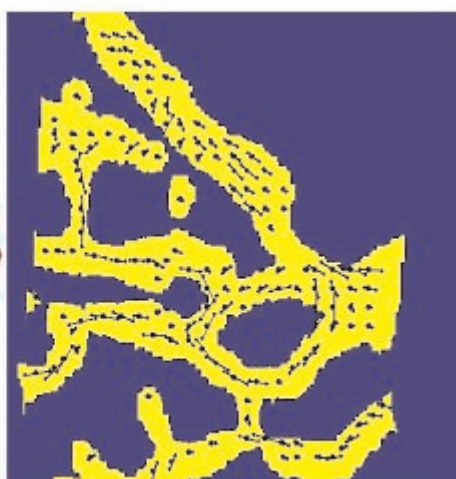


Figure 3: Scanning-SAXS investigation of human vertebra (from [5]). The specimen was a 200 micrometer thick bone section embedded in resin. First, the specimen was imaged by x-ray transmission (radiography). Transmission is high when the x-ray beam hits the (fully organic) resin and is low when it hits bone (which is a mixture of organic matrix and calcium phosphate). The trabeculae (see also Fig. 2) are clearly visible on this image. A number of positions were then chosen to perform SAXS-measurements. Clearly, SAXS-patterns are different at different positions. The evaluation of the SAXS-patterns gives the thickness and the orientation of the mineral particles in the organic matrix. As an example, the orientation is plotted by bars in the right side of the figure. Long bars mean high alignment, shorter bars less pronounced alignment of the particles within the volume of each individual measurement (in the present experiment, performed on a laboratory source, this volume was typically a cube with 200 micrometer side length).

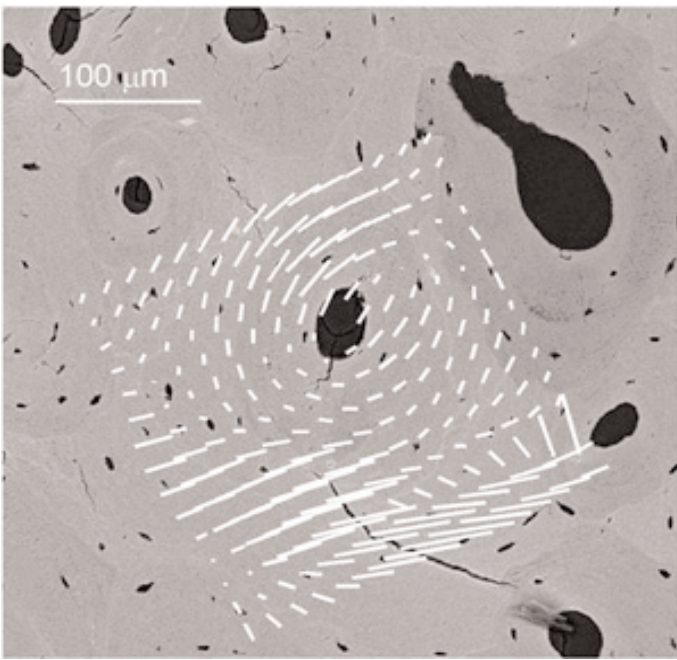


Figure 4: Orientation of mineral particle around an osteon in human compact bone (from [6]). The black ellipse in the centre is the trace of a blood vessel and there are concentric layers of bone lamellae around it, forming the osteon. Several osteons are visible on the backscattered electron image (BEI). The bars are results from scanning-SAXS, obtained at the synchrotron ELETTRA and superimposed on the BEI. They indicate the orientation of mineral platelets with the same convention as in Fig. 3. The specimen thickness and the diameter of the x-ray beam were 20 micrometers in this case.

(XRD) or small-angle x-ray scattering (SAXS) and, finally, by a variety of spectroscopic techniques, e.g., nuclear magnetic resonance or Fourier-transform infrared spectroscopy. One of the consequences of

the hierarchical architecture is that nanometer-sized structures may vary systematically throughout the tissue on a larger (typically micrometer-sized) scale. This introduces the technical difficulty that the nanometer-scale structures need, in principle, be characterized in a position-resolved way. A very powerful approach in this respect is scanning XRD or scanning-SAXS. A recent review can be found in [1]. The SAXS-contrast in bone or dentin is due to the huge electron density difference between the mineral particles and the organic matrix. SAXS is particularly useful since the typical thickness of the mineral particles is in the order of a few nanometers. Typical results of scanning-SAXS investigations of human bone are shown in Fig. 3 and Fig. 4. The first figure shows the typical data collection procedure.

First, the bone section is placed on an x-y stage movable perpendicularly to the x-ray beam. Ideally, the thickness of this section should be of the same order of magnitude as the diameter d of the x-ray beam, which defines the scanning resolution on the specimen. By this choice, a specimen volume of d^3 will be probed in each SAXS measurement. Using a laboratory x-ray source, d is limited by the counting statistics in the diffracted signal and cannot be chosen smaller than about 100 nm [2]. Using synchrotron radiation, d can be as small as 1 μm [1]. In the next step of the experiment, the bone section is scanned quickly across the x-ray beam to determine the transmission at each (x,y) position. A plot of

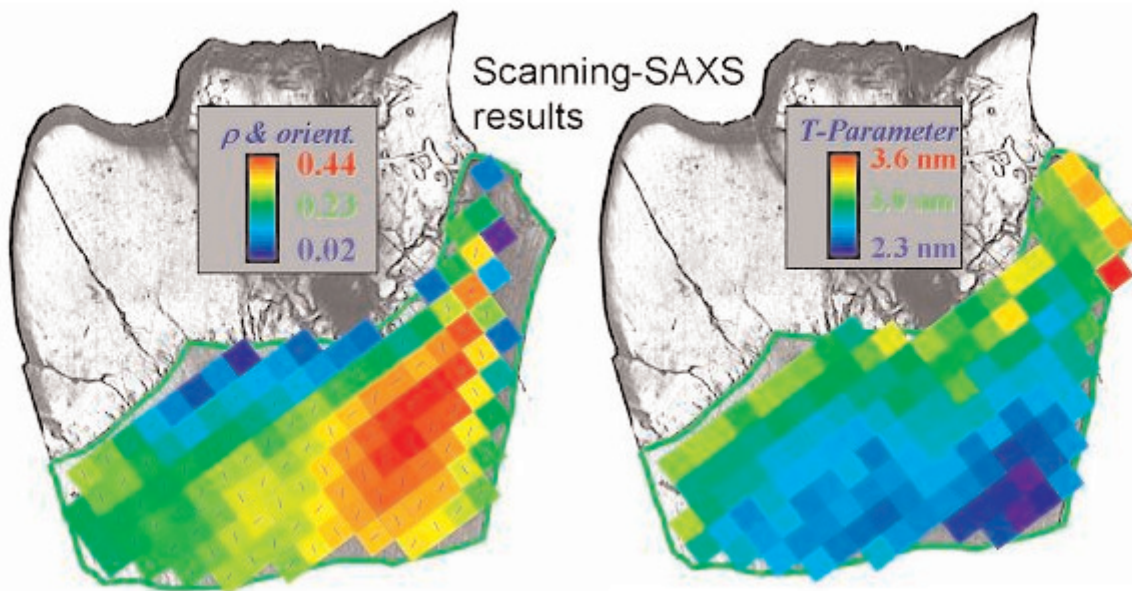


Figure 5: Thickness (right) and orientation (left) of mineral particles in human dentin (from [8]). The T-parameter, which is a measure for the particle thickness, varies from 2.3 to 3.6 nanometers. The degree of alignment r (a parameter which is =1, if all the mineral platelets are parallel, and =0, if they are randomly oriented) is larger further away from the enamel (top). The thickness of mineral particles correlates well with the elastic modulus measured (in position-resolved way) on the same specimen by nanoindentation [8].

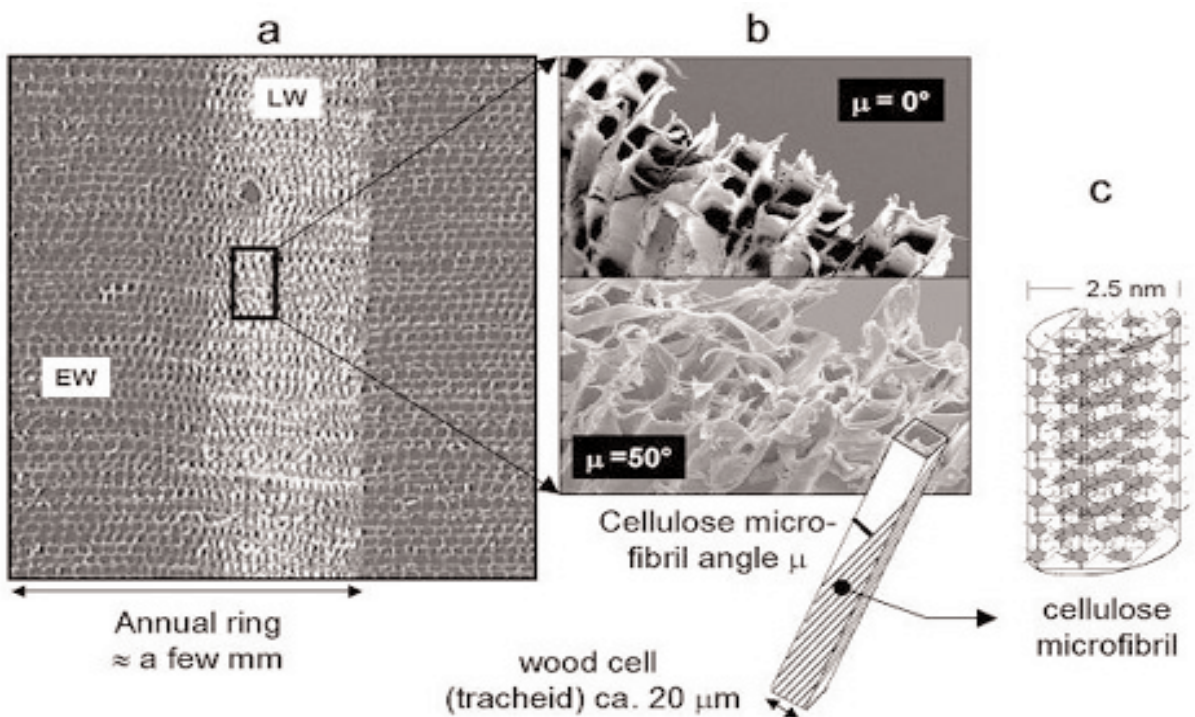


Figure 6: Hierarchical structure of spruce wood. (a) is a cross-section through the stem showing earlywood (EW) and latewood (LW) within an annual ring (from [9]). Latewood is denser than earlywood because the cell walls are thicker. The breadth of the annual rings varies widely depending on climatic conditions during each particular year. (b) shows scanning electron microscopic pictures of fracture surfaces of spruce wood with two different microfibril angles (from [10]). One of the wood cells (tracheids) is drawn schematically showing the definition of the microfibril angle between the spiralling cellulose fibrils and the tracheid axis. (c) is a sketch of the (crystalline part) of a cellulose microfibril in spruce (from [11]).

these data gives an image called "radiography" in Fig. 3. This image can serve two purposes: first, it is very useful to decide at which positions to collect SAXS data. The radiography in Fig. 3 shows a typical section through spongy bone, as one would find, e.g., in human vertebra or in clinical

biopsies from the iliac crest. Clearly, there are many positions where one would only find the embedding resin and, therefore, no signal from bone (blue regions). Useful positions for the SAXS measurements (red or yellow areas which reveal bone) can easily be identified on this image.

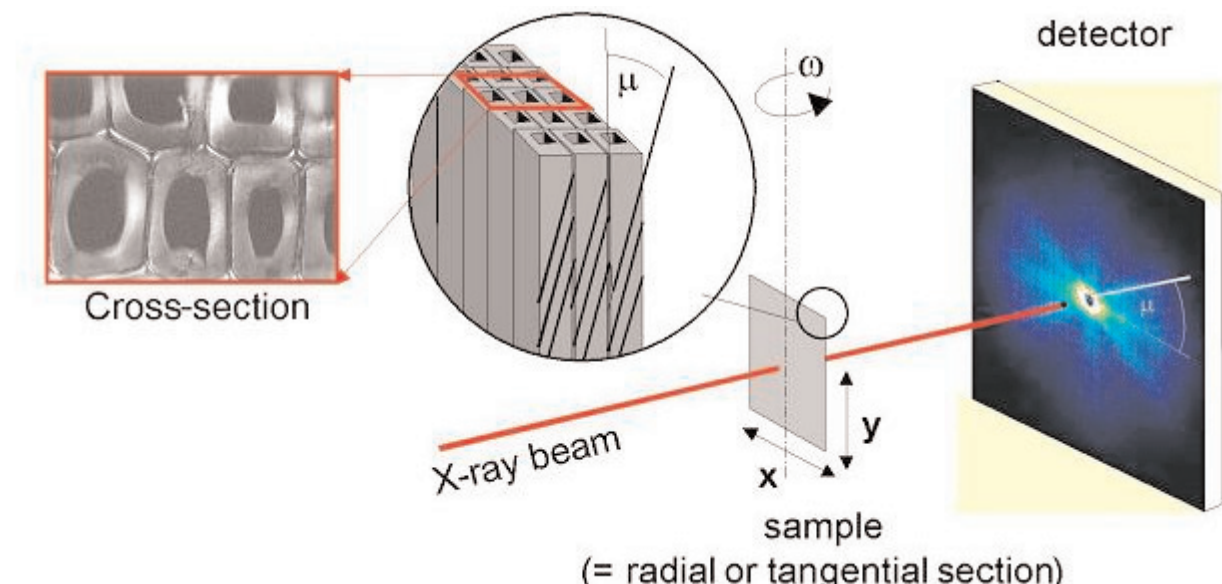


Figure 7: SAXS-signal from radial or tangential wood sections (the example shown is spruce wood), where the macroscopic fibre direction (the axis of the wood cells) is within the plane of the section (vertical in the example). The SAXS pattern shows several streaks originating from the cellulose fibrils tilted by an angle μ with respect to the macroscopic fibre direction. In normal spruce wood (see microscopic image on the left), the cross-section of the cells is rectangular. Hence, there are four different streaks on the detector, corresponding to cellulose fibrils in the four sides of the rectangular cells. If the distance specimen to detector is reduced sufficiently, it is also possible to measure the diffraction pattern from the crystalline parts of cellulose (see Fig. 8).

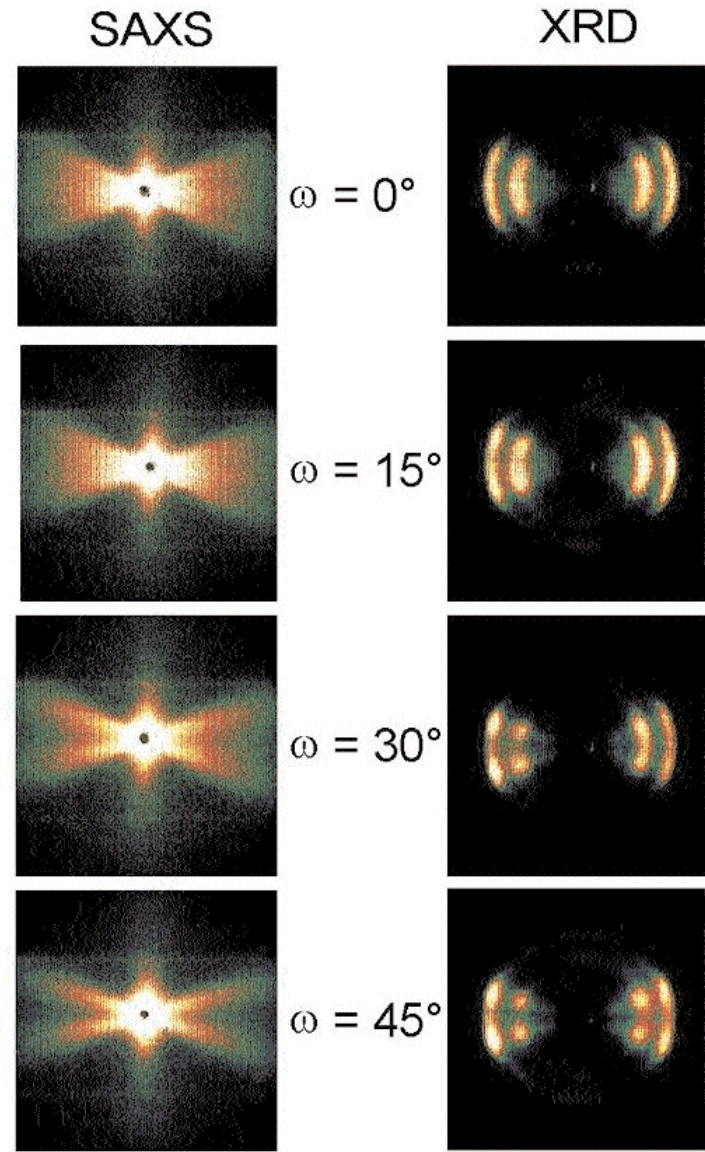


Figure 8: SAXS (left) and XRD (right) from cellulose fibrils in the wood cell wall of spruce wood, measured in the geometry shown in Fig. 7, for different rotation angles ω of the wood section. In all cases, the axis of the wood cells is oriented vertically. For $\omega=0^\circ$, the x-ray beam hits the rectangular tubes perpendicularly to one side, for $\omega=45^\circ$, the x-ray beam hits the (nearly square) tubes perpendicularly to an edge. Both, SAXS and XRD-signals can be used to extract the MFA (from [16]).

Secondly, radiographs can also be used to correlate the exact positions where SAXS data were collected to results from other measurements, such as light or scanning-electron microscopy [5]. The principle is to match the radiography to the corresponding light-microscopy image from the same specimen. The experience shows that the matching procedure works well, down to a precision of a few microns. Typical SAXS patterns obtained from bone are anisotropic (see Fig. 3) and it is possible to extract information on thickness and orientation of the (usually plate-shaped) mineral particles embedded in the organic matrix [5]. The rightmost image in Fig. 3 shows the typical orientation of the elongated mineral nanoparticles at many positions within the bone section. The direction of each bar gives the orientation of the longest axis of the particles within the plane of section. The length of the bar is a measure for the

degree of alignment which is reflected in the anisotropy of the SAXS pattern. It is obvious in Fig. 3 that the orientation of the mineral particles closely follows the orientation of the bone trabeculae in the spongy structure.

Fig. 4 shows similar kind of data, but collected within compact (and not spongy) bone, using an x-ray beam diameter of $20\mu\text{m}$ (that is, with a ten times better scanning resolution than in Fig. 3).

The orientation of the nano-particles reflects the layered structure of an "osteon" which is the tissue surrounding a blood vessel embedded in bone. The concentric arrangement of the layers is a mechanical protection of the blood vessel [1].

More recently, the structure of dentin (the bone-like

body of teeth) was studied by scanning-SAXS [7,8]. A gradient from the enamel towards the root was found both for the structure and for the mechanical properties [8]. Fig. 5 shows the orientation and the thickness of mineral particles in dentin as a function of position.

The figure shows that the T-parameter (which is a measure of the thickness of mineral particles) increases systematically from the enamel towards the root. The same section was also investigated by nano-indentation in an atomic force microscope, providing the elastic modulus of the tissue as a function of position. This mechanical parameter also exhibited a gradient from the enamel towards the tooth and was plotted against the particle thickness (as measured by the T-parameter) determined at the same position on the specimen. The excellent correlation between these two parameters is also shown in Fig. 5. This provides some insight on how the mechanical properties of mineralised tissue can be tuned by the type of reinforcing mineral particles. The probable reason for the grading of properties is a better long-term stability against failure of the tooth [8].

Cellulose microfibril angle in wood

The hierarchical structure of wood is shown in Fig. 6. At the lowest level, wood is a composite of cellulose microfibrils with a diameter in the order of a few nanometers and a matrix of lignin and hemicellulose. The cellulose fibrils are wound around tube-like wood cells with an angle called the microfibril angle (MFA, see Fig. 6). The MFA determines to a large extent the elastic modulus and the fracture strain of wood: When the MFA varies from 0 to 50°, the elastic modulus decreases by about an order of magnitude and the fracture strain increases by a similar factor [12].

Both XRD [11,13,14,16,17] and SAXS [9,11,15,16,18,19] have been used widely for the investigation of wood and, in particular, for the measurement of the MFA. Three geometries have been employed. First, radial or tangential wood sections were investigated as shown in Fig. 7.

In this case, the axis of the wood cells (that is, the

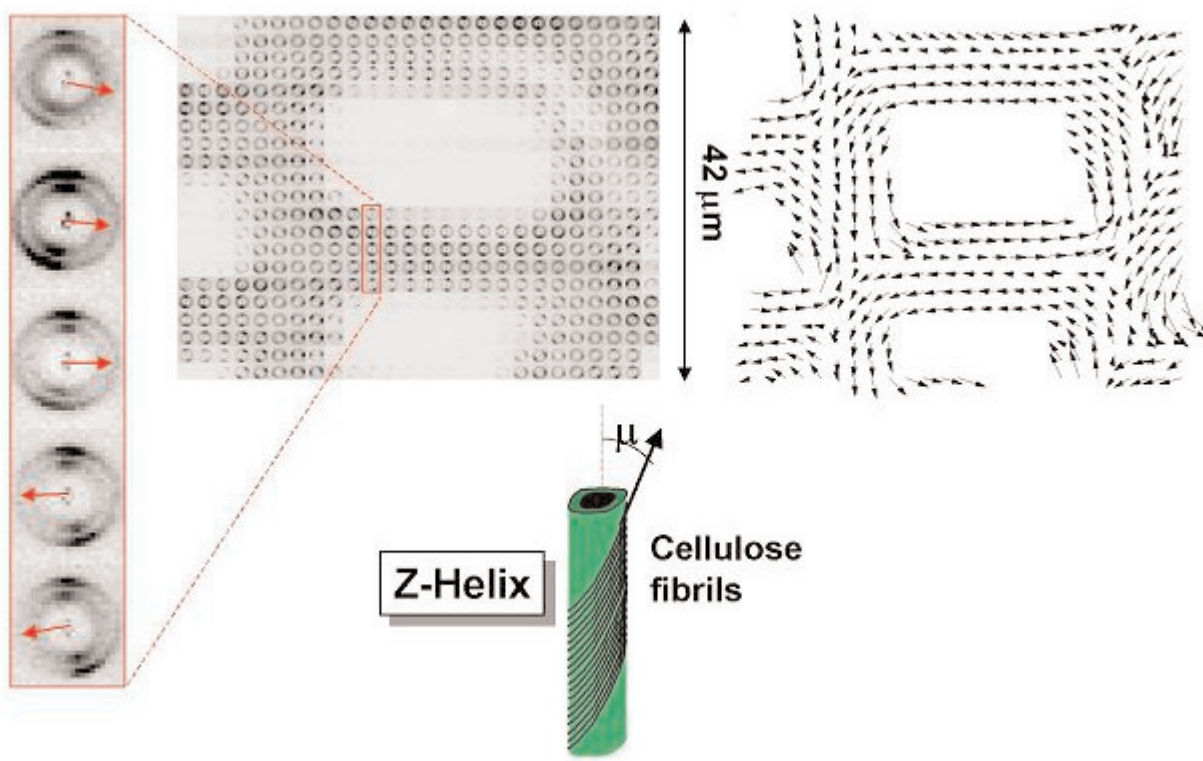


Figure 9: X-ray microdiffraction experiment with a 2 mm thick section of spruce wood embedded in resin (from [17]). Left: typical XRD-patterns from the crystalline part of the cellulose fibrils. Each pattern has been taken with a 2mm wide x-ray beam (at the European Synchrotron Radiation Source). The diffraction patterns are drawn side by side as they were measured. They reproduce several wood cells in cross-section. Note the asymmetry of the patterns in the enlargement (far left) which can be used to determine the local orientation of cellulose fibrils in the cell wall (arrows) [17]. The arrows are plotted in the right image with the convention that they represent the projection of a vector parallel to the fibrils onto the plane of the cross-section. The picture clearly shows that all cells are right-handed helices

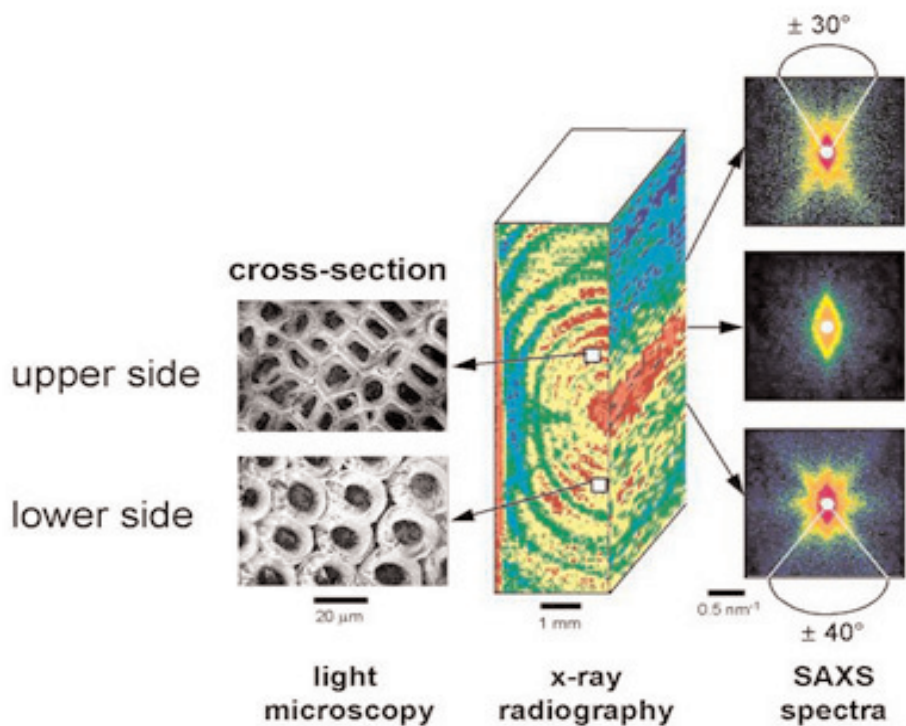


Figure 10: SAXS-patterns from a spruce branch (from [18]). Left: light-microscopic images of cross-sections. Note the round cell shape on the compression side (lower side) of the branch. Centre: X-ray transmission micrograph showing the annual rings. Right: SAXS-patterns showing an MFA of 30° on the upper side and an MFA of 40° on the lower side of the branch.

macroscopic fibre direction) is within the plane of the section. The direction of the cellulose fibrils is tilted by an angle m (the MFA) with respect to the cell axis. In SAXS, the contrast is due to the difference in electron density between cellulose and the surrounding matrix. In XRD, the contrast arises from the (partly) crystalline nature of cellulose, while the matrix is amorphous. For both types of measurement, a strongly anisotropic signal is expected from the cellulose fibrils, which may be used to determine μ . The difficulty is that the cellulose fibrils are actually spiralling around the wood cells, which means that several orientations of the fibrils superimpose in the scattering pattern. For cells with rectangular cross-section (as usually found in normal spruce wood, for instance) this means that the scattering pattern depends on the orientation angle ω of the cells with respect to the x-ray beam (the angle ω is defined in Fig. 7). This is demonstrated in Fig. 8, where both SAXS and XRD-signals are shown for different values of ω . The simplest case is when the x-ray beam hits wood cells with nearly square shaped cross-section perpendicularly to an edge of the tube ($\omega=45^\circ$ in Fig. 8). Then, only two streaks appear in the SAXS-pattern and the smallest angle between them is simply 2μ [16].

The third possibility which has been exploited to measure μ , is shown in Fig. 9. This technique is suited for investigating cross-sections (rather than radial or tangential sections). It has been used to determine the orientation distribution of cellulose fibrils within individual cells, with micrometer resolution [17]. The principle is based on the fact that - due to the curvature of the Ewald sphere - the diffraction pattern from cellulose fibrils becomes asymmetric in this geometry (see Fig. 9, left). Since the direction of the asymmetry depends on the local orientations of the fibrils by a simple formalism (given in detail in [17]), a map of fibril orientations can be drawn, demonstrating that the cellulose fibrils form right-handed helices around the spruce wood cells.

A final example is given in Fig. 10, where the MFA was determined in a branch of spruce. Clearly, not only the cell shape is different between the upper and the lower side of the branch (left side in Fig. 10), but also the MFA (right side in Fig. 10). It was shown recently that new wood, growing on the outside of an existing branch, has an MFA which tends to accommodate the mechanical properties to the increasing weight and length of the branch [20].

The author thanks all collaborators involved during

the last few years in the reported studies, in particular: J. Färber, H. Lichtenegger, O. Paris, W. Tesch, I. Zizak (Erich Schmid Institute, Leoben, A); M. Müller, Ch. Riekel (ESRF, Grenoble, F); H. Amenitsch, S. Bernstorff (ELETTRA, Trieste, I), A. Reiterer, S. Tschech (Univ. Agriculture, Wien, A); P. Roschger, K. Klaushofer (Ludwig-Boltzmann Institute of Osteology, Wien, A).

References

- [1] Paris O., Zizak I., Lichtenegger H., Roschger P., Klaushofer K., Fratzl P., Analysis of the hierarchical structure of biological tissues by scanning x-ray scattering using a micro-beam. *Cell. Mol. Biol.* (2000) **46**, 993-1004.
- [2] Fratzl, P., Jakob, H.F., Rinnerthaler, S., Roschger, P. and Klaushofer, K., Position resolved small-angle x-ray scattering of complex biological materials. *J. Appl. Cryst.* (1997) **30**, 765-769.
- [3] Riekel, C., Burghammer, M., Müller, M., Microbeam small-angle scattering experiments and their combination with microdiffraction. *J. Appl. Cryst.* (2000) **33**, 421-423.
- [4] Weiner, S. and H.D. Wagner, The material bone: structure-mechanical function relations. *Ann. Rev. Mater. Sci.* (1998) **28**, 271-298.
- [5] Rinnerthaler, S., Roschger, P., Jakob, H.F., Nader, A., Klaushofer, K. and Fratzl, P., Scanning small angle scattering analysis of human bone sections. *Calcif. Tissue Int.* (1999) **64**, 422-429.
- [6] Zizak, I., Paris, O., Roschger, P., Bernstorff, S., Amenitsch, H., Klaushofer, K. and Fratzl, P., Investigation of bone and cartilage by synchrotron scanning SAXS and -XRD with micrometer spatial resolution, *J. Appl. Cryst.* (2000) **33**, 820-823.
- [7] Kinney, J.H., Pople, J.A., Marshall, G.W., Marshall, S.J., Collagen orientation and crystallite size in human dentin: a small angle X-ray scattering study, *Calcif. Tissue Int.* (2001) **69**, 31-37.
- [8] Tesch, W., Eidelman, N., Roschger, P., Goldenberg, F., Klaushofer, K., Fratzl, P., Graded microstructure and mechanical properties of human dentin *Calcif. Tissue Int.* (2001) **69**, 147-157.
- [9] Lichtenegger, H., Reiterer, A., Stanzl-Tschegg, S.E., Fratzl, P., Variation of Cellulose Microfibril Angles in Softwoods and Hardwoods - A Possible Strategy of Mechanical Optimization, *J. Struct. Biol.* (1999) **128**, 257-269.
- [10] Reiterer, A., Lichtenegger, H., Fratzl, P., Stanzl-Tschegg, S.E., Deformation and Energy Absorption of Wood Cell Walls with different Nanostructure under Tensile Loading, *J. Mater. Sci.* (2001) **36**, 4681-4686.
- [11] Jakob, H.F., Fengel, D., Tschech, S.E. and Fratzl, P., The elementary cellulose fibril in picea abies. Comparison of transmission electron microscopy, small- and wide-angle x-ray scattering results. *Macromol.* (1995) **28**, 8782-8787.
- [12] Reiterer, A., Lichtenegger, H., Tschech, S. and Fratzl, P., Experimental evidence for a mechanical function of the cellulose spiral angle in wood cell walls. *Phil. Mag A* (1999) **79**, 2173-2184.
- [13] Cave, I. D., Theory of x-ray measurement of microfibril angle in wood, I and II. *Wood Sci. Technol.* (1997), **31**, 143-152 and 225-234.
- [14] Evans, R., Rapid measurement of the transverse dimensions of tracheids in radial wood sections from Pinus radiata. *Holzforschung* (1994) **48**, 168-172.
- [15] Kantola, M., Kähkönen, H., Small-angle x-ray investigation of the orientation of crystallites in finnish coniferous and deciduous wood fibers. *Ann. Acad. Sci. Fenn.* (1963) **137**, 3-14.
- [16] Lichtenegger, H., Reiterer, A., Tschech, S., Fratzl, P., Determination of spiral angles of elementary fibrils in the wood cell wall: comparison of small-angle x-ray scattering and wide-angle x-ray diffraction. In: *Microfibril Angle in Wood*, Butterfield, B.G. Editor (1998) IAWA-press, pp. 140-156.
- [17] Lichtenegger, H., Müller, M., Paris, O., Riekel,

Ch., Fratzl, P., Imaging of the helical arrangement of cellulose fibrils in wood by synchrotron X-ray microdiffraction. *J. Appl. Cryst.* (1999) **32**, 1127-1133.

- [18] Reiterer, A., Jakob, H.F., Stanzl-Tschegg, S.E. and Fratzl, P., Spiral angle of elementary cellulose fibrils in cell wall of picea abies determined by small-angle x-ray scattering. *Wood Sci. Technol.* (1998) **32**, 335-345.
- [19] Entwhistle K.M. and Terrill N.J. The measurement of the microfibril angle in soft wood. *J. Mater. Sci.* (2000) **45**, 1675-1684.
- [20] Färber, J., Lichtenegger, H.C., Reiterer, A., Stanzl-Tschegg, S., Fratzl, P., Cellulose microfibril angles in a spruce branch and mechanical implications. *J. Mater. Sci.* (2001) **36**, 5087-5092.

Recent insights into the three-dimensional molecular packing structure of native type I collagen

Joseph P.R.O. Orgel^{1,3}, Andrew Miller^{1,4}, Thomas C. Irving², and Tim J. Wess¹.

[1] Center for Extracellular Matrix Biology, Department of Biological Science, University of Stirling, Stirling, FK9 4LA, Scotland UK.

[2] Center for Synchrotron Radiation Research and Instrumentation and the Dept. Biological, Chemical, and Physical Sciences, Illinois Institute of Technology, 3101 S. Dearborn St. Chicago, IL, 60616. USA.

[3] Current: Laboratory for Molecular Biology (MC 567), University of Illinois at Chicago, 900 S. Ashland Ave. Chicago, IL, 60607. USA.

[4] Current: Interim Chief Executive office, Imperial Cancer Research Fund, 61 Lincoln's Inn Fields, London WC2A 3PX. UK.

Received 28th December 2001; accepted in revised form 15th March 2002.

The structure formed by the packing of collagen molecules within fibrous tissue has been a matter of some considerable speculation and debate for decades. Its importance is due to the fact that the arrangement of collagen molecules within fibrils must certainly impart the basis of the strength and integrity of mammalian connective tissue, and determines how collagen fibrils interact with other extracellular matrix components.

We recently reported a solution for the structure of collagen type I in situ [1]. This was obtained by modelling the x-ray fibre diagram and then solving the phase problem via MIR to produce our electron density map, thus avoiding any possible bias towards a particular structural model. In this paper, we review that work and present some additional details of the methods used that are particularly relevant to the fibre diffraction community.

The diverse range of proteins within the collagen family form the major constituent of connective tissues in most vertebrates [2]. Collagen is so prevalent that it is believed to be the single most abundant protein in the animal kingdom, accounting for approximately one third of the total protein mass in animals. Amongst these, collagen type I is the predominant form. Yet progress in understanding the organization of mammalian connective tissue at a basic level (the molecular arrangement) has been disproportionately slow when related to collagen's abundance, strategic functions and locations, and relative to the dizzying pace of structural solutions for soluble proteins through crystallography and NMR. A major factor impeding the progress of

collagen structure research has been the uncertainty inherent in the previous approach of comparing the calculated diffraction pattern of various stochastic models of the molecular packing with the observed diffraction pattern. Such an approach may permit discrimination among the chosen models but it cannot of itself provide assurance that a more accurate model, yet to be identified, does not exist. We have attempted to avoid possible bias by restricting the model generation process to that of the diffraction pattern alone, and then calculating phases from amplitudes obtained from native and isomorphously labelled samples. Obtaining the intensities from the diffraction pattern using this modelling approach and then obtaining the structure through MIR was made possible by a culmination of efforts, some of these efforts having lasted through the better part of one of our author's careers.

We present here a review of this challenging structural problem, and how we resolved it using a combination of fibre diffraction and x-ray crystallographic methods.

Collagen structure

The molecular organization of a single fibril is schematized in Figure 1. When heavily stained, collagen fibrils seen in electron micrographs exhibit the well-known dark/light-banding pattern, caused by the deposition of heavy metal into the gap resulting from a shorter fifth molecular segment within the five molecular segment unit cell. This axial structure is well defined. Meridional reflections in the fibre diagram extend beyond 0.45 nm (over

150 reflections). The lateral packing (molecular packing arrangement in cross-section of the fibril) was until very recently much less well characterized, except for the understanding that collagen molecules are somehow arranged on a quasi-hexagonal lattice [3,4]. It is the characterization of this part of the structure that has been so elusive.

The collagen x-ray fibre diagram, a technical challenge

A strong, diffuse 'fan' underlies the off-meridinal parts of the collagen fibre diagram (Figure 2). Whilst containing significant information in its own right, it is treated as 'background' in the attempt to quantify the Bragg scatter appearing in the same regions of reciprocal space. Its presence suggests that there is significant disorder within the tendon structure, with the maximum intensity being in the region of the intermolecular interference function. A later study [5] concluded that the diffuse scatter contains a significant contribution from the gap region where there is a lower packing density due to the missing molecular segment. Consequently, the remaining four segments have a greater tendency to motion [6] and/or reduced regularity in their molecular positioning. The molecules within the relatively well ordered overlap region have greater packing density (five chains) and the intermolecular crosslinks at the gap/overlap regions probably have much less

freedom for azimuthal motion and possess greater positional regularity than the gap region, which shows more extensive disorder. The consequences for the x-ray fibre diagram are that the contribution of the gap region to higher angle off-meridional reflections is attenuated. Despite this, the three-dimensional x-ray fibre diagram was successfully indexed on a triclinic unit cell after the strong near-equatorial reflection at 1.3 nm (a spacing close to that expected from near neighbor molecules), was shown to be split into three strong components and suggested a quasi-hexagonal packing of collagen molecules [3]. An improved set of unit cell parameters was later deduced by more detailed measurements [7,8].

A further complication to the interpretation of fibre diffraction diagrams in general and in the case of those arising from tendons, is that they are not single crystals, but are made up from millions of fibrils that are probably not all themselves crystalline since only 10% of the total off-meridional intensity arises from Bragg scatter [9]. Even here, since the collagen fibrils are not truly aligned with a spread of around 1-2 degrees from true parallelism, the Bragg reflections in the fibre diagram are often drawn out into arcs that overlap with other reflections. These two features present enough technical challenges, but in addition to these complications, the crystallographic unit cell is triclinic ($p1$) with its

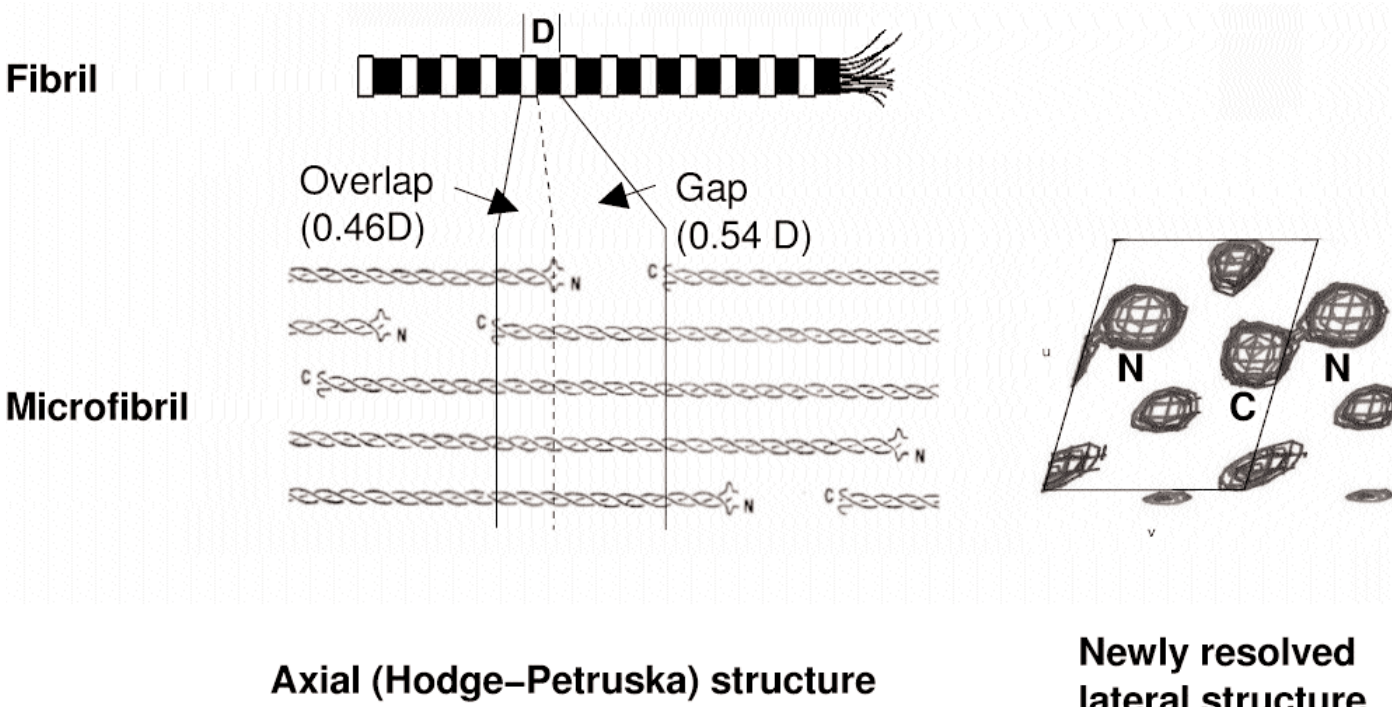


Figure 1: Axial and lateral molecular composition of the type I collagen fibril. N and C termini are labeled. The axial unit cell (D) is shown (left), as is an outline of the unit cell of the molecular packing structure (right). Molecular segments from a neighboring unit cell are shown (right) to better show the quasi-hexagonal nature of the packing structure and the corrugated pattern of the crosslinked N and C telopeptide containing molecular segments within the packing scheme.

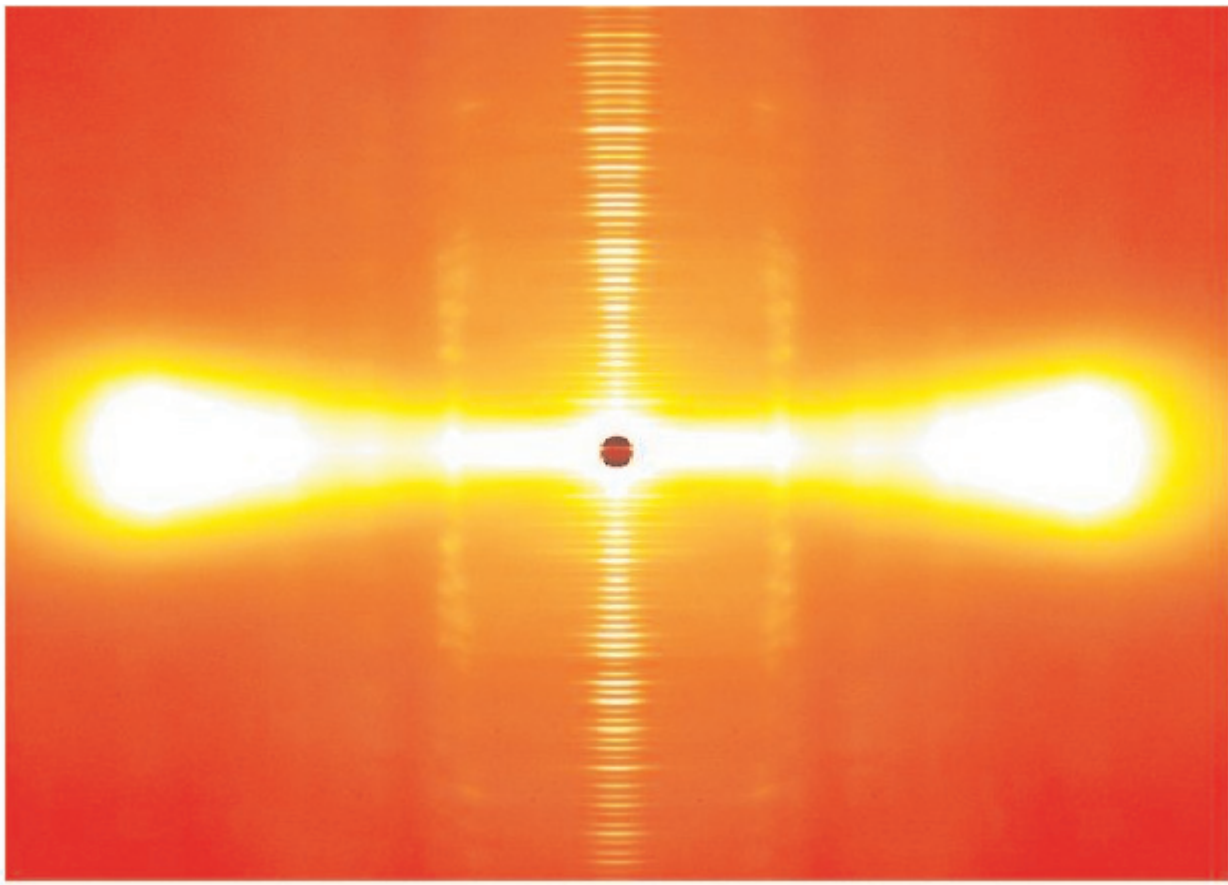


Figure 2: X-ray fibre diagram of rat-tail tendon, iodide derivative before data treatment.

(very) long axis (c) inclined at 5 degrees to the axis of the fibril. Finally, since the diffracting specimen is a fibre, the x-ray pattern is equivalent to a 360-degree rotational pattern from a single crystal.

Tackling the challenge

A great deal of improvement in the quality of x-ray diffraction patterns from collagen specimens has been made in recent years. The use of synchrotron radiation and new image treatment techniques have allowed the measurement of the intensities of the (h,k,l) reflections from native tissue and from isomorphous derivatives treated with iodine (which labels the tyrosine amino acids which only occur in the telopeptides) and gold which labels histidine, selected methionine and cystine residues (of which only the former two are found within the sequence of type I collagen). In these latter cases, it has been possible to improve markedly the visibility of weak Bragg reflections, that may be only barely visible or not seen at all, in the native pattern, but still enable quantitative interpretation of the data since these heavy atom treatments produce predictable staining patterns within a relatively small number of residue attachment sites [10,11].

Even so, several of the problems discussed above

had not, until recently, been dealt with. These were:

- a) Obtaining data of superior quality to allow the separation of the closely spaced Bragg reflections, (especially in the near-equatorial region) from the diffuse scatter.
- b) The development and application of techniques to separate and determine the intensity of reflections that overlap in the off-meridional parts of the fibre diagram.
- c) Repeating this process for two or more isomorphous derivative proteins, the data from which would then be used to determine the three-dimensional location of binding sites, and eventually the native phases.

Improving data quality

Several preliminary experiments were performed at beamline 7.2, Synchrotron Radiation Source (SRS) Daresbury UK, and beamline ID2, European Synchrotron Radiation Facility (ESRF) Grenoble, France, in the process of developing stain techniques and in parallel with the determination of a high angle one-dimensional structure of collagen [10]. Eventually, we were able to obtain data sets of

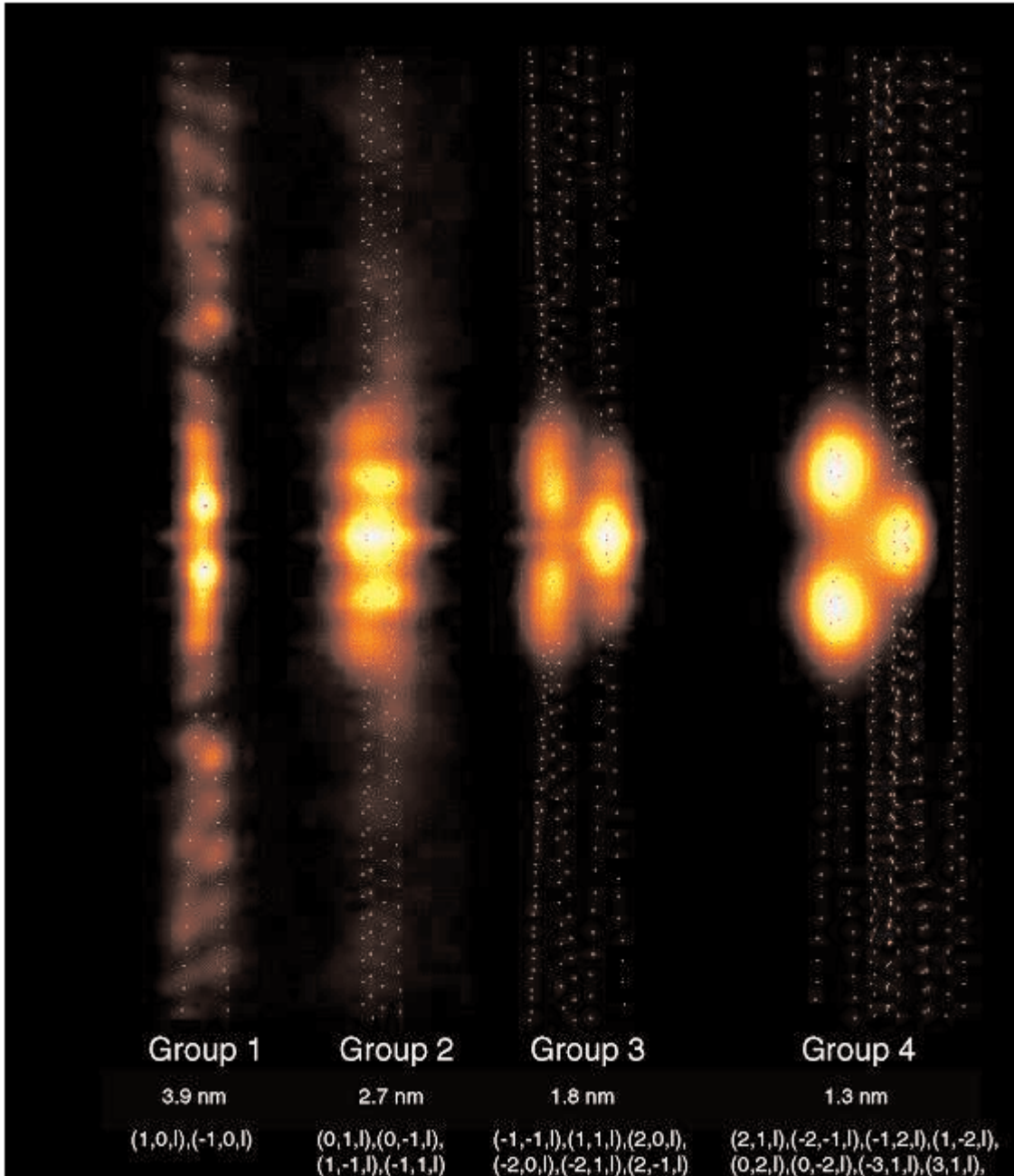


Figure 3: Portion of the fibre diagram showing Figure 2 after background subtraction. Bragg positions are marked and the groups 1-4 (with hkl reflections and reciprocal space ranges listed) are also labelled. Adapted from Orgel et al., 2001.

sufficiently high quality during an extended experiment at the BioCAT ID 18 beamline, Advanced Photon Source (APS), Argonne Illinois USA. In these fibre diagrams, the low beam divergence, small beam size, and clean optics of this instrument [12] have greatly reduced the parasitic scatter and the associated background and achieved a high order to order resolution (Figure 2, and Figure 3). The diffuse scatter of the pattern due to the inherent disorder contained within the samples remains, and was dealt with as described below.

A camera length of 1026 mm (at $\lambda = 1.003 \text{ \AA}$) was chosen to maximize the number of pixels over which fibre diagram extended (i.e. improve the resolution in Q space), whilst maintaining the presence of the

reflections at higher Q-space values needed solve the phase problem within the same diffraction pattern. This optimization would later prove critical during data extraction (see Table 1). The removal of the remaining 'background' (diffuse scatter), was performed by methods used previously [8,9], but worthy of brief review here:

The suite of programs FIT2D [13] was used to remove the diffuse scatter from the low-angle diffraction pattern background. This background was assumed to be smooth and regions containing background were presumed to be distinguishable from regions that did not. One of the drawbacks of this assumption is that in areas containing Bragg

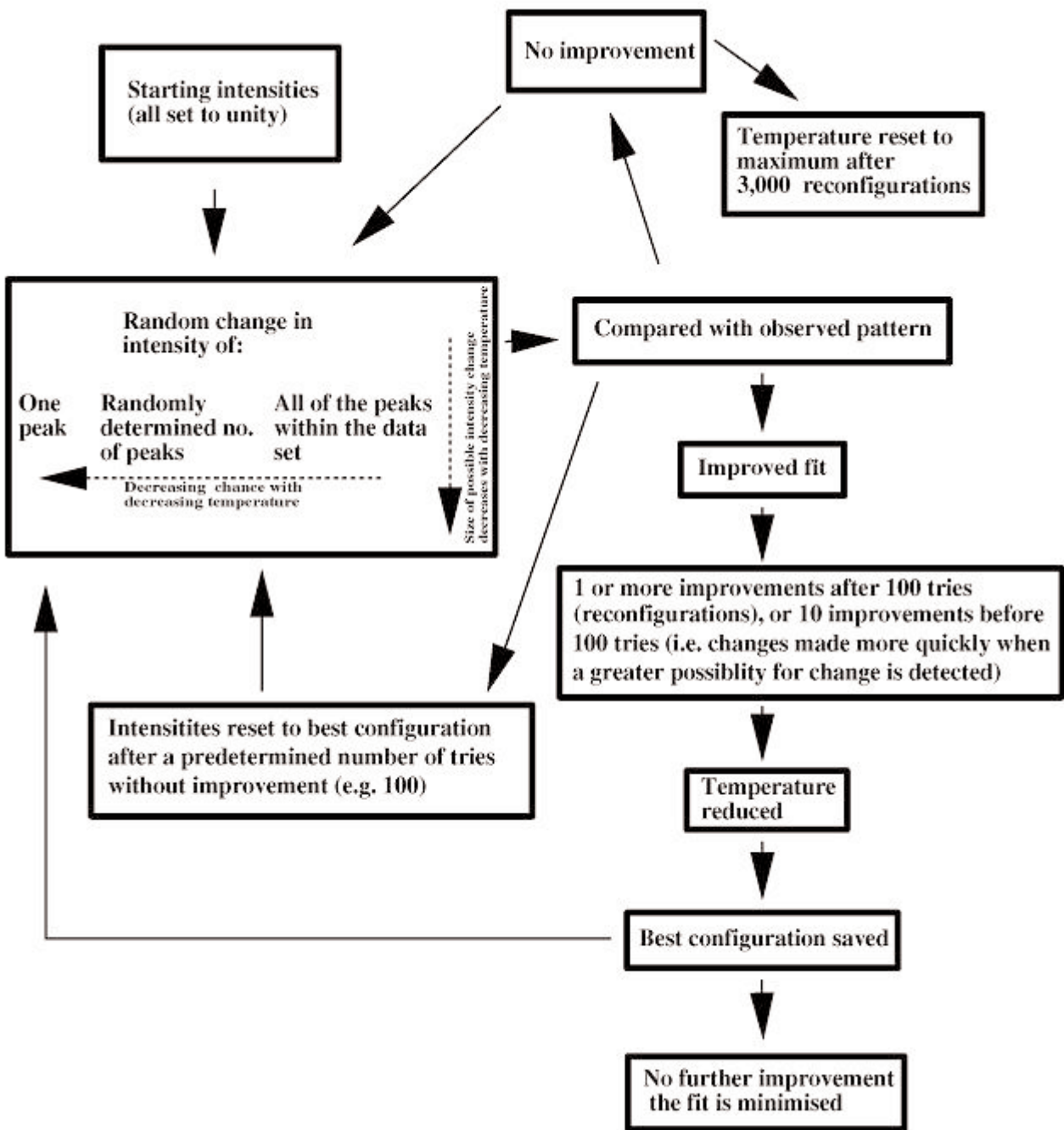


Figure 4: Schematic showing the operation of the simulated annealing algorithm that was used to determine the intensities of the native and two isomorphous derivative samples.

scatter that happens to be indistinguishable from the underlying background, the smooth background polynomial would model only a background function. Hence any Bragg scatter (the sought after data) in such areas would be partially or completely removed in the background subtraction process. The likely-hood is that weaker Bragg intensity reflections will be effected (reduced or removed) in this process more than stronger reflections will be. However, the diminished influence of the weaker reflections in the phase calculation is preferable to the over-representation of reflections that happen to be located on top of a highly sloping background that would otherwise adversely effect the phase and electron density calculations if left uncorrected.

Interpolation was performed within FIT2D in a user-defined area of the pattern (between approximately $R = 0.15$ to 1.0 nm^{-1} and $Z = 0.0$ to 0.4 nm^{-1}), with pixels containing Bragg peak data masked (excluded from the calculation). This area of the diffraction pattern contains the main part of the small-angle off-meridional data. Surface polynomial functions (two-dimensional Chebyshev polynomials) were used to fit a background model to the data. Generally, the area fitted would be larger in the Y direction than the X, hence the X polynomial would be in the order of 3-5 whilst the Y would be approximately 5-10. In either case, the polynomial order would always be much smaller than the number of pixels within the

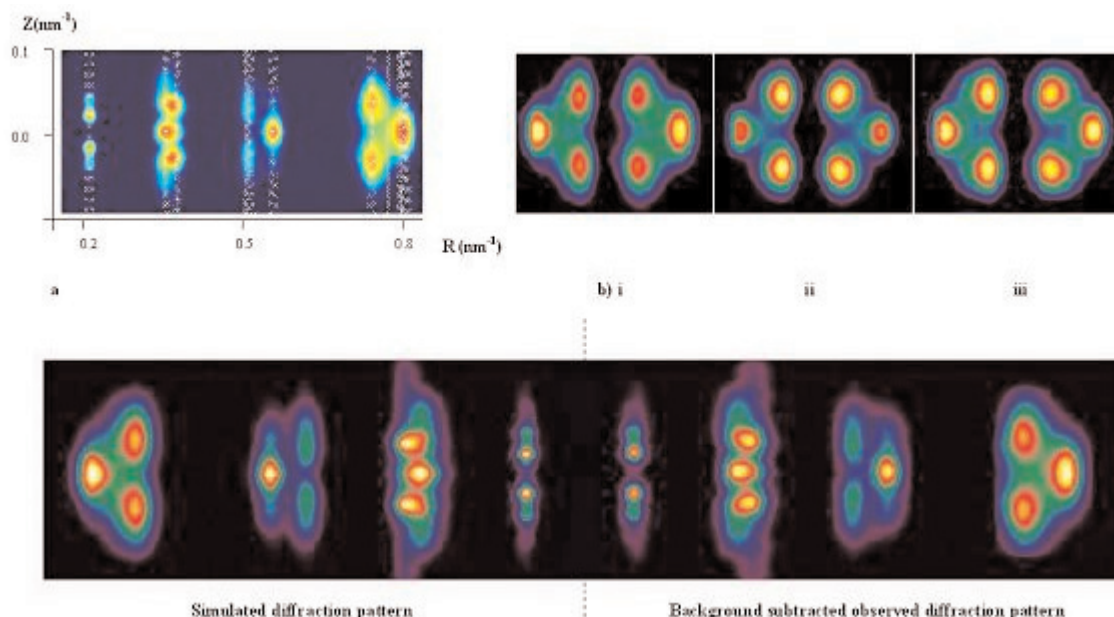


Figure 5: Comparisons of background-subtracted portions of the observed fibre diagrams with the computer generated patterns used in the determination of the overlapping reflections

- a) A background subtracted low angle off-meridional region of the native fibre diagram, the position of the Bragg reflections are marked with X's.
- b) Group 4 rowlines that contain the highest degree of Bragg overlap within the fibre diagram. This shows the high degree of agreement between the observed and the computer generated patterns; the observed is on the right, the simulated on the left of each of the following:
 - i. Native, ii. Iodide derivative, iii. Gold chloride derivative.
- c) Right, The observed background subtracted image shown in a). Left, the corresponding simulated low angle diffraction pattern. This is the region containing the highest degree of Bragg reflection overlap, and, for the native data set that shows the highest percentage error between that of the observed and simulated patterns (3.00%). Adapted from Orgel et al., 2001.



Figure 6: Tilted molecular segments of the overlap region

The molecular tilt of the collagen molecular segments of the overlap region are observed to follow a vector approximately parallel to the line (0,0,0) to (0,0.2,1) (u,v,w ; as in Fraser et al. [4]). This corresponds to a tilt of about 5 degrees relative to the c-axis of the unit cell. The molecular segments in the overlap region follow parallel paths. The formation of intermolecular crosslinks at the interfaces of the overlap/gap regions (at the telopeptides), ensures that the overlap region is well ordered, particularly in the plane of the telopeptides in contrast to the disordered state of the gap [5] see also [16]. The overlap region is illustrated here and the c-axis compressed by 5 times to show clearly the tilt of the individual molecular segments. The electron density is the same as that seen in Orgel et al., 2001, although the view is similar, the sigma levels (density scale) are slightly lower to contrast gap and overlap regions.

interpolation region.

We assumed that we had achieved a suitable background model when the residual between the model and observed data was minimal [13]. We used the lowest order polynomial that fitted these criteria, so that the rowlines were seen to be superimposed on a suitably flat background. This process was made considerably easier because of the improved quality of the fibre diagrams.

Extracting the data

Wess *et al.*, [9] had previously developed a model for fitting the group 1 row-lines (where group n (n is an integer 1-4) refers to the groups of row-lines in the collagen fibre diagram, 1 being closest to the meridian, 4 being furthest away, see Figure 3) using a two dimensional Gaussian function for each peak, the coordinate positions of each peak being calculated from the unit cell parameters of Wess *et al.*, [8]. We adopted and further developed this strategy using a computer generated diffraction pattern to fit the background-subtracted observed diffraction pattern, the minimisation between the two being driven by a simulated annealing method developed from the original concept described by Metropolis *et al.*, [14].

An algorithm was written following these principles, applying the annealing analogy to fitting a model diffraction pattern to the observed diffraction pattern, (the algorithm is summarized in the schematic flow diagram of Figure 4), each peak of intensity being treated as an atomic position in the annealing analogy. The coordinate positions of the intensities in the diffraction pattern were fixed according to the unit cell parameters previously described [8].

Three kinds of intensity change (analogous to atom redistribution in the annealing analogy) were allowed for each peak of the model pattern: 1) A random intensity change between the minimum and maximum pixel values of the observed pattern, of one randomly determined peak. 2) One random intensity change for a selected sequential series of peaks of random length. 3) One random global intensity change for all the peaks being fitted.

The model system had an imposed temperature, just as in the thermodynamic analogy. At high temperature, greater intensity changes were allowed as well as more wide spread change to the number of

peaks affected. As the temperature dropped, the chances of the options 2 or 3 (above) occurring diminished, reflecting the fact that, as in the thermodynamic analogy, widespread changes affecting arrays of atoms would be less likely to occur as the liquid cooled.

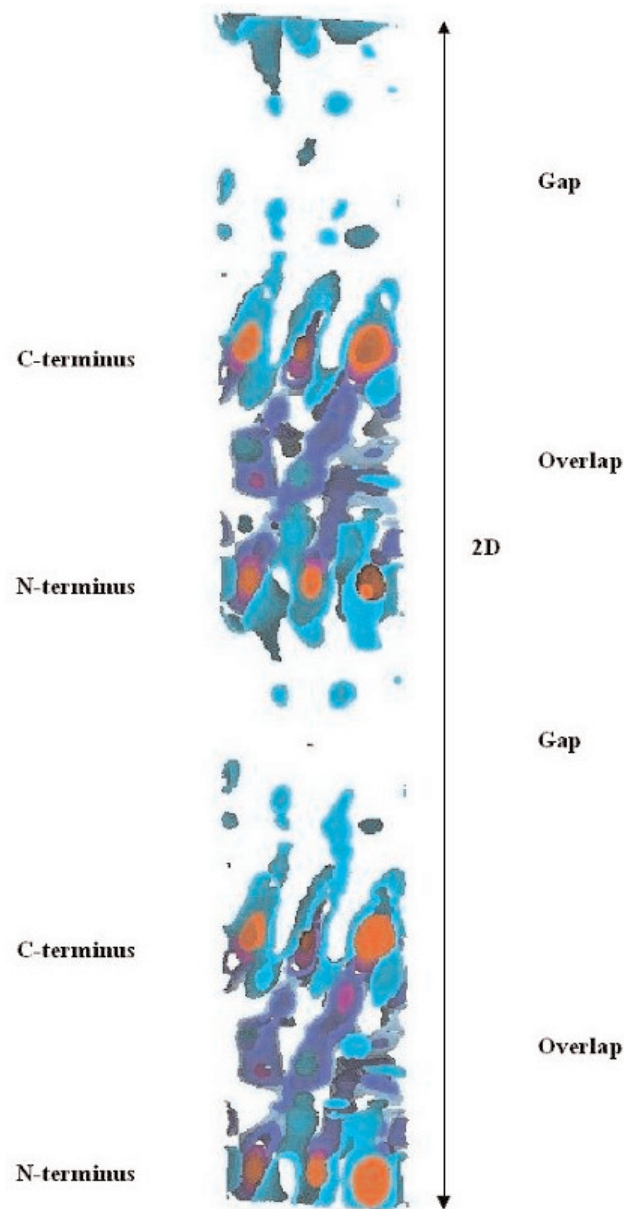


Figure 7: Two unit cells (along long unit cell axis) showing ordered overlap and disordered gap regions.

The molecular packing arrangement is most clearly discernible at the axial level of the telopeptides, (shown as the C terminus and N terminus regions on the figure) but is also discernible within the rest of the overlap region. The gap region shows a large degree of lateral disorder of the molecules in the lower packing density gap region, as predicted in several model studies [5,7,16]. Disorder is commonly encountered in macromolecular crystallography in regions of crystal structures subject to thermal motion (such as chain loops), and was seen to a similar degree in the study of tropomyosin [18]. The electron density is the same as that seen in Orgel *et al.*, 2001, although the view is similar the sigma levels (density scale) are slightly lower to contrast gap and overlap regions.

Source	ID18 BioCAT undulator beamline(APS)
Beamsize (unfocused)	0.8 mm x 3.6 mm (at sample) [12]
Flux	1.5-5 x 10 ¹³ ph/s @ 100 mA
Pathlength	1026mm
Wavelength	1.003 Å
Detector	Fuji BAS V image plates with a Fuji BAS2500 reader
Data sets	One native and two isomorphous derivative fibre diagrams
Derivatives	iodide and gold chloride
Unit cell dimensions	triclinic a=39.97 b=26.95 c=677.9 Å
Unit cell angles	$\alpha=89.24^\circ \beta=94.59^\circ \gamma=105.58^\circ$
Space group	P1
Resolution limits (Å)	5.4 meridional 10.0 equatorial
Observed unique reflections	410 (124 meridional 286 equatorial)
Figure of merit	0.4

Table 1: Experimental details. Adapted from Orgel *et al.*, 2001.

Data set	Group	Average error (%)			
		1	2	3	4
Native	3.02	3.23	4.21	1.57	2.99
Iodide	1.56	0.97	1.69	1.48	2.08
Gold	1.34	1.64	1.55	0.64	1.52

Table 2: Percentage error between simulated patterns and the observed fibre diagrams. Adapted from Orgel, *et al.*, 2001.

The algorithm would run until it was assessed that no further minimisation would occur. The success of each cycle and the final minimisation was judged through the use of the Root-mean-square difference in each pixel between the observation and simulation. Only the essential parts of the fibre diagram were calculated during the minimisation these being: all of the Bragg reflections, their Gaussian function and a small amount of the flat background surrounding each peak (around 0.09% per reflection of the total data area). This was to improve the speed of the algorithm only requiring it to make 1/100 of the calculations it would otherwise have needed to make if it were calculating the whole of each fibre diagram (most of which had already been assessed as flat after background subtraction of the observed data, described above). The R-factor was calculated to assess the fit of each simulated pattern to its respective observed pattern as follows:

$$R = \sum_i |F_o(i) - F_c(i)| / \sum_i F_o(i)$$

Where F_o and F_c are respectively the observed and calculated intensity of each pixel.

The final combined error for the native and the two derivative patterns was judged to be less than 3.0%. (Figure 5 and Table 2). This low level of error gave us sufficient confidence in the intensities so derived, to proceed with the phasing process. The process of phasing would test the real success of these methods; too much error in the assessment of the intensities could make it impossible to determine the phases accurately enough to be able to visualize the molecules and elucidate the packing system.

Determining the phases

As in many crystallography experiments, the determination of the structure factor phases can be the hardest and most laborious part of the data processing, especially when the sites of heavy atom

attachment are not known. Fortunately, data provided from the high angle one-dimensional structure of Orgel *et al.*, [10], identified the putative residues, their axial location, and the molecular segments within which they were bound. This greatly reduced the burden of heavy atom searching to that of looking for heavy atom peaks in difference Patterson maps corresponding to the axial distance between the telopeptide regions (the major sites of heavy atom attachment). The two derivatives, gold chloride and iodide treated samples each possessed two major sites for heavy atom attachment. These were clusters of residues that accept heavy atom stain, located, for the gold chloride derivative, at the N-terminus within molecular segment 5 and at the C-terminus within molecular segment 1, and for iodide derivative: at the N-terminus within molecular segment 1, and at the C-terminus within molecular segment 5 (see reference 10). Difference Patterson maps were calculated for the packing structure at the axial separation of the telopeptide regions (N and C-termini) of 0.33-0.41 w (fractional unit cell coordinates). The resulting vectors for the gold chloride and iodide derivatives were respectively: u=0.2, v=0.4 and u=0.05, v=0.25 (where u and v are fractional unit cell coordinates in Patterson space).

These values and the corresponding Patterson maps were used in conjunction with autocorrelation functions (calculated using XtalView programs [15]) to locate the three-dimensional positions of the molecular segments 1 and 5. When agreement was reached, these coordinates were used to calculate phases that were refined using the Xheavy program of the Scripps Institute crystallographic software suite XtalView [15].

The first true x-ray diffraction visualisation of a semi-crystalline natural fibre

The end result is shown in part in Figures 6 and 7. The molecular segments within the overlap region are clearly visualized (particularly at the telopeptide regions), whereas little is seen of them within the gap region. In cross section, the quasi-hexagonal packing scheme is revealed, (with the intermolecular cross-linking telopeptides identified in the difference Fourier maps, see [1]). The crosslinking pattern and its significance to the supermolecular structure is discussed elsewhere [1], but it is significant to see that the molecular segments of the overlap region are tilted with respect to the unit cell axis, as predicted by Fraser *et al.*, [7]. This is testament to the

successful extraction of the data from an extremely difficult system.

The successful generation of an interpretable electron density map that fits the consensus elements of several model studies [3-5,7-9] is compelling proof of the validity of the methods used to extract the intensities. It is still important, however, to continue to improve the quality of the electron density map. Work has already commenced to attempt to obtain improved diffraction patterns from fibrils that are cryofrozen. The freezing of the tendons in this way will allow the sample to be bathed in the x-ray beam for longer to obtain a higher signal to noise ratio, and further reduce the thermal disorder of the molecular system within the sample. It may be possible to reduce the disorder of the fibrillar packing arrangement using a series of freezing/partial thawing steps to anneal the packing system to a lower energy state.

An altogether different approach, still using x-ray fibre diffraction techniques, involves attempts to obtain diffraction from a *single* fibril. This approach would be closer to true single crystal macromolecular crystallography, and would, if it can be made to work, produce diffraction patterns with improved spatial resolution of the Bragg peaks (reduced range of fibril orientations within the fibre - only one fibril). Initial experiments (at beamlines ID 22 and 18F at the ESRF, Grenoble, France) have shown the necessity of cryofreezing the sample whilst using powerful x-ray beams of very small cross-sectional area (approximately $0.75 \mu\text{m}^2$). As the number of unit cells sampled by the incident x-ray beams is diminished in samples of this size (micron scale), the exposure time needed to collect data is increased (around 10-100 fold for this particular system). The cumulative effect of focused, high-brilliance synchrotron beam and tiny samples is the rapid destruction of delicate specimens, and inspiration will need to be drawn from the related field of macromolecular crystallography for techniques that preserve the life-span of samples over the extended time needed to collect data.

Both of these techniques involve treating the collagen sample in ways that are non-physiological. It is possible that the freezing of samples in the annealing studies, or the disruption of the sample to obtain single fibrils, would fundamentally change the molecular packing arrangement within the fibril. Solutions devised from these and other means,

however, can now be compared directly to the visualisation of the hydrated native protein presented here. This represents the first structure determined by MIR for any natural fibre, and the first three dimensional visualisation of the three-dimensional, periodic lateral packing structure of collagen.

Correspondence and requests for materials should be addressed to J.Orgel
(e-mail: jorgel@tigger.cc.uic.edu).

References

- [1] Orgel, J.P.R.O. Miller, A. Irving, T.C. Fischetti, R.F. Hammersley, A.P. and Wess, T.J. The *in situ* three dimensional packing structure of type I collagen". *Structure*, **9**, 1061-1069. (2001).
- [2] Hulmes, D.J., The collagen superfamily - diverse structures and assemblies. *Essays Biochem.* **27**, 49-67. (1992).
- [3] Hulmes, D. J. S., & Miller, A. Quasi-hexagonal molecular packing in collagen fibrils. *Nature*. **282**, 878-880 (1979).
- [4] Fraser, R. D. B., Macrae, T. B. & Miller, A. Molecular packing in type I collagen fibrils. *J. Mol. Biol.* **193**, 115-125 (1987).
- [5] Hulmes, D.J.S., Wess, T. J., Prockop, D. J., & Fratzl, P. Radial packing, order and disorder in collagen fibrils. *Biophys. J.* **68**, 1661-1670 (1995).
- [6] Torchia D.A., Solid state NMR studies of molecular motion in collagen fibrils. In *Methods of Enzymology*, **82**. 174-186. Cunningham, L., and Fredriksen, D., eds. Academic Press, New York (1982).
- [7] Fraser, R. D. B., MacRae, T. P., Miller, A., & Suzuki, E. Molecular conformation and packing in collagen fibrils. *J. Mol. Biol.* **167**, 497-521 (1983).
- [8] Wess, T. J., Hammersley A., Wess L., & Miller A. Type I collagen packing, conformation of the triclinic unit cell. *J. Mol. Biol.* **248**, 487-493 (1995).
- [9] Wess, T. J., Hammersley A., Wess L., & Miller A. Molecular packing of type I collagen in tendon. *J. Mol. Biol.* **275**, 255-267 (1998).
- [10] Orgel, J.P., Wess, T.J., & Miller, A. The *in situ* conformation and axial location of the intermolecular cross-linked non-helical telopeptides of type I collagen. *Structure*. **8**, 137-142 (2000).
- [11] Bradshaw J.P., Miller A., & Wess T.J. Phasing the meridional diffraction pattern of type I collagen using isomorphous derivatives. *J. Mol. Biol.* **205**, 685-694 (1989).
- [12] T.C. Irving, R. Fischetti, G. Rosenbaum, and G. B. Bunker (2000). Fiber Diffraction Using the BioCAT Undulator Beamline at the Advanced Photon Source. *Nuclear Instruments and Methods(A)* **448**, 250-254.
- [13] Hammersley, A. P. FIT2D V9.129 Reference Manual V3.1. Grenoble: European Synchrotron Radiation Facility, 1998, www.esrf.fr (or through <http://biocat1.iit.edu/FIT2D/>).
- [14] Metropolis N., Rosenbluth M., Teller A., & Teller E. Equation-of-state calculations by fast computing machines. *J. Chem. Phys.* **21**, 1087 (1953).
- [15] McRee D.E., *Practical Protein Crystallography*, Academic Press, San Diego CA. (1993).
- [16] Bailey A.J., Light N.D., & Atkins E.D.T. Chemical cross-linking restrictions models for the molecular organization of the collagen fibre. *Nature*. **288**, 408-410 (1980)
- [17] Woodhead-Galloway, J., & Machin, P., Modern theories of liquids and the diffuse equatorial x-ray scattering from collagen. *Acta Cryst. A*. **32**, 368-372 (1976).
- [18] Phillips G.N., Fillers J.P., and Cohen C. Motions of tropomyosin. Crystals as metaphor. *Biophys. J.* **32**, 485-502 (1980).

Real Time SAXS/Stress-Strain Studies of Thermoplastic Polyurethane - A fibre diffraction approach to a non-crystalline material

D J Blundell¹, C Martin¹, A Mahendrasingam¹, W Fuller¹ and G Eeckhaut²

1. Dept of Physics, Keele University, Staffordshire ST5 5BG, UK

2. Huntsman Polyurethanes, Everslaan 45, B-3078 Everberg, Belgium

Received November 2001; accepted in revised form 14th March 2002.

Introduction

Elastomeric polyurethanes are synthesised from blocks of flexible, "soft" units linked together with rigid, "hard" blocks. Incompatibility between hard and soft blocks leads to phase separation giving rise to two-phase morphologies with an approximate 10nm spatial correlation which can be monitored by SAXS.

Despite their versatility for a wide range of uses, applications of polyurethanes are still limited by their relatively high mechanical hysteresis compared with other elastomers. This hysteresis and the associated mechanical loss processes can be partly attributed to the breakdown and reformation of the phase structure during mechanical cycling.

This paper focuses on one aspect of an on-going programme between Keele University and Huntsman Polyurethanes. It involves simultaneously measuring the SAXS patterns and the stress during tensile deformation in order to follow the changes in morphology and identify effects associated with mechanical loss.

It is currently believed that phase separation (on cooling or during solvent evaporation) generally occurs via spinodal decomposition followed by ripening [1-3]. The exact nature of the final morphology is uncertain and depends on the fabrication route and on the molecular formulation. Several approaches are being used to elucidate the nature of both the starting morphologies and how the morphologies change during deformation. This paper describes a novel approach to the analysis of two dimensional SAXS patterns and is illustrated with

recent results from one particular polyurethane. The analysis is based on an affine deformation scheme in which some of the ideas are borrowed from fibre diffraction crystallography.

Experimental Results

The particular polyurethane used in this study had a soft segment derived from an a,w dihydroxy poly(tetrahydrofuran) of molecular weight 1000. The hard segments consisted of mixtures of toluene diisocyanate, 4,4'-methylene phenylene diisocyanate and ethanolamine in a molar ratio = 2/1/2. The volume fraction of the hard segments in the final polyurethane was approximately 0.36.

Specimens in the form of 0.5mm thick sheets were deformed in a purpose built stretching camera [4] mounted on beamline 16.1 at the SRS in Daresbury using the Fast 2D detector to monitor the SAXS. The specimen was subjected to a continuous cycle of extensions and retractions. Figure 1 shows the variation in tensile force during the cycle in which the SAXS patterns were recorded with sequential 3.2 second frames. Figure 2 shows the same force data plotted against draw ratio and illustrates the hysteresis effect during the cycled oscillations. The draw ratios in these experiments have been derived from grating markings on the sample using a video image that had been recorded simultaneously with the force and SAXS patterns. It will be noted that the shape of the force variation during the first extension indicates a mechanical yield process followed by a more linear response at around the point corresponding to frame 10 where the draw ratio is about 1.25. Selected SAXS frames from this

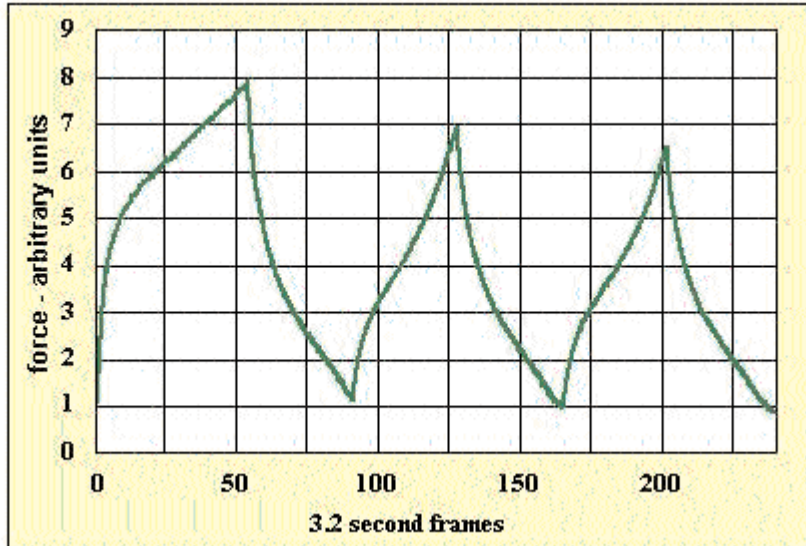


Figure 1: Variation in tensile force during extension and retraction cycle.

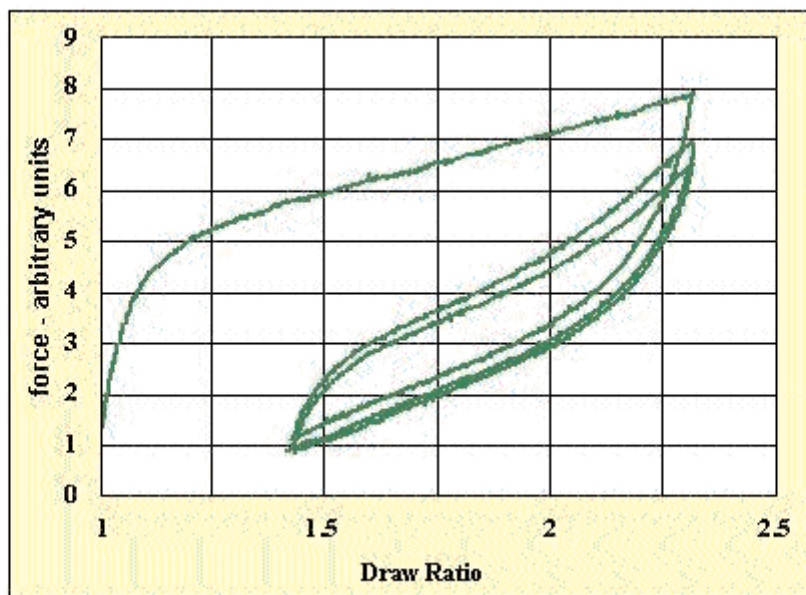


Figure 2: Tensile force plotted against draw ratio showing hysteresis effect.

experiment during the first tensile extension are illustrated in Figure 3.

The initial SAXS pattern from the undeformed sample in frame 1 is an isotropic halo with a peak intensity equivalent to a Bragg periodicity of 10.4nm. During the first tensile extension, the diffraction halo intensifies on the meridian and becomes progressively elliptical in shape. Confirmation that the halo maximum follows the locus of an ellipse (ie. $x^2/a^2 + z^2/b^2 = 1$) can be seen from plots of x^2 vs z^2 as in the examples in Figure 4, where z is in the vertical draw direction and x is in the lateral direction. This paper is primarily concerned with describing an analytical method for interpreting the shape and intensity distribution of these elliptical patterns during this first tensile extension. Further papers will address the

ramifications of this interpretation in more detail and will also deal with the subsequent changes in the patterns during retraction.

Affine Deformation

An elliptical locus can be derived from a circle by an affine deformation; ie a deformation in which all x and y coordinates are systematically multiplied by constants f_x and f_y respectively. It is therefore of interest to enquire whether the elliptical halo is directly linked with an affine deformation of the two phase structure in the specimen. To a good approximation, polyurethane elastomers deform at constant volume. Thus during uniaxial tensile deformation of draw ratio λ , the length of the sample will change by λ while the lateral dimensions will change by a factor of $1/\sqrt{\lambda}$. If the two phase

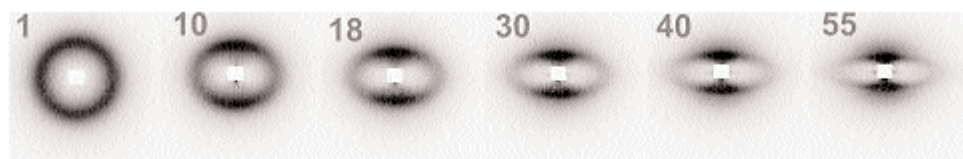


Figure 3: Selected SAXS patterns for frames 1, 10, 18, 30, 40 and 55 during the first extension of the deformation cycle.

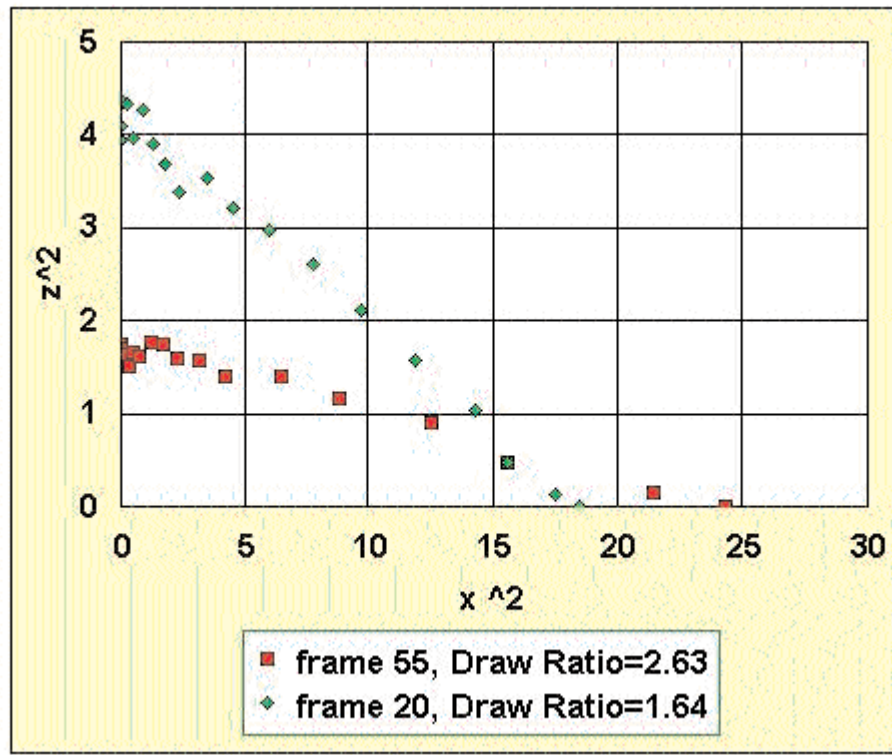


Figure 4: Example plots of loci of intensity maxima around the elliptical pattern for frames 20 and 55.

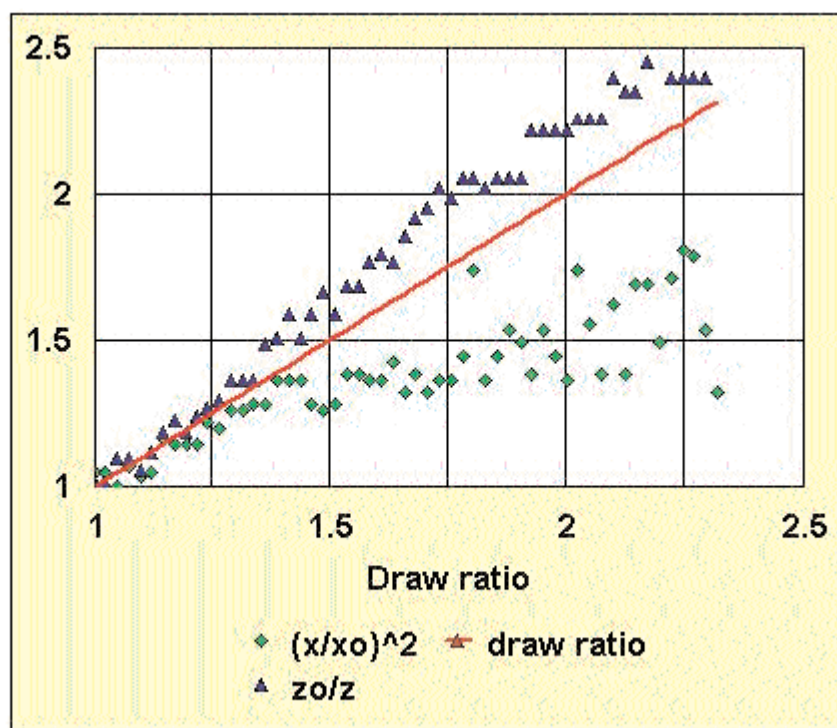


Figure 5: Plots of z_0/z and x^2/x_0^2 versus draw ratio, showing agreement with affine deformation scheme up to $l \sim 1.25$.

microstructure follows an affine deformation scheme related to the overall sample shape then the x and z coordinates of a vector between any two structural elements in real space will be modified by the same factors. In such a situation, the corresponding intensity function in reciprocal space will also deform affinely but with factors that are the inverse of those in real space. Thus x and z coordinates of vectors in reciprocal space will be changed by factors of $1/\lambda$ and $\sqrt{\lambda}$ respectively. If the circular halo of the undeformed specimen has a radius x_o ($=z_o$) then $x/x_o = \sqrt{\lambda}$ and $z/z_o = 1/\lambda$. This hypothetical situation can be partially tested on the experimental data by plotting the two parameters $(x/x_o)^2$ and z_o/z versus l as in figure 5. The data points closely follow the value of λ up to a draw ratio of around 1.25. Beyond this the data points diverge and indicate a larger degree of ellipticity than that predicted for affine deformation. The point of the divergence corresponds to the onset of the more linear response in Figures 2 and 3 and suggests there may be a link with the way in which the microstructure deforms.

Up until this point there is therefore an indication that the main features of the microstructure are deforming in a way that is related to an affine scheme. One needs to examine the implications of this for the nature of the phase morphology. In a true affine deformation, every feature and shape of the phase morphology would need to deform in an affine manner. In an associated way all the features of the

corresponding intensity function in reciprocal space would undergo a reciprocal affine deformation. Thus a circular diffraction halo with uniform intensity would deform to an oblate ellipse that also had a uniform intensity. However the observed elliptical halos in figure 3 up to frame 10 do not have a uniform intensity but exhibit an intensification on the meridian. One can conclude therefore that, despite the ellipticity being consistent with affine deformation, the shapes of the microphases are not themselves following the true affine scheme.

Statistical Particulate Model

The above conclusion is not surprising if one bears in mind the composition of the polyurethane elastomer. It is unrealistic to expect the above true affine model to hold since the hard and soft phases have quite different mechanical properties. The hard microphase regions will resist changes in shape while the soft phase will tend to change shape to accommodate the hard phase. When the hard phase is in the minority, as in this specimen, the degree of connectivity of the hard phase will be reduced. One would therefore expect that the larger concentrations of hard phase will be more able to retain their original shapes during the deformation of the macroscopic sample. It is therefore of interest to consider a modified affine model in which the hard microphase regions can effectively be represented by separated particulate inclusions embedded in a continuous soft phase and to ignore any minor

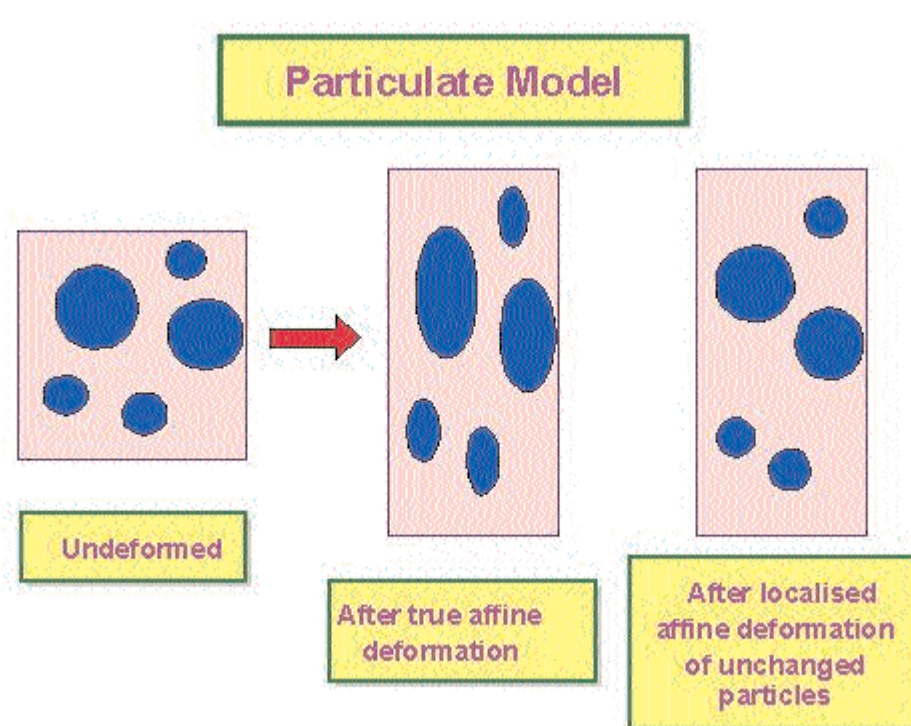


Figure 6: Illustration of particulate model showing differences between pure affine deformation and modified affine deformation.

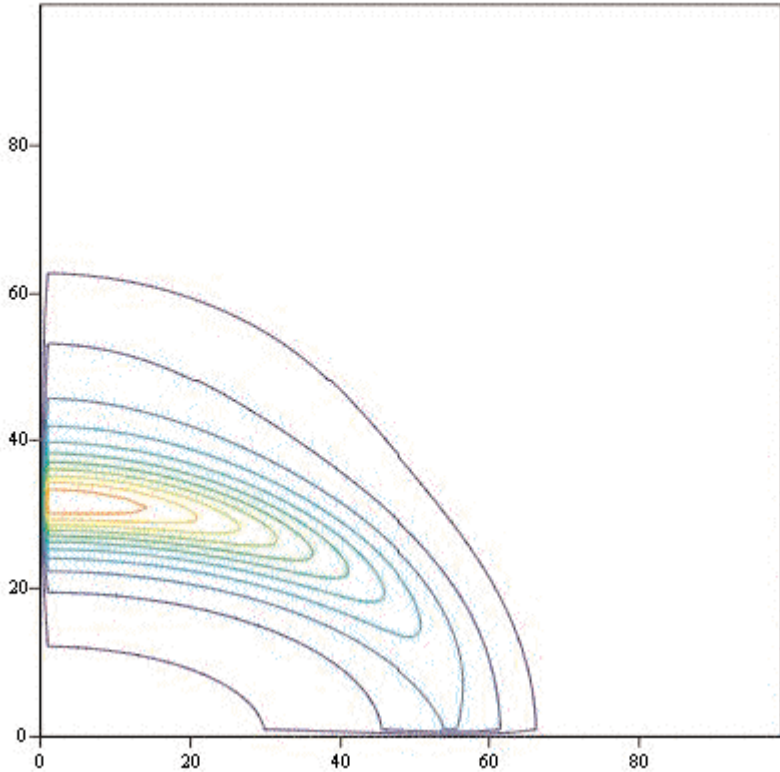


Figure 7: Predicted SAXS pattern for a model example of spherical particles on a deformed statistical lattice.

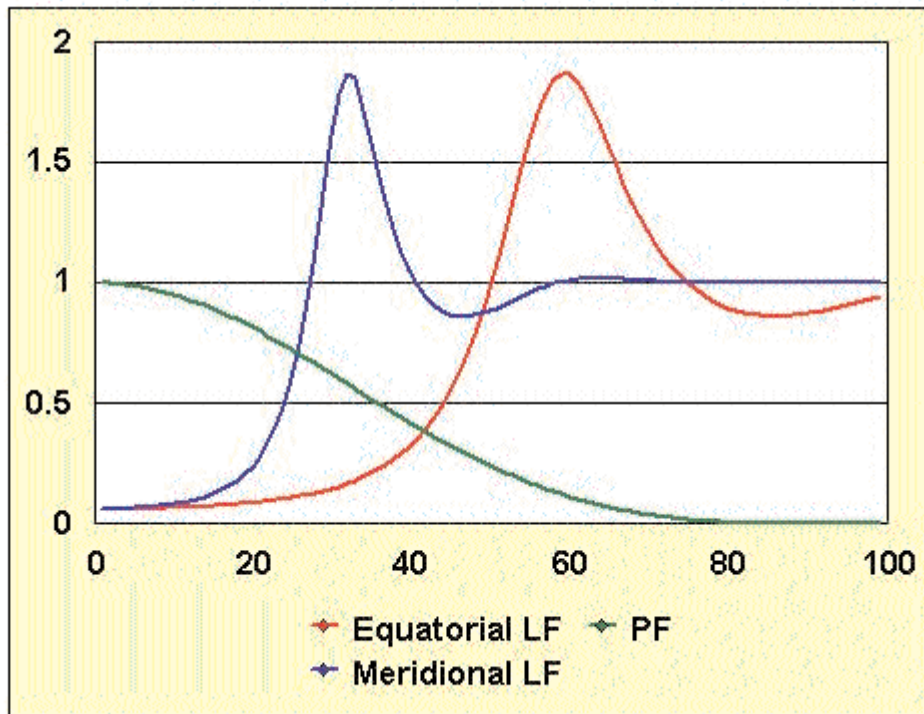


Figure 8: Contributions of LF and PF factors for predicted pattern in figure 7.

regions of connectivity. Assume therefore that during deformation, the relative positions of the hard phase particles with respect to each other move affinely but the shapes of the particles remain unchanged. In this model the particles represent the main concentrations of hard phase and will vary in shape and size. The contrast between true affine and the modified affine deformation is shown in Figure 6 for the simplified case of spherical particles.

The diffraction halo will result from the interference between waves scattered from this statistical arrangement of particles. Making the analogy with standard crystallography, one can consider the particles to be located on statistical lattice points. The observed intensity along any given scattering direction will therefore be the product of a Particle Function (*PF*) and a Lattice Function (*LF*). In the

undeformed, isotropic state, LF will be centrosymmetric. During deformation the statistical lattice points will move according to the affine scheme. The LF will then vary with direction in such a way that the profile of LF will deform in an affine manner that is the reciprocal of the deformation of the statistical lattice. In contrast, PF will be isotropic and will remain unchanged during deformation. Accordingly the peak intensity of the observed intensity halo in any particular direction will be determined by the value of PF at the peak scattering vector. This is analogous to the crystallography of perfect crystals where the intensity of each discrete crystalline reflection is due to the sampling of the structure factor of the unit cell at each reciprocal lattice point. As an illustrative example of a statistical lattice consider the simple case in which the periodic regularity in any particular direction is represented by a one dimensional lattice factor (LF) in the form of a Zernike-Prins term.

$$LF = \frac{(1 - |F|^2)}{(1 - 2.|F|.\cos(qd) + |F|^2)}$$

where

$$F = \exp\left(\frac{-\pi^2 q^2 g^2 d^2}{2}\right)$$

and d is the periodic repeat and g is the fractional deviation of the distribution of projected distances

between scatterers.

Also for simplicity, assume that the hard phase inclusions can be represented by identical spheres of radius R with a particle scattering factor,

$$PF = \frac{9.(\sin(Rq) - R.q.\cos(Rq))^2}{(R.q)^6}$$

The predicted intensity is the product of the two terms. During deformation, the periodic distance d will vary with direction according to an affine scheme causing the q -radius at the peak of the halo to vary with direction in a reciprocal way. The intensity around the halo will be determined by the value of PF at each peak q . Figure 7 shows one quadrant of a predicted SAXS pattern expected for an affine deformed sample for the particular case where:-

the sphere radius is 0.4 of the average periodic repeat,
the deviation g is 0.25 of the periodic repeat and
the draw ratio $\lambda = 1.4$.

Figure 8 illustrates how the LF and PF contribute to the intensity of the elliptical halo along the meridian and equator axes.

Figure 7 reasonably reproduces the features of the observed SAXS patterns. If one accepts this approach for interpreting the experimental patterns

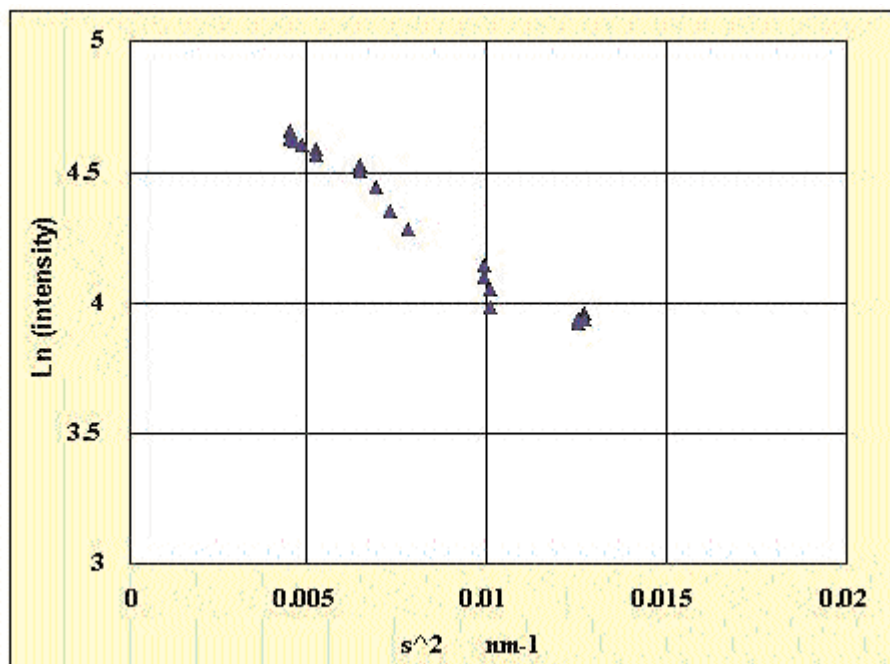


Figure 9: Variation of peak intensity around ellipse for frame15, plotted in the form of a Guinier Plot.

then one can consider the corollary of the argument that the intensity variation around the ellipse gives direct information of the structure factor of the particles located on the statistical lattice. (Interestingly, the exact form of the Lattice Factor does not need to be known providing the positions of the statistical lattice points deform affinely.) Figure 9 shows the variation of intensity as a function of the square of the radii for frame 10, plotted on a log scale. This is equivalent to a Guinier plot for the scattering particles [5] plotted between the limits of the major and minor axes of the elliptical halo. A linear fit to these points indicates that the effective radius of gyration of the particles is 2.7 nm. Identical spherical particles with this radius of gyration would have a diameter of 6.9 nm. Bearing in mind the dispersity in size expected for the equivalent particles that represent the hard phase concentrations in this model, this derived particle dimension is sensibly consistent with the 10.4 nm periodic repeat of the undeformed diffraction halo.

Implications of Affine Model

This analytical approach implies that the hard phase in this particular specimen tends to concentrate into regions that can be approximated to particles and that during the first part of deformation these effective particles separate from each other in an affine manner. Since the phase separation is expected to be initiated via a spinodal decomposition there is expected to be a degree of interconnectivity in the final ripened morphology. The analysis implies that any such connections do not significantly impair the movement of the main hard phase concentration during the initial deformation. It is of interest to note that the additional insight into the nature and size of the hard phase concentrations which is provided by this approach is obtained independently of a direct analysis of the SAXS pattern of the undeformed sample.

It should be noted that there is considerable variation in the formulation of thermoplastic polyurethanes and that other specimens have been observed in which the development of the SAXS patterns differs from the present example and where the above affine deformation approach would therefore not be applicable.

References

- [1] Ryan, A.J., Willkomm, W.R., Bergstrom, T.B., Macosko, C.W., Koberstein, J.T., Yu, C.C. and Russell, T.P., *Macromolecules* (1991) 24, 2883.
- [2] Elwell, M.J., Mortimer, S. and Ryan, A.J., *Macromolecules* (1994) 27, 5428.
- [3] Ryan, A.J., Macosko, C.W. and Bras, W., *Macromolecules* (1992) 25, 6277.
- [4] Mahendrasingam, A., Fuller, W., Forsyth, V.T., Oldman, R.J., Mackerron, D.H. and Blundell, D.J., *Rev. Scientific Instruments* (1992) 63, 1087.
- [5] Guinier, A., X-ray Diffraction in Crystals, *Imperfect Crystals and Amorphous Bodies*, (W.H.Freeman, San Francisco, 1963)

Structure determination from screw-disordered fibres

R. P. Millane* and J. L. Eads

Whistler Center for Carbohydrate Research and Computational Science and Engineering Program, Purdue University, West Lafayette, Indiana 47907-1160 USA

* Current address: Department of Electrical and Computer Engineering, University of Canterbury, Christchurch, New Zealand

Received 14th March 2002; accepted 16th April 2002.

Fibre diffraction analysis has traditionally used x-ray data from either noncrystalline or polycrystalline fibres. In some cases however, only data from specimens with intermediate ordering are available. A simple method for incorporating the effects of screw-disorder into structure determination, using a conventional refinement program, is described. The method is applied to diffraction data from a screw-disordered polynucleotide fibre.

Introduction

The degree of order in oriented specimens used for x-ray fibre diffraction analysis varies greatly. In a noncrystalline fibre, the diffracting particles are randomly rotated about the axis of orientation, and the diffraction pattern shows continuous intensity on layer lines. In a polycrystalline fibre, the molecules form small, well-ordered crystallites that are randomly rotated, and the diffraction pattern consists of discrete Bragg reflections. It is therefore straightforward to calculate the intensity diffracted by models of noncrystalline and polycrystalline fibre specimens, and for this reason, almost all polymer structures so far determined by x-ray fibre diffraction analysis have utilized one of these two kinds of specimen [1,2].

It is not uncommon, however, for fibres to give diffraction patterns that display both sharp reflections and continuous intensity on layer lines [3-6], indicating that the packing of the molecules is neither ideally noncrystalline nor ideally polycrystalline. In fact, a spectrum of such disordered fibres has been observed [3,4]. The Bragg reflections are often confined to the centre of the diffraction pattern, giving way to continuous intensities at high resolution, indicating that the packing of the molecules in the crystallites is disordered in some way. The diffraction pattern recorded from such a specimen depends not only on the molecular and crystal structures, but also on the

type and degree of disorder in the specimen. If the disorder is *uncorrelated*, then the diffraction can be separated into the sum of continuous and Bragg components. These components have the same general character as those from noncrystalline and polycrystalline specimens, but are different in detail.

Disordered fibres have generally not been used for structure determination because of the difficulty of calculating the diffraction from such specimens and of refinement. In cases where they have, an approximate method has been used in which molecular and crystal structures are co-refined against the continuous and Bragg diffraction, treating the continuous intensity data as if they are from a noncrystalline fibre, and the low resolution Bragg data as if they are from an ideal polycrystalline fibre [7,8]. Such an analysis is only approximately valid however, since it ignores the effects of the disorder on the diffracted intensities. Stroud and Millane [5,6] have recently reported a comprehensive analysis of diffraction by fibres that contain various kinds of packing disorder, and use of this theory allows the possibility of determining structures from these kinds of specimens while rigorously incorporating the effects of the disorder. We describe here a method for implementing such an approach and its application to diffraction data from a screw-disordered polynucleotide fibre.

There are two reasons for pursuing structural analysis of molecules in disordered fibres. First, some biopolymers pack only as disordered fibres, so that this is the only route by which structural information can be obtained. Second, since the disorder produces an averaging of the effects of specific intermolecular interactions (that are present in a polycrystalline fibre), structures in disordered fibres are more likely to represent intrinsic molecular structures free of these intermolecular effects.

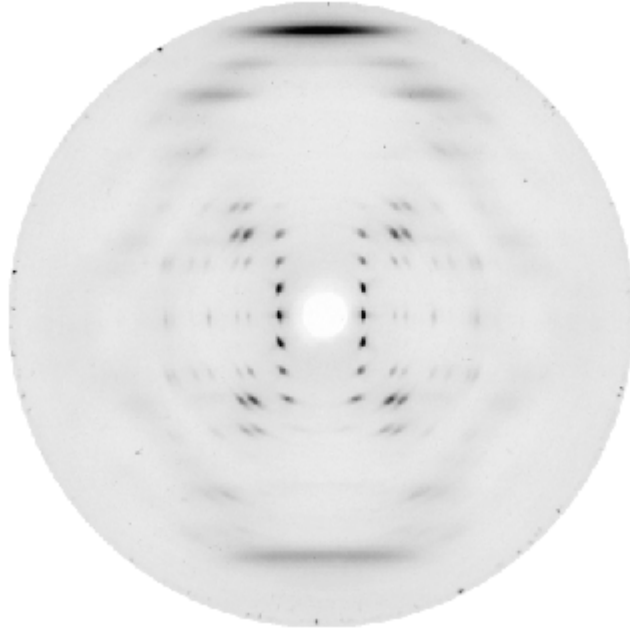


Figure 1: Fiber diffraction pattern from a-poly(dA)·poly(dT) (from Ref. 11)

Diffract by fibres

The intensity diffracted by a noncrystalline fibre at cylindrical polar radius R on layer line l is given by

$$I_l(R) = \sum_n |G_{nl}(R)|^2 \quad (1)$$

where the $G_{nl}(R)$ are the Fourier-Bessel structure factors and the sum is over the integers that satisfy the helix selection rule. In structure determination from such a specimen, molecular models are refined against the data $I_l(R)$. For a polycrystalline fibre, assuming a monoclinic unit cell with c parallel to the rotation axis, the intensity of the i -th spot on the l -th layer line, I_{il} , is given by

$$I_{il} = \sum_{(h_i, k_i)} |F_{h_i k_i l}|^2 \quad (2)$$

where the F_{hkl} are the usual crystallographic structure factors, and the sum is over the reciprocal lattice points $(h_i k_i l)$ that overlap in the spot (i, l) . The structure factors can be calculated in the usual way, or in terms of the Fourier-Bessel structure factors as

$$I_{il} = \sum_{(h_i, k_i)} \left| \sum_n G_{nl}(R) \exp(in(\psi_{h_i k_i} + \pi/2)) \right|^2 \quad (3)$$

where $(R_i, \psi_{h_i k_i}, l/c)$ are the cylindrical polar coordinates of the reciprocal lattice point $(h_i k_i l)$. In structure determination from such specimens, molecular and crystal structures are refined against the data I_{il} .

The packing disorder in the microcrystallites of disordered polycrystalline fibres is conveniently described in terms of *lattice* disorder and *substitution* disorder [5]. Lattice disorder is due only to deviations in the positions of the molecules away from their positions on a regular undistorted lattice. Substitution disorder is due to variations in the orientation of the molecule (or in the kind of molecule) at each site. If the lattice and substitution disorders are independent, and the distortions at different lattice points are uncorrelated, then the diffraction can be separated into the sum of continuous and Bragg components [5]. If the Cartesian components of the lattice disorder are independent, and the x and y components have equal variances, then general expressions have been derived for the continuous and Bragg diffraction in terms of the statistics of the disorder [5].

We consider here the case of screw disorder (a form of substitution disorder) that is quite common with molecules of high helix symmetry (such as polynucleotides). Screw disorder occurs when the helical molecules in a crystallite randomly "screw in and out" of a plane normal to the rotation axis, as a result of rigid body motion constrained by the interlocking of grooves and protuberances of neighbouring molecules. If the screw disorder is completely random, its symmetry is the same as the molecular helix symmetry (as would usually be expected), and the molecular helix is integral (one helix turn in one c -repeat), then the continuous and Bragg components of the diffraction are given by [4,5]

$$I_l^{(sd)}(R) = \sum_n |G_{nl}(R)|^2 - |G_{ll}(R)|^2 w_{lattice}(R, l/c) \quad (4)$$

and

$$I_{il}^{(sd)} = N_{il} |G_{ll}(R)|^2 w_{lattice}(R, l/c) \quad (5)$$

The *lattice disorder weight* $w_{lattice}(R, Z)$ is given by

$$_{ice}(R, Z) = \exp(-4\pi^2(R^2\sigma_{lat}^2 + Z^2\sigma_{axial}^2)) \quad (6)$$

where σ_{lat}^2 and σ_{axial}^2 are the variances of the distortions of the lattice sites normal (or "lateral") and parallel (or "axial") to the direction of orientation, respectively, N_{il} is the number of overlapping reflections in spot (i, l) , and the superscript (sd) denotes "screw-disordered." (Note that the term $Z^2\sigma_{axial}^2$ is missing in equations (75) and (76) of Ref. 5).

Structure determination incorporating the effects of disorder

Structure determination using data from disordered fibres in general requires optimisation of molecular and disorder parameters to obtain the best match between the calculated and measured diffraction. For the case of screw disorder however, the simplicity of the expressions (4) and (5) allows a simple refinement protocol to be developed based on use of a conventional fibre refinement program such as LALS [9], that rigorously incorporates the effects of the disorder. This is the approach we have taken. In many cases, most of the available data (and all the high resolution data) are continuous, and the

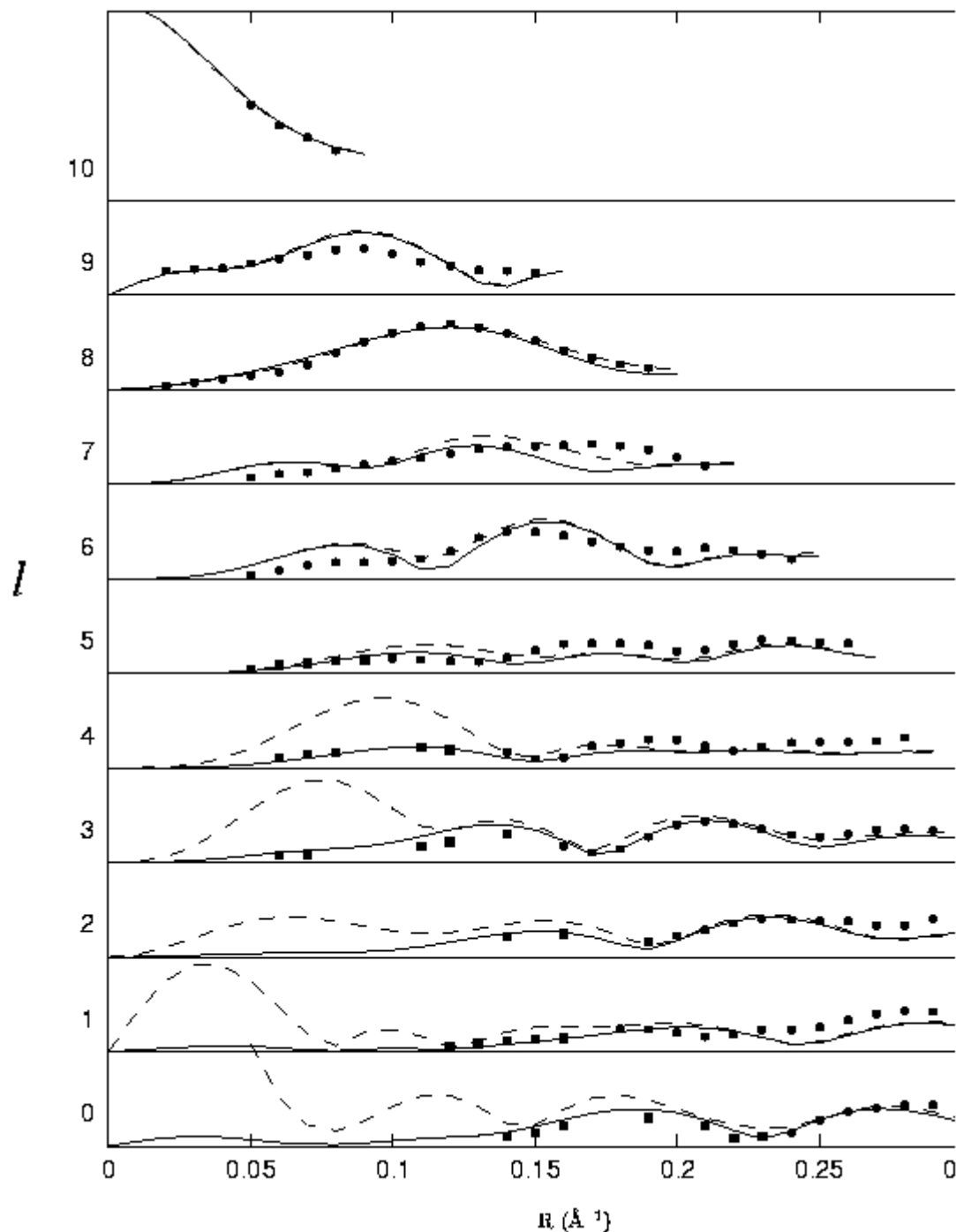


Figure 2: Observed x-ray amplitudes in the resolution range $\sim 6\text{-}3\text{\AA}$ (circles), and in the resolution range $\sim 8\text{-}6\text{\AA}$ (squares). Amplitudes calculated from refined models based on screw-disordered (---) and noncrystalline (- - -) fibres.

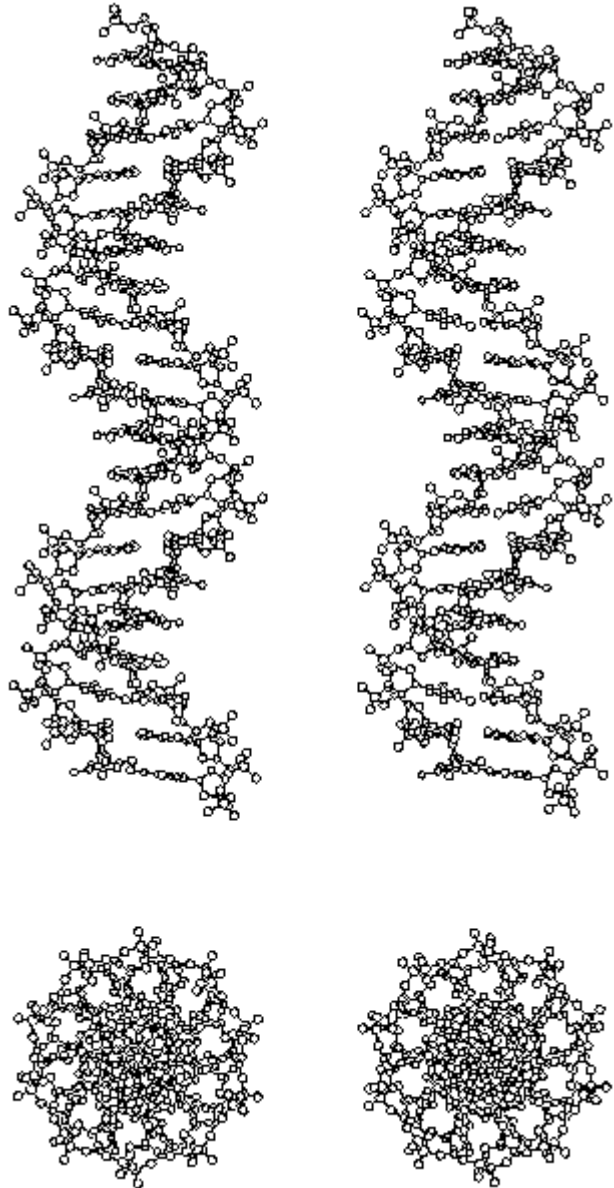


Figure 3: Structures of a-poly(dA)-poly(dT) viewed normal and parallel to the helix axis, determined as described here incorporating the effects of the screw disorder (left), and as determined in Ref. 8 (right).

refinement scheme we describe is based on using the continuous data. The approach is to iteratively modify the data to "take out" the effect of the disorder, allowing refinement based on a noncrystalline fibre. This is done as follows.

1. Obtain an initial estimate of the structure using conventional methods based on the continuous data and assuming a noncrystalline specimen.
2. Select values of σ_{lat} and σ_{axial} .
3. Using the current estimate of the molecular structure, calculate the continuous diffracted amplitudes $|I_l(R)|^{1/2}$ and $|G_{ll}(R)|$.
4. Compute a modified data set, denoted by $[\hat{I}_l^{obs}(R)]^{1/2}$, as

$$\hat{I}_l^{obs}(R) = I_l^{obs}(R) + K^2 |G_{ll}(R)|^2 w_{lattice}(R, l/c),$$

where $I_l^{obs}(R)$ is the continuous observed intensity data and K is the scale factor (i.e. $|I_l^{obs}(R)|^{1/2}$ is scaled to $K|I_l^{calc}(R)|^{1/2}$). The modified data $[\hat{I}_l^{obs}(R)]^{1/2}$ represents the continuous data that would be observed if the specimen were perfectly noncrystalline, based on the current estimate of the molecular structure.

5. Refine the molecular structure against $[\hat{I}_l^{obs}(R)]^{1/2}$, treating it as if the specimen were noncrystalline.
6. If step 5 results in no significant change in the x-ray agreement then stop, otherwise return to step 3.

The procedure is repeated for a set of values of σ_{lat} and σ_{axial} to find those that give the best agreement. A model consistent with the continuous x-ray data and incorporating the effect of the disorder is then obtained.

Application to α -poly(dA)·poly(dT)

The polynucleotide duplex poly(dA)·poly(dT) has been trapped in both polycrystalline and screw-disordered fibres. Structure determination based on x-ray data from these different allomorphs shows conservation of the overall molecular morphology, and this system therefore provides an ideal test-bed for the method described above.

Poly(dA)·poly(dT) has been trapped in three distinct forms in oriented fibres. Two of these are polycrystalline, one with one molecule per unit cell (the β_1 -form) [10], and the other with two molecules per unit cell (the β_2 -form) [11,12]. Structure determination for the two β forms shows that the overall molecular structures are quite similar in the two allomorphs [10,12]. The two strands of the double helix are similar, but are different enough conformationally to give a duplex morphology distinct from that of classical B-DNA. The third form of poly(dA)·poly(dT), denoted the α -form [11], gives a diffraction pattern that contains sharp Bragg reflections at low resolution, that give way to continuous diffraction at higher resolution (Figure 1). Park *et al.* [8] analysed the structure of α -poly(dA)·poly(dT) using the continuous x-ray data between approximately 6 and 3 Å resolution, and the low resolution Bragg data. In this analysis, it was assumed that the continuous diffraction at a resolution greater than ~6 Å is due to a perfectly noncrystalline specimen, and that the sharp Bragg reflections at a resolution of less than ~6 Å are due to a perfectly polycrystalline specimen. This approach was based on the reasonable assumption that the Bessel term $G_{ll}(R)$ which is eliminated by the screw disorder (in the absence of lattice disorder) would have a relatively small amplitude at resolutions greater than 6 Å, so that its inclusion in the calculation would introduce only a small error. However, such an approach does involve an approximation, and it also imposes the restriction of having to exclude data with spacings > 6 Å. We therefore applied the algorithm described above to the continuous diffraction data from α -

poly(dA)·poly(dT).

A survey of different disorder models for α -poly(dA)·poly(dT) by Stroud & Millane [13] confirmed that the diffraction data are best explained by a specimen in which the molecules in the crystallites are randomly screw disordered, and also indicated that the lattice is subject to small lateral and axial distortions. Referring to (4), and considering the behaviour of the Bessel functions and the function $w(R,Z)$, the disorder is expected to affect the diffraction primarily at medium resolution. We therefore conducted two sets of refinements, one using the original diffraction data in the resolution range 6-3 Å, and one using data in the region 8-3 Å. The medium (8-6 Å) resolution continuous data were measured only where there was no interference by Bragg sampling. The structure was refined conventionally against the continuous data using each data set. It was also refined, incorporating the effects of the disorder, by using the algorithm described above, for a range of values of σ_{lat} and σ_{axial} , and using both data sets. The algorithm converged within four cycles in all cases, and the best agreement was obtained for $\sigma_{lat} \approx \sigma_{axial} \approx 0.2$ Å. The results of the refinements are listed in Table 1. Referring to the table shows that for the case of data in the range 6-3 Å, although the x-ray agreement is slightly better for the refinement based on the screw-disordered model than for that based on the noncrystalline model, the differences are quite small. This is not particularly surprising, and validates the approach taken by Park *et al.* [8], showing that the particular x-ray data they used are indeed relatively insensitive to the disorder as described above. However, the approach is not completely satisfactory since it does not allow one to make use of all the available diffraction data, and in the presence of lattice disorder the term $|G_{ll}(R)|$ does contribute to the continuous diffracted intensity. The results obtained using data in the range 8-3 Å show why Park *et al.* [8] had to use the restricted data set. Significantly better agreement is obtained for a refinement based on a screw-disordered specimen than for one based on a noncrystalline specimen (Table 1). With the new algorithm, very good agreement ($R'' = 0.23$) is obtained with many more diffraction data (182 vs. 152) and addition of only one parameter. (We set $\sigma_{lat} = \sigma_{axial}$ since releasing this constraint did not lead to significantly better agreement). As expected, a poor fit with the larger x-ray data set is obtained ($R'' = 0.39$) if the effect of the

Resolution range of data (Å)	Screw disordered	R	R"
6 - 3	N	0.25	0.28
6 - 3	Y	0.22	0.26
8 - 3	N	0.32	0.39
8 - 3	Y	0.20	0.23

Table 1: Conventional (R) and quadratic (R") crystallographic R-factors for the continuous diffraction for various models as described in the text

disorder is not incorporated. The agreement between the measured and calculated amplitudes is shown in Figure 2. The fit of the final model to the Bragg data was assessed by refining only the scale factor while fitting $[I_{il}^{(sd)}]^{1/2}$ to the Bragg data $[I_{il}^{obs}]^{1/2}$. This gave $R = 0.21$ and $R'' = 0.23$ for the Bragg data. The backbone conformation angles of the structure obtained are similar to those of the previously determined a structure, and the β_1 and β_2 structures. Differences between the α structures are generally no larger than the differences amongst the original α structure and the β structures. This is can be seen by comparison of the molecular structure obtained here with that of Ref. 8 (Figure 3).

Discussion

Polymer and other biomolecular structures so far determined by x-ray fibre diffraction analysis have almost always utilized diffraction data from either noncrystalline or polycrystalline specimens. In the few cases where data from specimens with intermediate ordering have been used, the disorder has been only approximately taken into account. Explicit treatment of the effects of the disorder allows use of the full set of available diffraction data, and leads to a more rigorous, accurate and satisfactory structure determination. Application of the method described here for the case of screw-disorder leads to a structure that is within the conformational domain defined by the other crystal forms and gives good x-ray agreement against a larger data set. This lends support to the validity of the approach. For this particular example, the advantages of this approach are relatively small, since the increase in the number of data that it allows is rather modest. However, this will not always be the case. In cases where the disorder affects most, or all, of the diffraction data, using an approach of this kind will be necessary for accurate structure determination.

We are grateful to Drs. R. Chandrasekaran and Struther Arnott for discussion, and the U.S. National Science Foundation for support (DBI-9722862).

References

- [1] Millane, R.P., in *Crystallographic Computing 4: Techniques and New Technologies* (eds. Isaacs, N.W. & Taylor, M.R.), Oxford, London, 1987, pp. 169-186.
- [2] Millane, R.P., in *International Tables for Crystallography, Vol. B* (ed. Schmueli, U.), Kluwer, Dordrecht, 2001, pp. 466-481.
- [3] Miller, A. & Parry, D.A.D., *Polymer* (1974) 15, 706-712.
- [4] Arnott, S., in *Fiber Diffraction Methods* (eds. French, A.D. & Gardner, K.H.), American Chemical Society, Washington, DC, 1980, pp. 1-30.
- [5] Stroud, W.J. & Millane, R.P., *Acta Cryst.* (1995) A51, 771-790.
- [6] Millane, R.P. & Stroud, W.J., *Fiber Diffraction Rev.* (1996) 5, 16-20.
- [7] Arnott, S., Chandrasekaran, R., Millane, R.P. & Park, H.S., *J. Mol. Biol.* (1986) 188, 631-640.
- [8] Park, H.S., Arnott, S., Chandrasekaran, R. & Millane, R.P., *J. Mol. Biol.* (1987) 197, 513-523.
- [9] Smith, P.J.C. & Arnott, S., *Acta Cryst.* (1978) A34, 3-11.
- [10] Chandrasekaran, R., Radha, A. & Park, H.S., *Acta Cryst.* (1995) D51, 1025-1035.
- [11] Arnott, S. & Selsing, E., *J. Mol. Biol.* (1974) 88, 509-521.
- [12] Chandrasekaran, R. & Radha, A., *J. Biomol. Struct. Dynam.* (1992) 10, 153-168.
- [13] Stroud, W.J. & Millane, R.P., *Acta Cryst.* (1995) A51, 790-800.

10th Annual Workshop Prize-Winning Posters

Evidence of spinodal decomposition in semi-crystalline polymers

E.L.Heeley^a, W.Bras^b, I.P. Dolbnya^b, A. Maidens^c, P.D.Olmsted^c

J.P.A. Fairclough^a & A.J. Ryan^a.

^a Chemistry Department, University of Sheffield, Brook Hill, Sheffield, S3 7HF, UK.

^b ESRF, BP220, F-38043, Grenoble Cedex, France.

^c IRC, Physics Department, University of Leeds, Leeds, LS2 9JT, UK.

Received 14th January 2002; accepted 14th March, 2002.

Introduction

Polymer processing relies on the shaping of molten polymer in dies and moulds. During processing, the crystallinity of the material will develop and stabilize the shape of the final product, as well as determining the aesthetic and mechanical properties. Inevitably, the prediction and control of the crystallization of a polymer during its processing will enable new 'application specific' materials to be developed. Clearly, today, the polymer processing industry is concerned with such developments of new and useful materials, due to the high demand for these products in our everyday lives.

The complete processing of a polymer into a product, involves the development of a molecular hierarchical ordered structure (the crystallization process). Here, from the polymer melt, crystallites form and grow into lamellar (crystalline and amorphous regions) which, in turn, are organized into large spherulitic superstructures. The growth of lamellae crystals into the final spherulitic macrostructure is well understood and the theories predicting the crystallization kinetics are usable and well developed [1,2]. However, one area that is less understood in the crystallization process is the 'early' or 'pre-nucleation' stage. Revealing the initial step of polymer crystallization will give a fuller picture of the complete process and provide invaluable information into refining and controlling the final physical properties of the material.

The classical picture of polymer crystallization involves, firstly, the creation of a stable nucleus from

the entangled polymer melt and, secondly, the growth of the crystalline region into the lamellar structures and beyond. In the past, the kinetics involved with the formation of a stable nucleus have been difficult to follow experimentally, thus few theories were developed which describe this process well. Recently, however, investigations into the early stages of polymer crystallization X-ray scattering techniques have allowed theories to be developed which describe the process in terms of a 'liquid-liquid' phase separation system[3]. The early stages of the crystallization are thought to follow an ordering of the molecules through a mesophase, which continues to evolve through a process of phase separation into crystalline and amorphous regions. The development of a mesophase in the phase separation process can be described theoretically with the kinetics of spinodal decomposition[4]. Here, a continuous transformation of a partially ordered phase (polymer chains with the correct conformation) develops towards more ordered states leading to nucleation of crystallites and growth. Molecular chains without the correct conformation will become the amorphous phase components. Figure 1, shows how the phase separation leads from the random coil of a polymer melt to a crystalline lamellar structure.

Following the early stages of crystallization kinetics has been successfully reported recently on a range of semi-crystalline polymer samples such as polyethylene terephthalate (PET)[5], isotactic polypropylene (iPP), polyethylene (PE)[6] and polyether ketone ketone (PEKK)[7]. These investigations have also observed spinodal-like

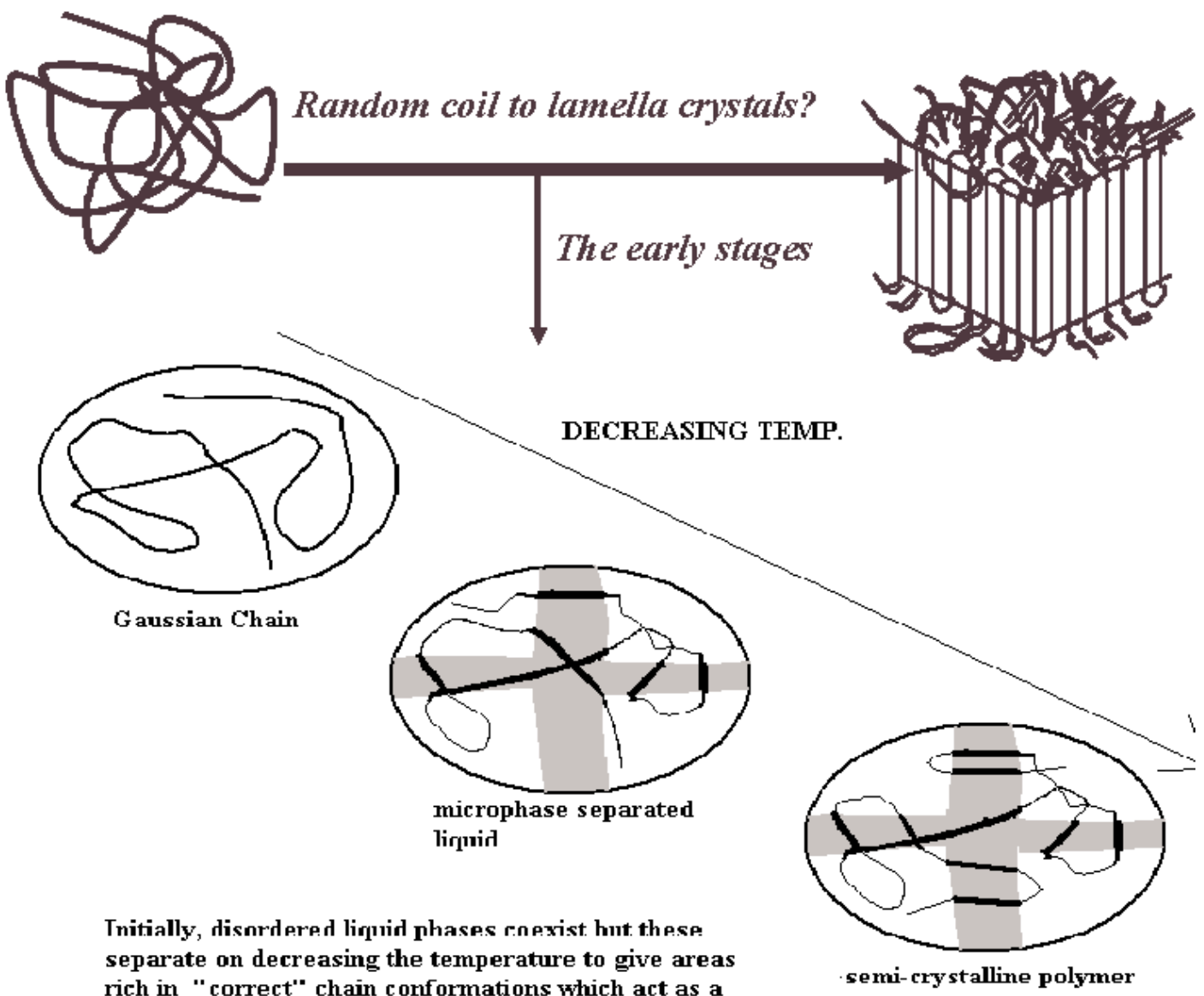


Figure 1: Phase separation during the early stages of polymer crystallization.

kinetics during the early stages of crystallization. Further investigations into the crystallization of commercial iPP samples have been performed here, using time resolved Small- and Wide- Angle X-ray Scattering experiments. Particular attention has been paid to the early stages of crystallization and relating this to the spinodal decomposition kinetics described.

From the scattering data obtained during crystallization, SAXS develops showing long range ordering (stacking of lamellae) or the macrostructure, along with WAXS giving details on the atomic unit cell or microstructure development. If the kinetics follow classical nucleation and growth theories then the SAXS and WAXS should develop together after an induction period, t_i . However, if the SAXS is seen to emerge before any WAXS is detected during this induction period, then the

development of some long-range ordering must be occurring before any crystalline structure arises. This is identified as the spinodal region during the pre-nucleation stages of crystallization. As the SAXS intensity grows in this period, the kinetics of the crystallization can be fitted to the Cahn-Hilliard (CH) linearized growth model [8,9] for spinodal decomposition. This describes the time evolution of the scattering intensity following an exponential growth from the increased amplification of density fluctuations. The fitting of the CH theory to the SAXS data gives an extrapolated value for the spinodal temperature. Below this temperature the polymer is said to spontaneously separate into two phases.

Previous experimental evidence of spinodal decomposition in iPP and other semi-crystalline polymers has been reported in Ryan *et al.* 1999 [10].

Here the spinodal temperatures have been obtained from the CH analysis of SAXS data obtained from the Daresbury SRS. However, recent arguments have questioned this 'phase separation' route to early structure development indicating that scattering observed in the SAXS pattern before WAXS is a feature relating to detector sensitivity [11]. This is, in fact, a valid argument and depends upon the WAXS detector limitations, whether being 'counting rate' or 'intrinsic experimental' limitations. Detector count rates can vary depending on type, but statistical limitations occur when the sum of detected scattered photons is dependant primarily on the scattering process (i.e. lowest detectable crystalline limit).

Recently, improved detector technology has been developed to greatly reduce limitations on 'count rates', allowing improved data collection which can be used in comparison with previous data and so address the issue of WAXS detection capabilities. Details of the early stages of the quiescent crystallization of iPP using time-resolved SAXS/WAXS/DSC experimental techniques, are given below. The data have been collected for comparative examination from both the ESRF Dubble beam line, France and the Daresbury SRS 8.2 beam line, UK using different WAXS detection systems.

Experimental

Samples of commercial iPP (S-30-S: M_w=520Kg/mol., M_w/M_n = 4.4 & Daplen: M_w= 622 Kg/mol, M_w/M_n= 5.5) free from additives, were used to investigate the early stages of quiescent crystallization at several temperatures. Samples were isothermally crystallized having been quenched from above the melting point to the desired temperature, using a Linkam DSC [12]. The SAXS /WAXS data were recorded simultaneously during the crystallization, where similar quadrant SAXS detectors were used [13], however the WAXS detectors differed. The WAXS detector used at the Daresbury SRS (Inel) [13] and the ESRF (MSGC) [14,15] are both photon counting devices and a comparison of their specifications is given in Table 1. The SAXS data from the experiments were analysed using the CH model and the spinodal temperature thus obtained.

Data analysis and results

During the crystallization of the iPP the

SAXS/WAXS data were recorded. Figure 2, gives the 1-D SAXS and WAXS data for the quiescent crystallization at 130°C obtained from Dubble at the ESRF. Figure 3 shows the integrated intensity, SAXS from the invariant and WAXS from the relative crystallinity. An Avrami plot is also given which illustrates the slope or the Avrami exponent, in this case the value being ~3 showing a spherulitic growth component [14]. From this figure it is clear that the evolution of SAXS and WAXS are simultaneous. However, Figure 4 gives the integrated intensity of a quiescent crystallization at 142°C. Here, it is clear that the SAXS starts to develop well before any WAXS is observed (a gap of ~10 minutes). During this period, the SAXS peak is seen to grow, indicating the development of long range order. The development of the 1-D SAXS pattern without accompanying WAXS, during the early stages of the crystallization at 142°C, is shown in Figure 5.

The theory of spinodal decomposition is used to describe these events prior to nucleation. The SAXS peak is therefore analysed in terms of the CH model. This predicts that the variation in the scattering intensity with time following a quench, is given by the following equation:

$$I(q,t) = I_0 e^{2R(q)t} \quad (1)$$

Being:

$$R(q) = D_{eff} q^2 \left[\frac{1-q^2}{2q_m^2} \right] \quad (2)$$

Where, I_0 is the initial scattering intensity, $R(q)$ is the growth rate at given q , D_{eff} is the effective diffusion coefficient and q_m the wave vector having the highest rate of growth.

The growth rate $R(q)$ is determined by plotting $\ln I$ vs t , for discrete wave vectors and obtaining the slope. From this the CH plots ($R(q)/q^2$ vs q^2) are performed and extrapolation of $q=0$ of the linear portion (between the limits $q_m < q < \sqrt{2}q_m$) of the plot gives D_{eff} . Figure 6 gives an example of the CH plot of the crystallization at 142°C during the spinodal region. The inset shows the scattering intensity at discrete values of q with time, where the linear slope gives

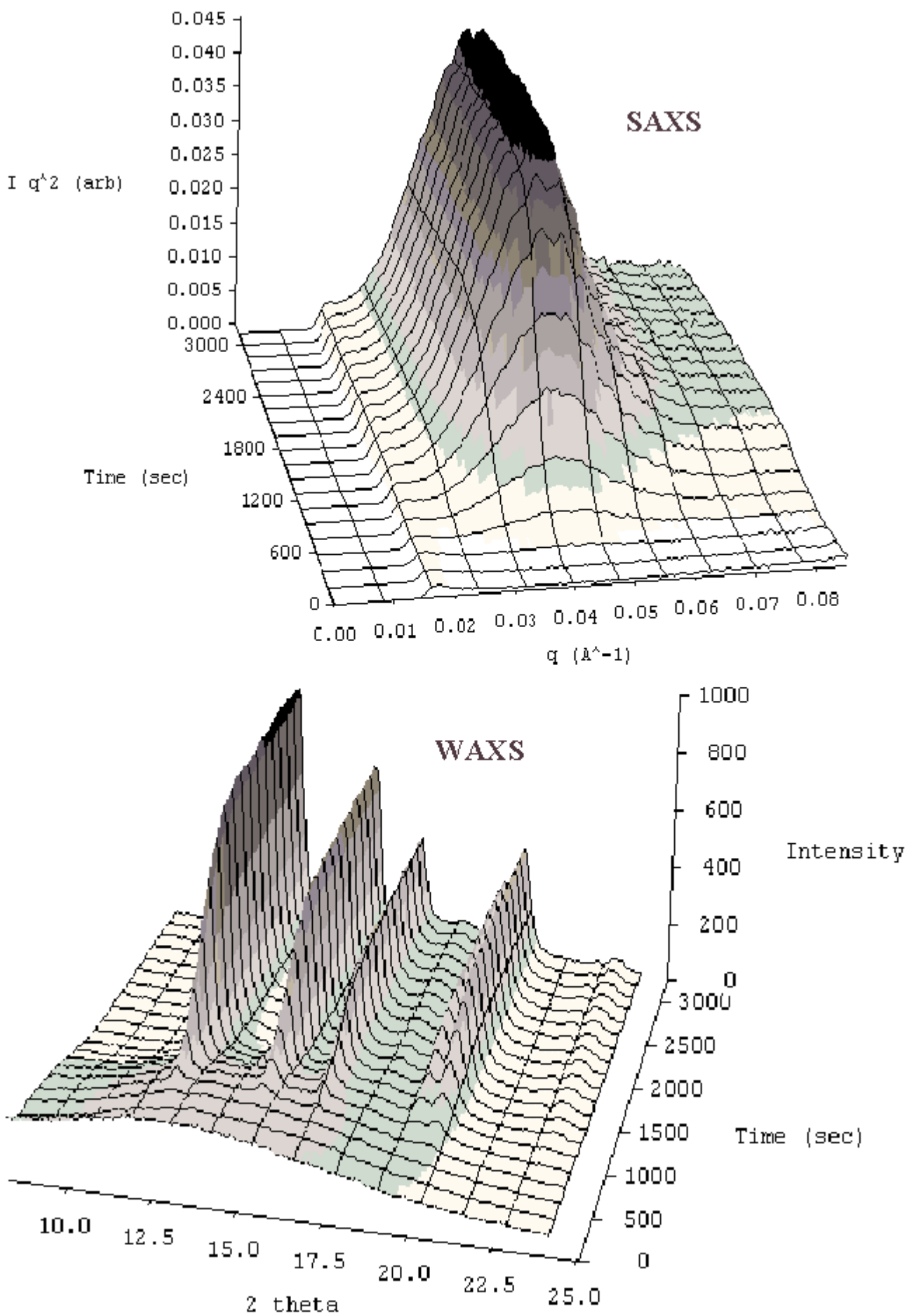


Figure 2: SAXS/WAXS development during quiescent crystallization of iPP at 130°C.

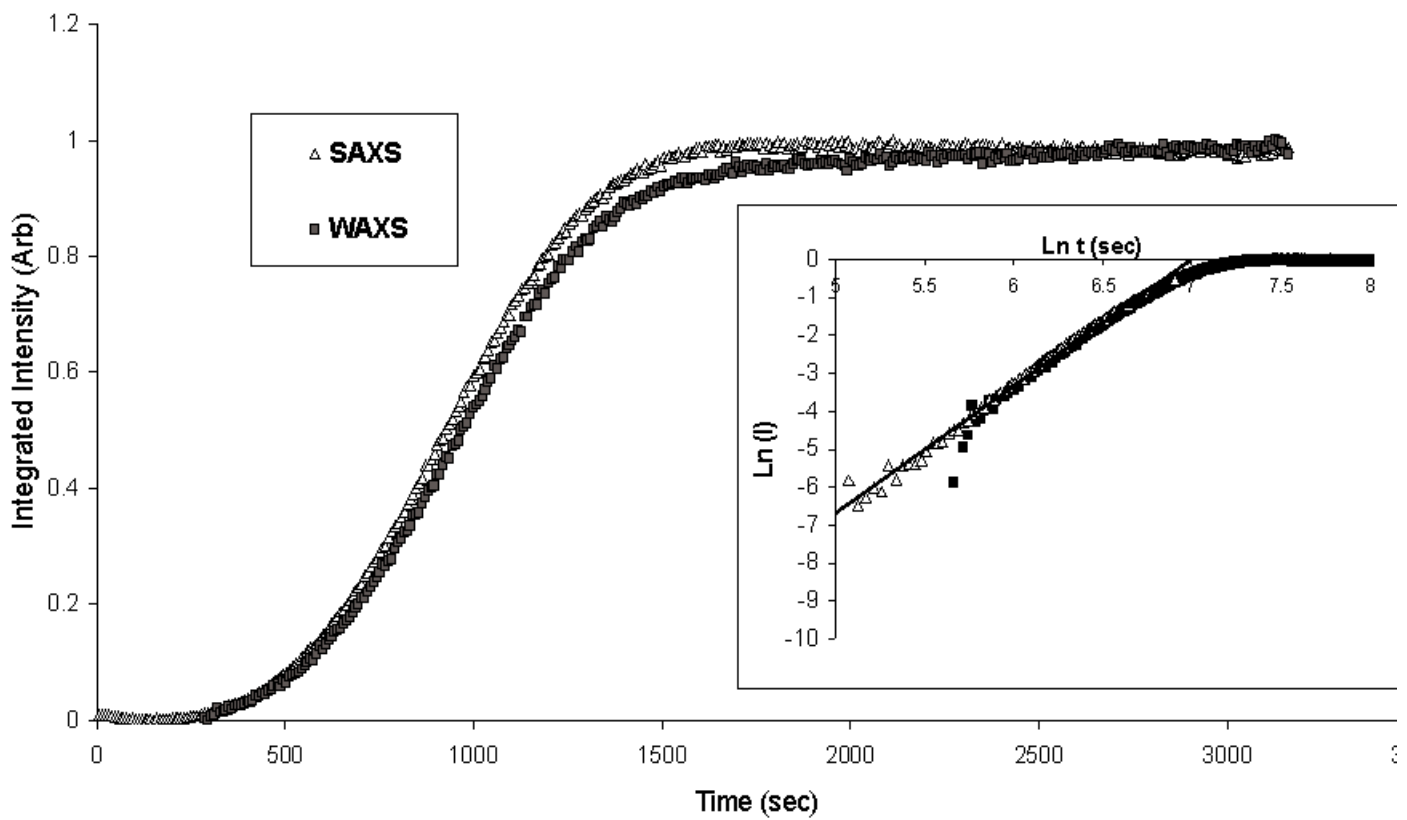


Figure 3: Integrated intensity data for quiescent crystallization of iPP at 130°C. Inset illustrates Avrami plot where the fit has a slope ~ 3 .

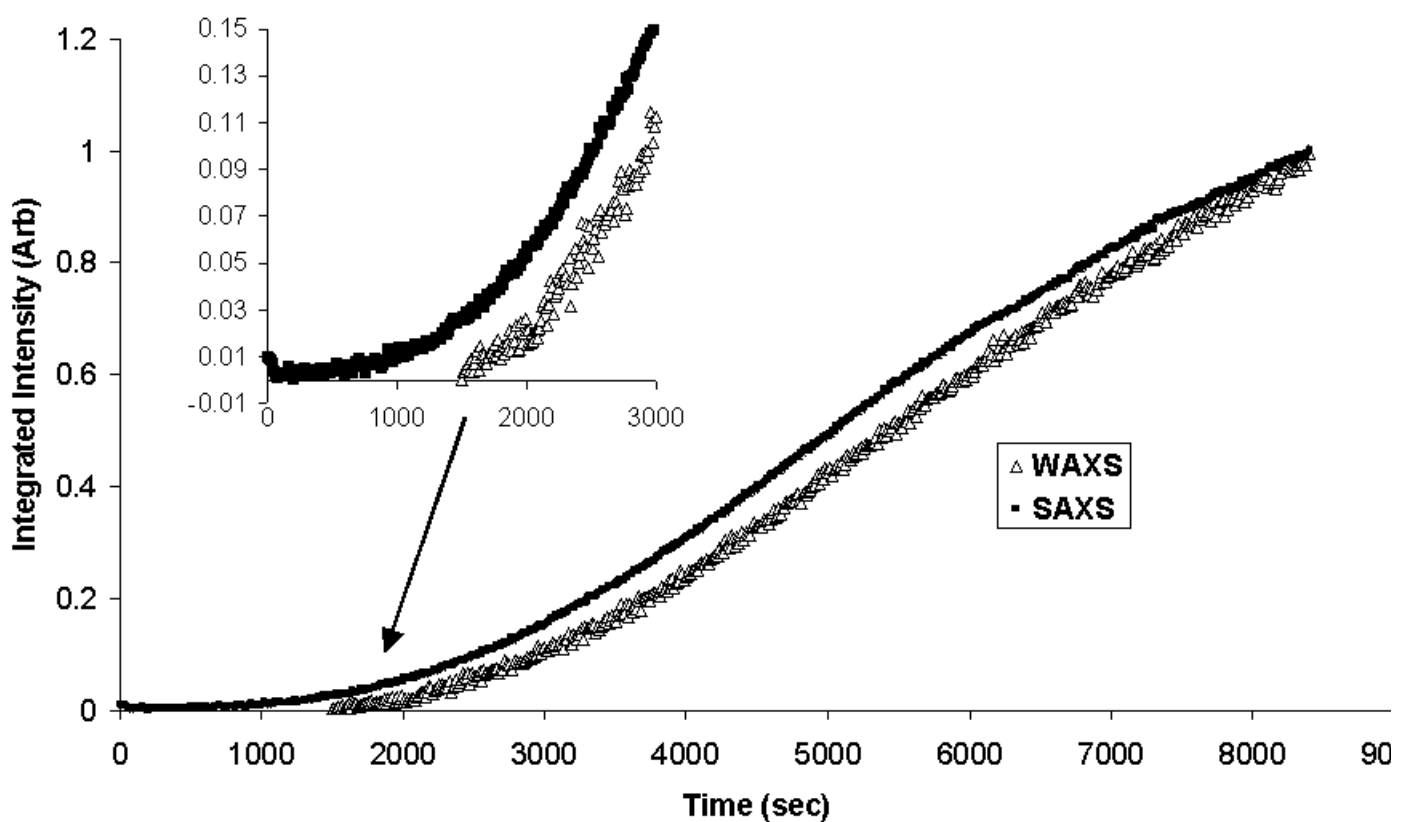


Figure 4: Integrated intensity of quiescent crystallization for iPP at 142°C. Inset shows development of SAXS before WAXS. Here, SAXS intensity is shown at $t = 0$ but, no WAXS peaks develop to integrate before 1500s.

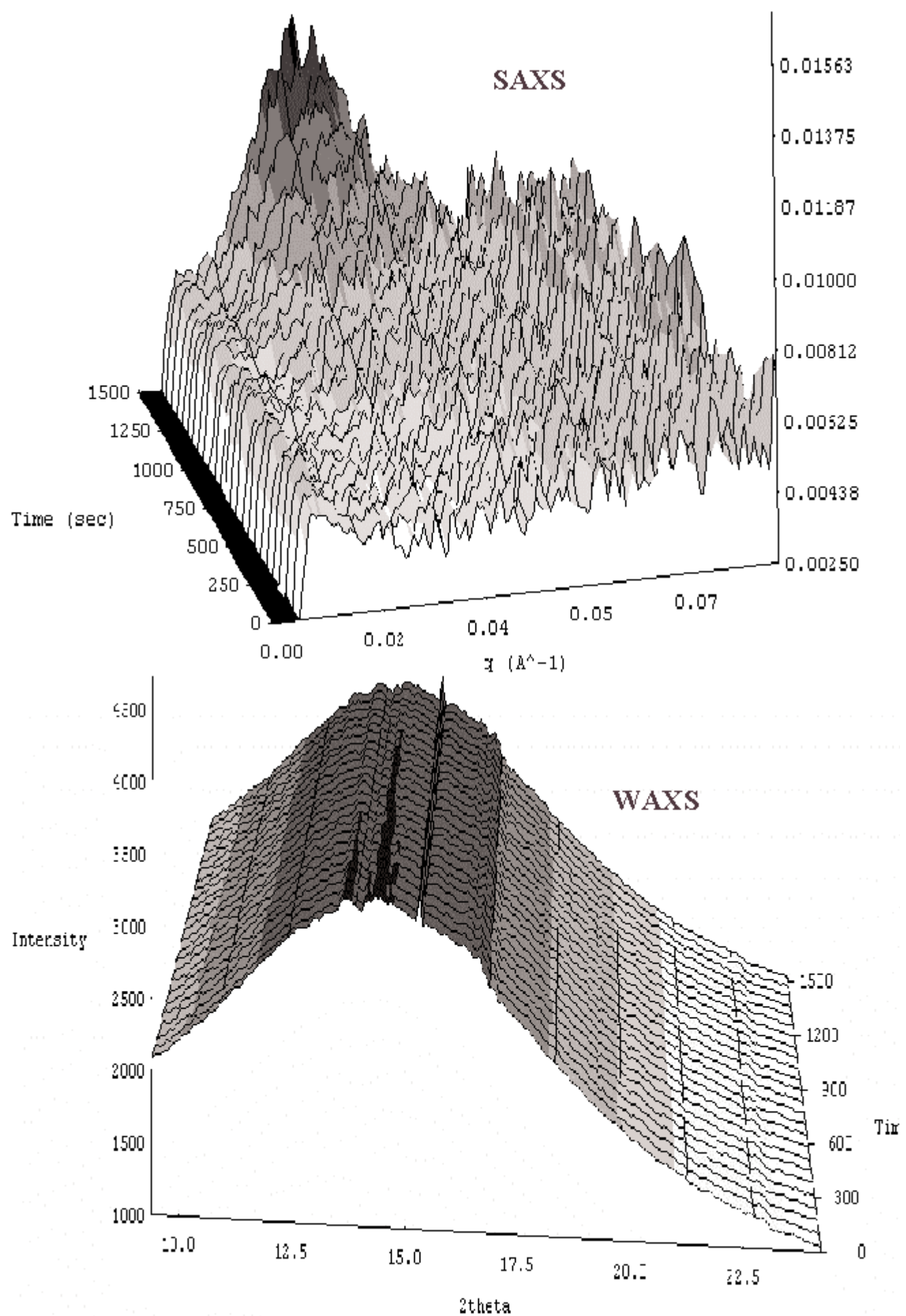


Figure 5: Development of SAXS peak before WAXS during the spinodal region.

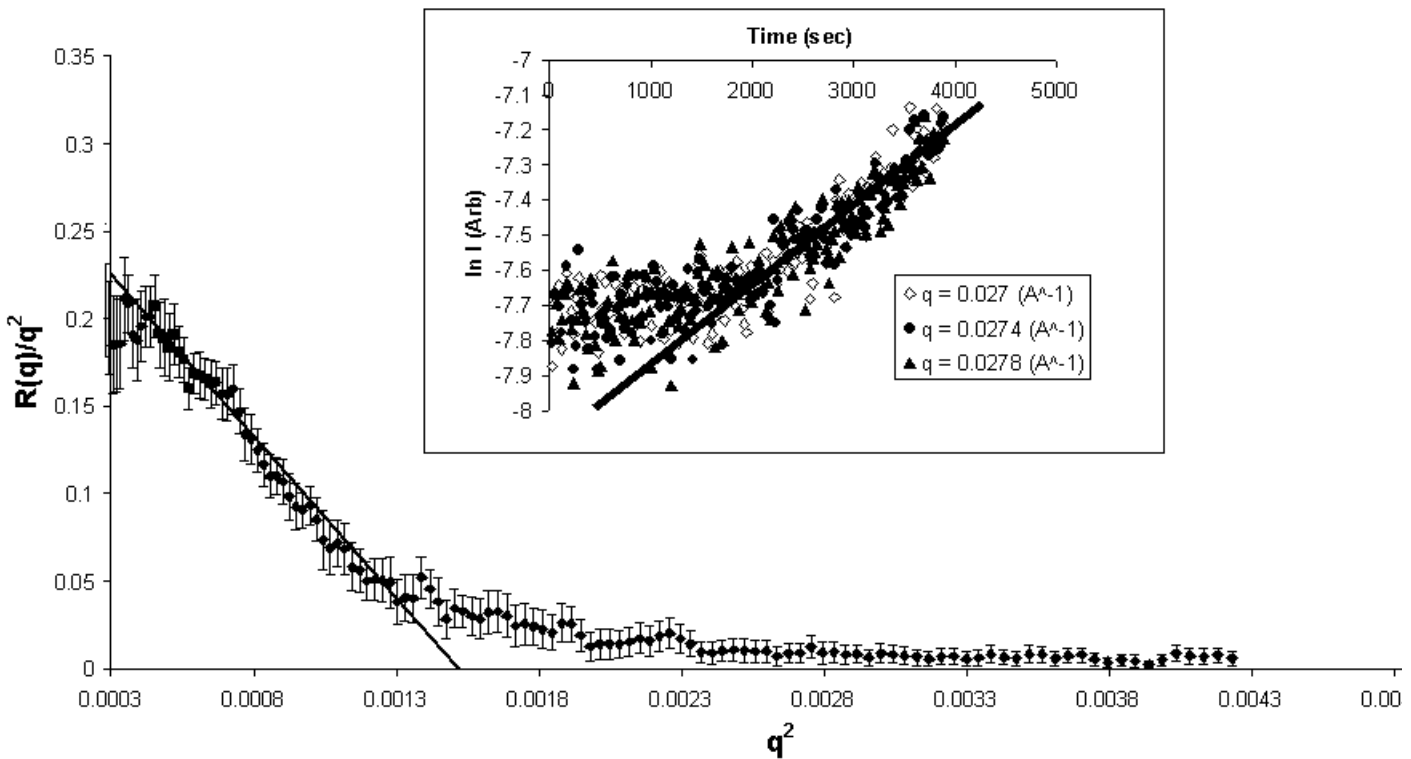


Figure 6: Cahn-Hilliard plot of quiescent crystallization of iPP at 142°C where the linear fit is used to estimate D_{eff} at $q=0$. The inset shows $\ln I$ v t plots for discrete values of q , here the linear fits are used to calculate $R(q)$.

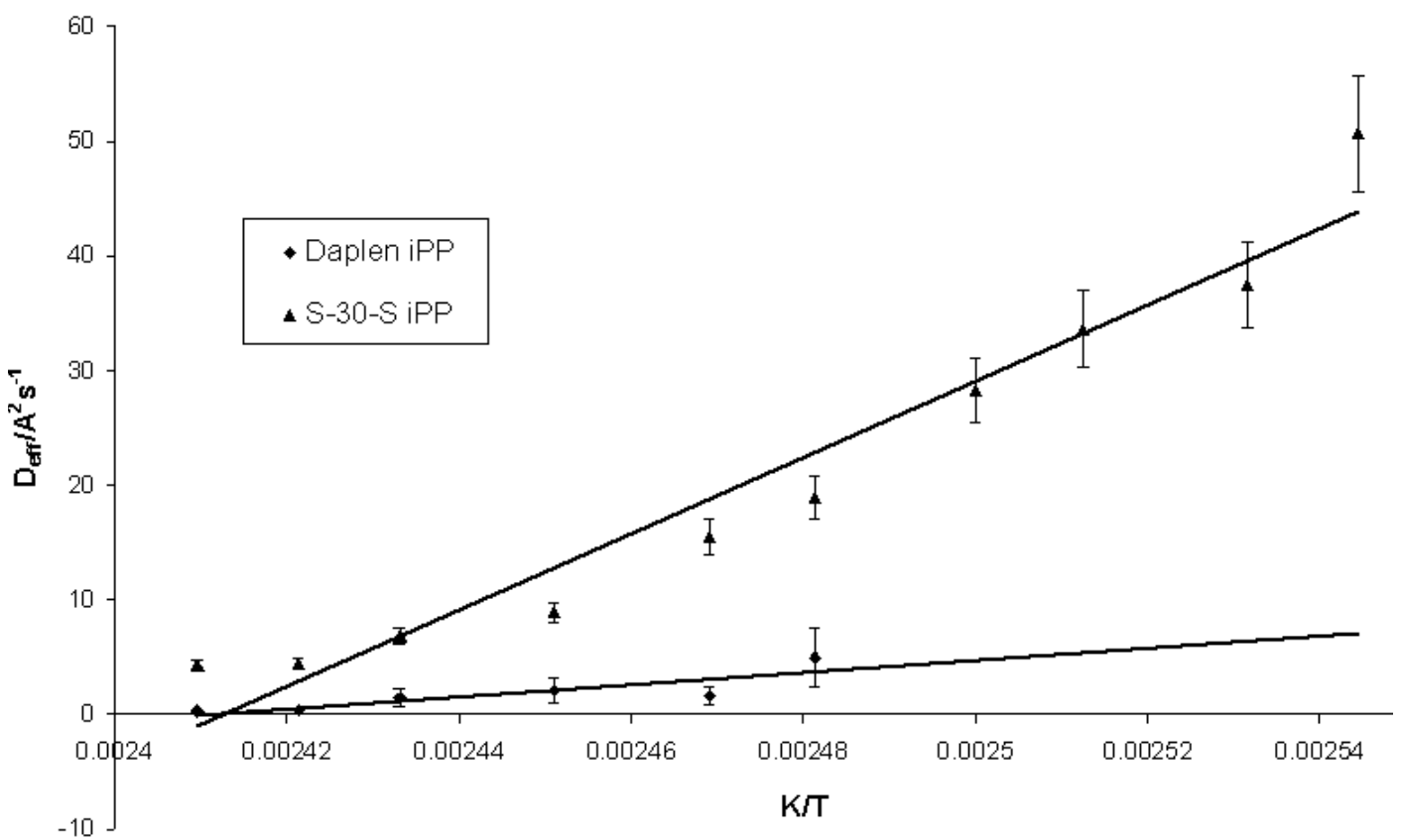


Figure 7: Graph of D_{eff} v $1/T$, allowing the calculation of the spinodal temperature from extrapolation to $D_{eff}=0$

the growth rate $R(q)$. The D_{eff} values at several quench temperatures were calculated in this way for the polypropylene sample in order to estimate the spinodal temperature T_s . Figure 7, shows a plot of the D_{eff} values with quench temperatures for the two similar iPP samples, S-30-S where the data were recorded at the Daresbury SRS (from Ryan *et al.* 1999) and Daplen having data recorded from the ESRF. Table 2 gives the spinodal temperature which is calculated from the extrapolation of $D_{eff} = 0$, along with the thermodynamic melting point T_{m0} [15] and measured DSC melting point T_m . From the table the T_s values of both iPP samples are estimated to be 415 K, which is 44 K below the thermodynamic melting point of a polypropylene crystal and ~23 K below the measured melting point. The final long spacing of the polypropylene from the SAXS is ~150 Å.

Discussion

Crystallizations with long induction times, i.e. shallow quench temperatures, show evidence of the onset of long scale ordering prior to crystal growth from simultaneous SAXS/WAXS experiments. It has been possible to analyse the data in terms of spinodal decomposition theory, where the events are described as a phase separation process and the amplitude of the density fluctuation increases with time, shown by the early emergence of a SAXS peak before WAXS. The SAXS data can be conveniently fitted to the Cahn-Hilliard model which gives rise to the spinodal temperature, below which the polymer spontaneously separated into two phases. From the data taken using similar iPP samples but using different WAXS detectors, some differences have been observed in the results with respect to the quench temperature. Generally, the gap between SAXS and WAXS is seen to agree with data obtained from both WAXS detectors at shallow quench depths. However, the gap is not observed at deep quench depths in the data obtained from the MSGC detector at the ESRF. This indicates that the improved signal to noise ratio in the MSGC detector allows the detection of crystallinity from the sample at lower levels than does the Inel detector.

In conclusion, agreement with T_s values has been observed with both systems, but obviously improvements in detector technology have led us to address the argument of detector sensitivity. It is possible now to see how the improvements made with the MSGC detector have enabled the issue of

spinodal decomposition as a precursor to nucleation to still be an obvious route to primary crystallization. However, experimentally, the phase separation is very much a temperature dependant process and even though we have seen that the technical detector limitations are reduced from the comparison of data here, there are still statistical limitations in the data analysis that cannot be totally disregarded.

References

- [1] Young, R.J. & Lovell, P.A., *Introduction to Polymers*, Chapman & Hall, London, 2nd ed, 1991.
- [2] Gedde, U.W. *Polymer Physics*, Chapman & Hall, London, 1st edition, 1995.
- [3] Olmsted, P.D., Poon, W.C.K., McLeish, T.C.B., Terrill, N.J. & Ryan, A.J., *Phys Rev Letters*, 1998, **81**, 373-376.
- [4] Bates, F. S. & Wiltzius, P., *J. Chem. Phys.*, 1989, **91**, 3258-3274.
- [5] Imai, M., Kaji, K. & Kanaya, T., *Macromols.*, 1994, **27**, 7103-7108.
- [6] Terrill, N. J., Fairclough, P. A., Towns-Andrews, E., Komanschek, B. U., Young, R. J., Ryan, A. J., *Polymer*, 1998, **39**, 2381.
- [7] Ezquerra, T.A., López-Cabarcos, E., Hsiao, B. S. & Baltà-Calleja, F. H., *Phys. Rev. E*, 1996, **54**, 989--992 .
- [8] Cahn, J. W., Hilliard, J.E., *J. Chem. Phys.*, 1958, **28**, 25.
- [9] Gunton, J. D., San Miguel, M., Sahni, P. S. In *Phase Transitions and Critical Phenomena*; Domb, C., Green, M. S., Eds.; Academic: New York, 1983; **8**.
- [10] Ryan, A. J., Fairclough, P. A., Terrill, N. J., Olmsted, P.D., Poon, W.C.K., *Faraday Discuss.*, 1999, **112**, 13.
- [11] Wang, Z. G., Hsiao, B.S., Sirota, E.B., Agarwal, P & Srinivas, S., *Macromols.*, 2000, **33**, 978-989.
- [12] Bras, W.; Derbyshire, G. E.; Mant, G. R.;

Clarke, S. M.; Cooke, J.; Komanschek, B. U.;
Ryan, A. J. *J. Appl. Cryst.* 1994, **28**, 26.

[13] Bras, W.; Derbyshire, G. E.; Ryan, A. J.; Mant,
G. R.; Felton, A.; Lewis, R. A.; Hall, C. J.;
Greaves, G. N. *Nucl. Instrum. Methods Phys.
Res.* 1993, **A326**, 587.

[14] Bras, W.; *J. Macromol. Sci.-Phys.* 1998, **B37(4)**,
557.

[15] Zhukov, V.; Udo, F.; Marchena, O.; Hartjes, F.
G.; van den Berg, F. D.; Bras, W.; Vlieg, E.;
Nucl. Instrum. Methods Phys. Res. 1997, **A392**,
83.

[16] Avrami, M., *J. Chem. Phys.*, 1939, **7**, 1103; *ibid*,
Avrami, M., *J. Chem. Phys.*, 1940, **8**, 212.

[17] Mark, J.E. *Physical properties of polymers*,
American Institute of Physics, NY, 1996.

Folded-back solution structure of monomeric Factor H of human complement by scattering, ultracentrifugation and modelling

Mohammed Aslam and Stephen J. Perkins

Department of Biochemistry and Molecular Biology, Royal Free and University College Medical School, University College London, Gower Street, London WC1E 6BT, U.K.

Received 19th February 2002; accepted 16th April 2002.

Introduction

Factor H (FH) of the complement system of immune defence is present in plasma at about 0.5 mg/ml. It consists entirely of 20 short complement/consensus repeat (SCR) domains, each of length about 61 residues, where SCR domains constitute the most abundant domain type in the complement proteins. The principal function of FH is to regulate the alternative pathway of complement activation by acting as a cofactor for factor I in the breakdown of C3b to form iC3b. The cofactor and decay accelerating activity are located within the four N-terminal domains, SCR-1 to SCR-4, which bind to intact C3b. A second C3 site is located within SCR-6 to SCR-10 which binds to the C3c region of C3b, and a third site is located within SCR-16 and SCR-20 which binds to the C3d region of C3b. FH also binds to heparin and other polyanionic substrates, where heparin modulates the complement regulatory functions of FH. Two heparin binding sites have been located in SCR-7 and SCR-20 in recombinant FH, and a third heparin binding site is suggested to be located at or near SCR-13. The SCR domains are thought to act synergistically to enable FH to achieve differential control of complement activation.

Molecular structures of FH are required to clarify its mechanism of action. However, its crystallisation is thought to be precluded by the 19 potential flexible peptide links between the 20 SCR domains and the existence of up to 9 putative glycosylation sites. Recent NMR and crystal structures for other proteins with two to five SCR domains showed that there is no preferred structural orientation between two adjacent SCR domains, thus it is not possible to deduce an overall structure for FH from these studies. Accordingly, to determine a medium-resolution molecular structure for FH, we have used x-ray and neutron scattering in conjunction with

automated molecular modelling methods to assess these interdomain linkers. The FH curve fits were highly constrained by the use of 17 homology models and three known NMR structures for the 20 SCR domains of FH [1]. The present article reviews the scattering approach that was used for FH in terms of our earlier applications of these automated rigid-body curve fit searches. The novelty of this strategy is that it is applied here for the first time to a linear arrangement of 20 domains [see refs 2-4]. Biologically useful information can be extracted from the medium-resolution structures obtained by scattering analyses [5].

X-ray and neutron scattering and ultracentrifugation of FH

X-ray and neutron scattering was performed with FH in the concentration range between 0.7-14 mg/ml. The joint use of x-rays and neutrons provided independent checks of self-consistency in the scattering curves. It was already known that FH is highly elongated in solution [6], thus the camera at Station 2.1 at SRS Daresbury was set up with sample-detector distances of up to 5.64 m in order to ensure that a sufficiently low Q had been obtained for Guinier analyses. For the same reason, after initial data collection on the LOQ camera at ISIS had verified its monomeric state, the final neutron scattering data were obtained on Instrument D11 with a sample-detector distance of 10 m and Instrument D22 with a sample-detector distance of 8 m, both at the Institut-Laue-Langevin. Full details are given in [1]. From the x-ray and neutron Guinier plots, the radius of gyration R_G of FH was determined to be 11.1-11.3 nm. These similar values indicated that radiation damage effects sometimes seen by x-rays were absent. Cross-sectional Guinier analyses revealed two linear regions. From these, two distinct radii of gyration of the cross-section R_{XS}

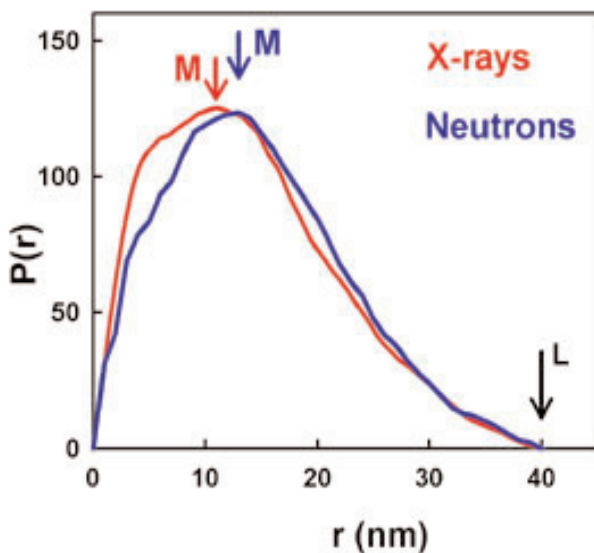


Figure 1: Experimental X-ray and neutron distance distribution functions $P(r)$ for FH.

I and R_{XS-2} were identified in two Q ranges to be 4.4 nm and 1.7 nm respectively. These were assigned to an averaged higher-order structure formed by the proximity of non-adjacent SCR domains in FH (R_{XS} of 4.4 nm) and the averaged cross-sectional structure of a line of SCR domains (R_{XS} of 1.7 nm) (see below). The x-ray and neutron distance distribution functions $P(r)$ for FH were of particular interest. In these, the most frequently occurring distance within FH (M) are similar at 11 nm (x-rays) and 12 nm (neutrons), and the maximum dimension is denoted by L which is 40 nm for both the x-ray and neutron data (Figure 1). If all the SCR domains in FH were fully extended in conformation, this would result in a length L of 73 nm for FH. This difference in the experimental and predicted L values shows that the 20 SCR domains of FH are folded back upon themselves in solution. Other analyses based on the neutron I(0)/c data from Guinier plots and from sedimentation equilibrium fits by analytical ultracentrifugation showed that FH was monomeric with a molecular weight of $165,000 \pm 17,000$ (neutrons) and $148,000-159,000$ (ultracentrifugation). The use of sedimentation velocity experiments showed that FH had a sedimentation coefficient of 5.3 ± 0.1 S. The combination of this value of 5.3 S with the RG determination of 11.1-11.3 nm in the modelling below provided an independent confirmation that the correct Guinier Q range had been identified for the RG determination. This was necessary as there was a chance that the true Guinier region for FH might

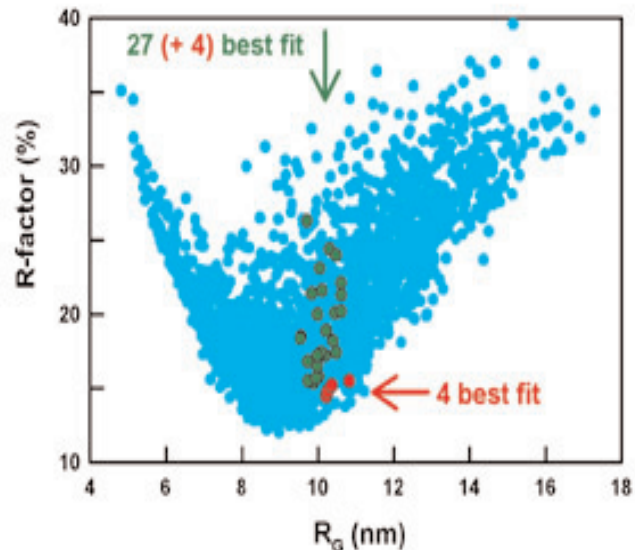


Figure 2: Comparison of the goodness-of-fit R-factor values for 2010 FH models with their RG values in one of the eight full automated conformational searches for a FH solution structure. The best fit solutions are highlighted in green and red.

have occurred at even lower Q values than that utilised here.

Automated modelling of the FH structure

Advances in modelling calculations have shown that scattering curves and analytical ultracentrifugation data are fully calculable from atomic structures [2,3]. Most notably, this method has been applied to determine the relative location of the two Fab and Fc fragments within antibody structures. Each of the Fab and Fc fragments was treated as a rigid body of known atomic structure. The modelling analysis identified the conformation of the two hinge peptides that connected each Fab-Fc pair by evaluating 12,000 variable conformations for these [4]. In comparison to antibody modelling, the major difference in the modelling of FH is the need to incorporate 19 variable linker peptide conformations to link the 20 SCR domains, not one. Despite the multiparameter nature of this new analysis, it was nonetheless possible to determine molecular structures from the scattering and ultracentrifugation data.

In order to initiate the FH modelling for the scattering curve and sedimentation coefficient fits, homology models were constructed for 17 of the 20 SCR domains using known NMR structures for FH SCR-5, SCR-15 and SCR-16 and other homologues. Trial calculations then evaluated the modelling strategy using different types of links. One FH model

was created using extended β -strands to connect the SCR domains. The known linker conformations from NMR and crystallography were used to make seven other FH models. While none of these models gave good scattering curve fits, they provided important clues. In particular, the RXS-1 value was found to be sensitive to the higher-order SCR structure while the RXS-2 value was not sensitive to the linker conformation provided that this was extended. In order to perform an automated search to identify best-fit FH structures, molecular dynamics simulations were used to generate libraries of 10,000 random conformations for each of the 19 SCR-SCR linker peptides. Peptides from these libraries were randomly selected for combination with the 20 SCR structures in order to generate stereochemically-complete models for the FH structure. In the automated curve fit procedure, a total of 16,752 FH models were generated from eight different searches of about 2000 models each, in each of which the assumptions made for the linker conformations were varied.

The typical outcome of one of the eight searches is summarised for 2010 FH models in Figure 2 in which a minimum length was specified for each of the 19 linkers (see [1]). Filters based on the experimental values for the R_G , R_{XS-1} and R_{XS-2} values from scattering and the sedimentation coefficient from analytical ultracentrifugation were used to retain or reject candidate FH models. Few models survived these filters, which illustrated the computational difficulty in identifying a good scattering fit model. The 31 best-fit FH models all

had RG values close to 11 nm (green and red in Figure 2). The lengths of these models ranged between 8 nm to 33 nm (see [1]), which is far less than the distance of 73 nm predicted for the most extended FH structure possible. From these 31 models, the four best-fit FH ones (red in Figure 2) were identified by their lowest R-factor values of between 12% to 15% in Figure 2b. Since the R-factors are generally between 1.2-8.7% for good scattering fit models [2], this showed that the four best-fit FH models were limited in their ability to describe the X-ray and neutron curves. Nonetheless it is concluded that only those FH models in which the 20 SCR domains were bent back upon themselves will fit the scattering and ultracentrifugation data.

Typical x-ray and neutron curve fits for one of the four best-fit FH models are shown in Figure 3, together with the α -carbon trace of the FH model in question. The upper curve fit corresponds to x-ray data from Station 2.1 at the SRS Daresbury, while the lower curve fit corresponds to neutron data from Instrument D11 at the Institut-Laue-Langevin. The continuous lines correspond to the calculated curve from each model. The arrowed ranges indicate the Q ranges used for the R_G , R_{XS-1} and R_{XS-2} analyses. These show that the overall structure as monitored experimentally by the R_G and R_{XS-1} parameters is well modelled, while the transition point in the scattering curve between the R_{XS-1} and R_{XS-2} regions is less well modelled. One explanation of this discrepancy is the inability to generate a sufficiently wide range of FH conformers in the computer time available for this project. It is also possible that, if there is sufficient interdomain flexibility in FH in solution, this would reduce both the detail in the FH scattering curve at large Q and the applicability of static models to represent this region of the curve. The four best-fit FH models are shown in Figure 4, in which the SCR-1 domains (grey) of the four models are superimposed. This indicates the folded back conformation of the FH structures, together with the random orientations of SCR-2 to SCR-20 that were generated in these models.

Conclusions

The solution data and their modelling show that the SCR domains in FH are folded back. These bent-back domain structures may correspond to conformational flexibility in FH that may enable the multiple FH binding sites for C3 and heparin to come

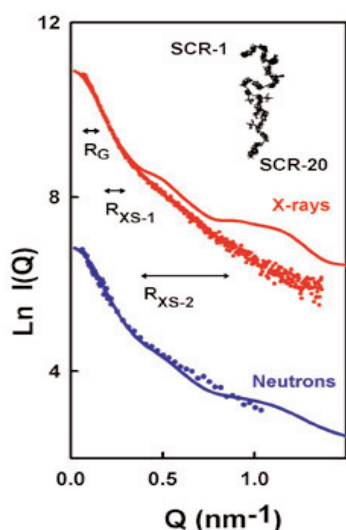


Figure 3: X-ray and neutron curve fits for one of the four best-fit models for FH that was identified from the automated search of FH models summarised in Figure 2.

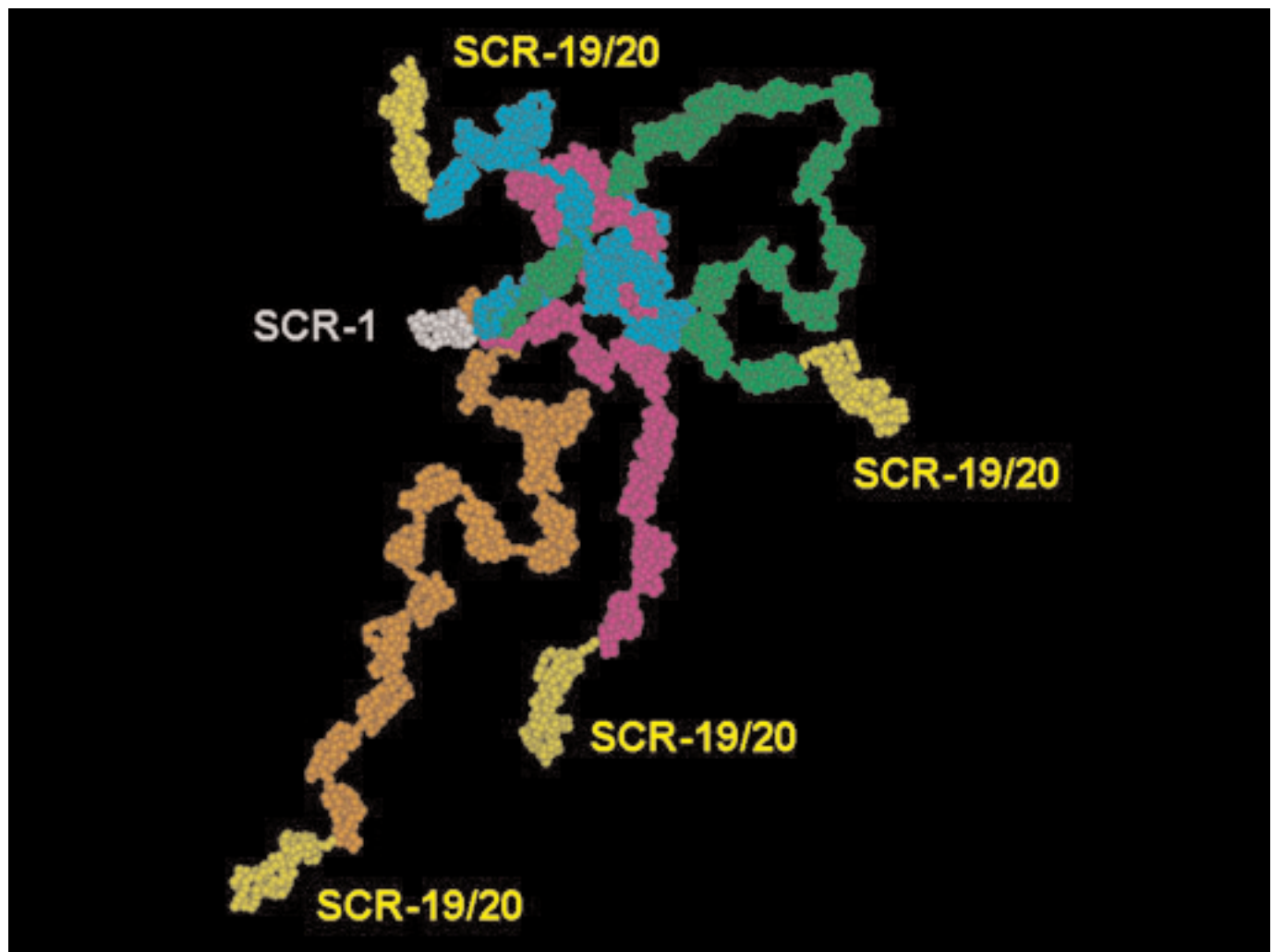


Figure 4: Positional summary of the four best-fit models for FH, all four of which are overlaid on SCR-1 (grey). SCR-19 and SCR-20 are highlighted in yellow.

into closer proximity. It is not clear at present why bent-back structures should occur, even though the known inter-domain orientations between SCR domains are variable. The most likely reason is the existence of five unusually-long linkers of lengths up to 8 residues between SCR-10/11, SCR-11/12, SCR-12/13, SCR-13/14 and SCR-18/19. These are mostly at the centre of the FH structure and may impart a higher degree of local flexibility to the FH structure to result overall in a structure that on average is not as extended as it could be. The automated rigid-body modelling strategy itself, which is based on 19 variable linkers here, as opposed to the single one used as a pair in antibody modelling, is seen to be sufficiently versatile to be successfully applied to

this system.

The biological utility of this medium resolution modelling was demonstrated by the use of the four best-fit FH scattering models to interpret the significance of 12 missense mutations found in FH that result in haemolytic uraemic syndrome, a disease involved with renal disorders and kidney failure [5]. Ten mutations occur in SCR-19 and SCR-20 (yellow domains in Figure 4). Eight of nine mutations in SCR-20 are shown in Figure 5a (two involve the same residue), while the tenth one occurs at D1101 in SCR-19. The homology model for SCR-20 [1] showed that the majority of these nine mutations are immediately adjacent to basic

conserved residues in SCR-20, that in turn could be correlated with a predicted heparin binding-site in SCR-20, for which a model could be built. Since the amino acid substitutions occur in both SCR-20 and SCR-19, the interdomain orientation between these was of interest. Despite the possibility that the three-residue linker connecting the two domains can vary in its conformation, Figure 5b shows that the range of this variation is restricted in the four best-fit models. The substitution at D1101 in SCR-19 (four yellow circles) is close to the predicted heparin binding-site in SCR-20 and may affect the linker

conformation. The scattering models therefore show that SCR-19 may contribute towards the formation of a heparin binding site in FH. We conclude that the medium resolution models generated by scattering modelling have utility for the interpretation of biological function.

Acknowledgements

We thank the Wellcome Trust and the BBSRC for their support, and Dr T. H. J. Goodship and Dr R. B. Sim for many useful discussions.

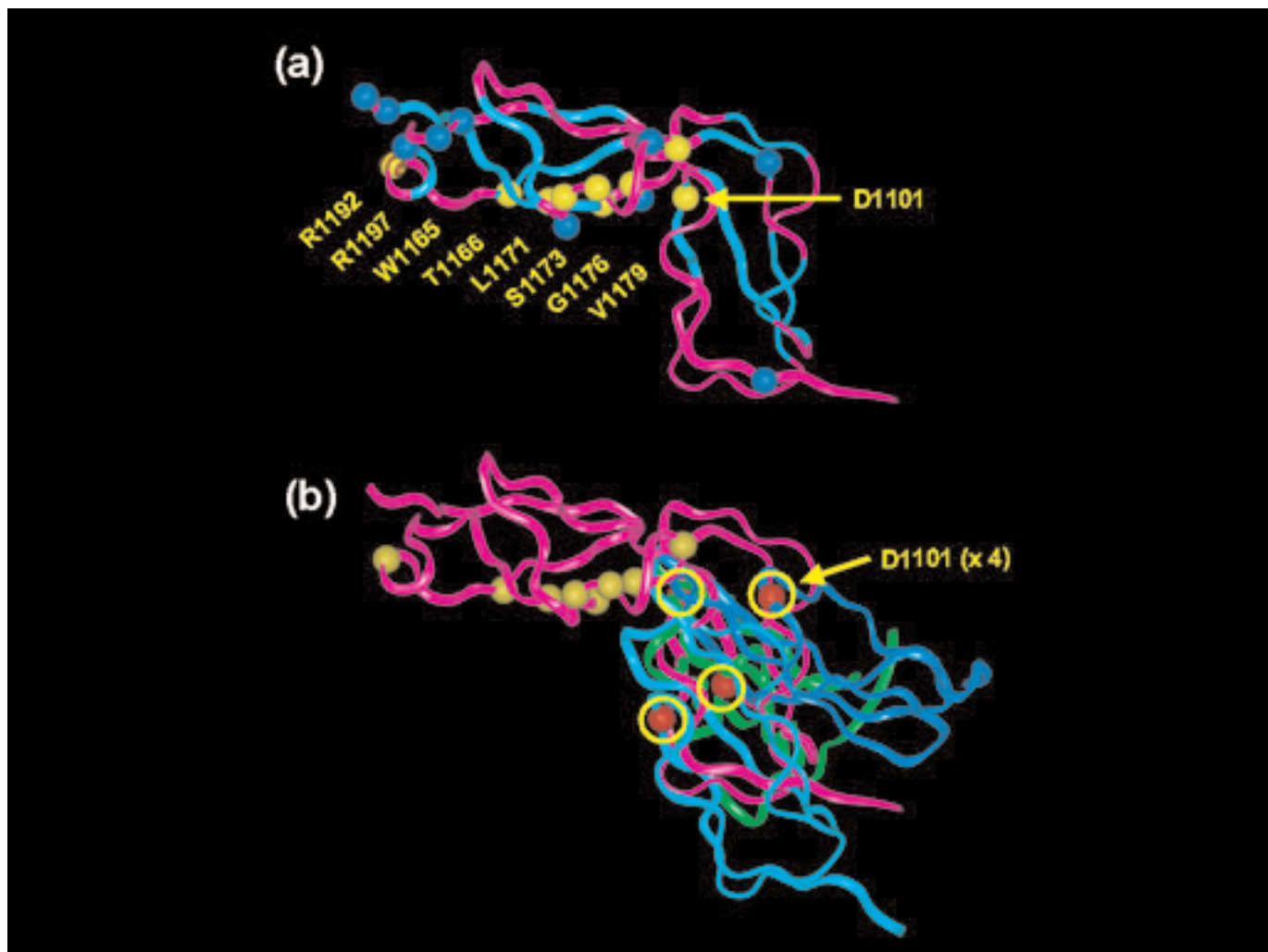


Figure 5: Use of the FH scattering models to provide a molecular explanation for haemolytic uraemic syndrome. (a) The single residue substitution in SCR-19 and nine in SCR-20 are shown as nine yellow spheres in one of the best-fit models (purple ribbon), together with the basic residues denoted as blue spheres. The b-strands are shown as blue ribbons. (b) SCR-19 and SCR-20 in the four best-fit models are shown superimposed on SCR-20, with the four positions of D1101 in SCR-19 denoted by yellow circles. The other three models are shown as blue and green ribbons.

References

- [1] Aslam, M. & Perkins, S. J. (2001) Folded-back solution structure of monomeric Factor H of human complement by synchrotron X-ray and neutron scattering, analytical ultracentrifugation and constrained molecular modelling. *J. Mol. Biol.* **309**, 1117-1138.
- [2] Perkins, S. J., Ashton, A. W., Boehm, M. K. & Chamberlain, D. C. (1998). Molecular structures from low angle X-ray and neutron scattering studies. *Int. J. Biol. Macromol.* **22**, 1-16.
- [3] Perkins, S. J. (2001). Applications of highly constrained molecular modelling scattering curve fits to biologically important proteins. *Fibre Diffraction Review*, **9**, 51-58.
- [4] Boehm, M. K., Woof, J. M., Kerr, M. A. & Perkins, S. J. (1999) The Fab and Fc fragments of IgA1 exhibit a different arrangement from that in IgG: A study by X-ray and neutron solution scattering and homology modelling. *J. Mol. Biol.* **286**, 1421-1447.
- [5] Perkins, S. J. & Goodship, T. H. J. (2002) Molecular modelling of mutations in the C-terminal domains of factor H of human complement: a new insight into haemolytic uraemic syndrome *J. Mol. Biol.* **316**, 217-224.
- [6] Perkins, S. J., Nealis, A. S. & Sim, R. B. (1991) Oligomeric domain structure of human complement factor H by X-ray and neutron solution scattering. *Biochemistry*, **30**, 2847-2857.

10th Annual Workshop Abstracts

Real Time SAXS/Stress-Strain Studies of Thermoplastic Polyurethane -A fibre diffraction approach to a non-crystalline material

D J Blundell

Department of Physics, Keele University

Elastomeric polyurethanes are synthesised from blocks of flexible, "soft" units linked together with rigid, "hard" blocks. Incompatibility between hard and soft blocks leads to phase separation giving two-phase morphologies with a spatial correlation of the order of 100Å that can be monitored by SAXS.

Despite their versatility for a wide range of uses, applications of polyurethanes are still limited by their relatively high mechanical hysteresis compared with other elastomers. This hysteresis and the associated mechanical loss processes can be partly attributed to the breakdown and reformation of the phase structure during mechanical cycling.

This presentation will focus on one aspect of an ongoing programme between Keele and Huntsman Polyurethanes and more recently with Bristol University. It involves measuring the SAXS patterns and stress during tensile deformation in order to follow the changes in morphology and identify effects associated with mechanical loss. It is currently believed that phase separation (on cooling or during solvent evaporation) generally occurs via spinodal decomposition followed by ripening. The exact nature of the final morphology is uncertain and depends on fabrication route and molecular formulation. In attempting to interpret the data we have therefore tried to minimise the number of prior assumptions about the structure. The presentation will describe one approach based on a statistical particulate model which borrows ideas from crystallography.

Axial disposition of myosin heads in contracting muscles

J. Juanhuix, J. Bordas, J. Campmany, A. Svensson, M. L. Bassford and T. Narayanan

Laboratori llum Sincrotron-LLS Edifici Cn. Campus UAB. E-08193 Bellaterra (SPAIN)

-Dept.of Physics and Astronomy, University of Leicester. Leicester LE1 7RH, UK.

-Europen Synchrotron Radiation Facility (ESRF). F-38043 Grenoble (France)

The development of high brilliance third generation SR sources (e.g. the ESRF) in conjunction with appropriate X-ray cameras and detectors allows the recording of the X-ray diffraction diagrams of muscle tissues with unprecedented resolution and precision. This offers the possibility to study important phenomena such as filament extensibility and symmetry for a variety of short-lived structural states (e.g. Bordas *et al.*, Biophys. J., 77, 3197-3207, 1999). Perhaps still more useful is that the brilliance of third generation SR sources allows the resolving of pronounced interference effects sampling the diffraction diagrams. These effects - due to the bipolar distribution of the motor proteins in the sarcomere - provide phase information and permit a direct visualisation of the disposition of the myosin heads during various forms of contraction (e.g. isometric, unloaded, overloaded, etc., e.g. Juanhuix *et al.*, Biophys. J., 80.)

Co-localisation of type I and type III collagen

Graeme Cameron

University of Stirling, Stirling, FK9 4LA

The molecular interactions between type I and type III collagen heterotypic fibrils are essential within some collagenous structures, yet these interactions are not understood to any significant level. The interactions can be modelled and compared to x-ray diffraction information from collagen structures which are rich in both type I and type III collagen (these include skin and the mitral valve complex of

the heart which contain 80% type I and 20% type III collagen). These diffraction studies have shown that the type I : type III complex containing structures have relatively similar x-ray diffraction patterns to that of rat tail tendon which is essentially type I collagen. Yet simulations of type III collagen diffraction patterns show significant differences to that of type I collagen. The intensities of the meridional reflections of the mixed fibrils are attenuated in the higher orders of the diffraction data. The reasons for this attenuation are not yet fully understood, although it could be related to the long-range helical structure of the collagen fibril which appears to be a characteristic of type I, type III heterofibrils. We have built models of heterotypic fibrils in order to simulate their diffraction pattern and to investigate the possible role of type III collagen in the long-range helical structure.

Pore formation studied by neutron reflectometry

Marcelo Nöllmann (1), Robert Gilbert (2), Michele Sferrazza (3), Olwyn Byron (1)

(1) Division of Infection & Immunity, Institute of Biomedical and Life Sciences, Joseph Black Building, University of Glasgow, Glasgow G12 8QQ

(2) Division of Structural Biology, Wellcome Trust Centre for Human Genetics, University of Oxford, Roosevelt Drive, Oxford OX3 7BN

(3) Department of Physics, School of Physics and Chemistry, University of Surrey, Guildford SU2 5XH

Pneumolysin (PLY), a 53 kDa protein, is a major virulence factor of the human pathogen *Streptococcus pneumoniae*. It causes damage to lipid bilayer membranes during disease and forms pores within them. Its receptor is cholesterol. We have performed small-angle neutron scattering, specular and off-specular neutron reflectivity studies on the PLY/membrane/cholesterol system to further understand the mechanism of pore formation. How does cholesterol function as a receptor? Does PLY translocate across the entire membrane bilayer? Is leakage of the membrane the result of pore formation by large PLY oligomers or bilayer instability caused by the insertion of individual PLY monomers? The answers to some of these questions will be presented in this talk.

Interactions of cations, water molecules and polysaccharide helices in oriented fibers and correlation with solution properties

Rengaswami Chandrasekaran, Srinivas Janaswamy and Wen Bian

Whistler Center for Carbohydrate Research, Purdue University, West Lafayette, IN 47907

X-ray diffraction patterns from well oriented and polycrystalline specimens recorded on photographic films are our source of experimental data for determining the three-dimensional structures of several industrially useful polysaccharides. In every case, polymer helices, constructed to be consistent with the helical parameters, have been packed in the unit cell appropriately consistent with space group and fiber density constraints and optimized by least squares refinement against the measured intensities. Guest molecules surrounding the helices have been located from electron density maps and the augmented crystal structures further refined to convergence. The emerging structural results in the solid state, in particular the interactions among the helices involving co-solutes and the solvent, help to understand the molecular basis of the observed solution properties of these biopolymers.

In the case of guaran, the galactomannan chain forms a flat, ribbon-like, 2-fold helix stabilized by hydrogen bonds from the galactosyl side-chains to the mannan backbone. Four helices are present in an orthorhombic unit cell. Water molecules promote the formation and subsequent stacking of sheets containing the polymer chains. The naked regions in the galactomannan are the sites of hydration that lead to good solubility and high viscosity in aqueous solution.

In the gellan family of anionic polysaccharides, a half-staggered, parallel, left-handed, 3-fold double helix is always maintained for the gel-forming gellan and the branched polymers welan, S-657 and rhamsan. The interactions involving up to three helices in trigonal unit cells, mediated by cations (e.g. sodium, potassium, calcium) near their carboxylate groups and stabilized by water molecules, correlate with the strong gelling properties of gellan and the thermal stability of viscosity exhibited by the rest.

A recent examination of its sodium and calcium salt forms confirms that iota-carrageenan exists as a half-staggered, parallel, right-handed, double helix. Three helices are present in a trigonal unit cell and their peripheral sulphate groups interact via ions and water molecules in forming the junction zones in carrageenan gels.

Scattering studies of plant cell wall polymers

Athene M Donald and Owen M Astley

Cavendish Laboratory, University of Cambridge

The plant cell wall is composed primarily of the polysaccharide cellulose, one of the most ubiquitous biopolymers in the world. Cellulose is the primary building block, and how it packs and responds to external mechanical stresses has important consequences for the viability of the plant. Scattering studies on a variety of cell wall systems will be presented, demonstrating how both long and short range order changes with stress. The consequences of interactions with other biopolymers in the cell wall will also be considered.

Crystallisation from ordered block copolymer melts.

JPA Fairclough, A.J. Ryan, S.C. Turner, S.M. Mai, L. Messe, W. Bras, R. Register, Y-L Lou

University of Sheffield, UK

ESRF Grenoble, France

Princeton, USA

Structure formation upon crystallization is of fundamental importance to the properties of semi-crystalline solids. We have studied the crystallization of semi-crystalline block copolymers where crystallization occurs from an ordered melt phase. The structure and degree of segregation of the melt phase plays an integral role in determining the structure formed during crystallization. Templating of directional order within the system is preserved in many cases. Results will be presented for a range of systems, morphologies and interfaces.

Structural changes and force generation in muscle cells

M.A. Ferenczi¹, A. K. Tsaturyan², Natalia Koubassova², Z.-H. He³ and S.Y. Bershitsky⁴

1 Imperial College, London, UK;

2 Institute of Mechanics, Moscow University, Russia;

3 NIMR, MRC, London, UK;

4 Institute of Ecology and Genetics of Micro-Organisms, Urals Branch of RAS, Yekaterinburg, Russia

Force generation in muscle originates from the cyclical interaction of myosin cross-bridges with actin filaments, coupled to the hydrolysis of ATP. The shortening of muscle cells is caused by the sliding of interdigitating filaments of actin and myosin, brought about by actomyosin interactions. It is now clear that the elementary movements involve cyclical changes in the structure of the myosin cross-bridges, and in the interactions between myosin and actin. It is these molecular changes which are responsible for the complex mechanical response of muscle fibres to rapidly applied changes in fibre length. Although various crystal forms of the motor domain of the myosin molecule have revealed their atomic structures, there is yet no atomic structure available for the actomyosin complex. Furthermore, protein crystallography does not reveal the dynamics of the structural changes which underlie movement.

Low angle x-ray diffraction of muscle obtained from live or contracting cells provides dynamic, nanometer-scale information which directly relates to the molecular changes responsible for force generation. Although the resolution is only adequate for domain-scale interpretation, and the interpretation remains model dependent, changes in the orientation of muscle cross-bridges on the sub-millisecond time scale can be resolved, as well as changes in the mode of binding of myosin to actin.

The results of recent experiments will be presented in which we show that force generation which accompanies an increase in temperature is caused by stereo-specific binding of myosin cross-bridges to the thin filaments. The shift from non-stereo-specific to stereo-specific binding is also investigated by the use of a myosin-derived, synthetic peptide which

perturbs the equilibrium between actin-attached cross-bridge states.

It will also be shown that cross-bridge binding to actin affects the structure of the thin filaments in a force-independent way.

Neutron reflectivity from model membranes

Fragneto Giovanna

Institut Laue-Langevin, Grenoble, France.

Neutron reflectivity has been applied to the study of model biological membranes. Models include flat phospholipid bilayers adsorbed on solid substrates with Langmuir Blodgett/Schaeffer or spin coating techniques. Results of structural determinations from those systems by means of specular neutron reflectivity will be given. Among the examples shown there will be the behaviour at the phase transition (critical swelling) of phospholipid bilayers, the interaction of lipid bilayers with the anti-bacterial peptide alamethicin or with DNA containing cationic liposomes.

Hierarchical structure of collagen and bone studied by x-ray scattering

Peter Fratzl

Erich Schmid Institute of Materials Science, Austrian Academy of Sciences

& University of Leoben, Jahnstr. 12, 8700 Leoben, Austria

Ludwig Boltzmann Institute of Osteology, Vienna, Austria.

Collagen-rich tissues constitute the major structural components conferring mechanical stability to vertebrates. These tissues have exceptional and highly variable properties, a consequence of their hierarchical architecture. At the lowest structural level, collagen consists of triple-helical molecules packed more or less regularly into fibrils.

The structure of the collagen fibrils is not completely solved but most of the information available to date has been obtained from fibre x-ray diffraction measurements with increasing resolution and sophistication. In bone, the fibrils are reinforced by mineral nanoparticles, the size and orientation of which can be studied by small-angle x-ray scattering

(SAXS) or fibre diffraction using x-rays or neutrons.

For a better understanding of the mechanical properties, higher levels of hierarchy have to be included. In the case of rat tail tendons, for instance, the strain in the collagen fibrils, measured by in-situ synchrotron x-ray diffraction, is only 1/3 of the total strain of the tendon, or even less. Recently, tendons were studied during tensile stretching using time-resolved fibre diffraction at different strain rates. The aim was to identify contributions from different hierarchical levels to the viscoelastic properties of the tendon.

A different approach was developed for the characterisation of hierarchical tissues, such as bone. In scanning x-ray microdiffraction, the specimen is scanned across a narrow x-ray beam. In this way, structural information is obtained on two scales simultaneously: the one defined by the evaluation of the scattering pattern (that is, the nanometer range) and the one defined by the beam cross-section (corresponding to the micrometer range). With laboratory equipment, bone can be studied by scanning-SAXS using a beam cross-section of 100 micrometer. This lateral resolution of the scanning process can be pushed to a few micrometers and even to the sub-micrometer range using synchrotron radiation. By this new approach, structures can be characterised in the range between nanometers and millimeters, contributing to a better understanding of complex biological materials.

Model-independent maximum - entropy inversion of SAXS data

S. Hanna¹, J.A. Elliott²

(1) Physics Department, Bristol University

(2) Materials Science Department, Cambridge University

A model-independent maximum-entropy method is presented which will produce a structural model from 2-dimensional SAXS data of disordered systems using no other prior information. In this respect, it differs from conventional maximum-entropy methods which assume the form of scattering entities *a priori*. The method is demonstrated using data obtained from perfluorinated ionomer membranes, liquid crystalline copolymers, polyurethanes and other semi-crystalline polymers.

Evidence of spinodal decomposition in semi-crystalline polymers

E.L.Heeley^a, W.Bras^b, I.P. Dolbnya^b, A. Maidens^c, P.D.Olmsted^c & A.J. Ryan^a

a) Chemistry Department, University of Sheffield, Brook Hill, Sheffield, S3 7HF, UK.

(b) ESRF, BP220, F-38043, Grenoble Cedex, France.

(c) IRC, Physics Department, University of Leeds, Leeds, LS2 9JT, UK.

crystallizations of the polymers investigated. The new detector technology with significantly increased sensitivity at the ESRF, has indicated that spinodal decomposition can still be used to describe early structure development during an induction period. However, the increased WAXS detector sensitivity has shown that induction periods are reduced and low isothermal crystallization temperatures have failings when evaluated by the CH theory, compared with previous data obtained. Nevertheless, the spinodal temperatures obtained for samples still correlate well with past and present data collected on both beam lines.

Astringency - a molecular approach

Elisabeth Joebstl

University of Sheffield

Astringency is generally described as a feeling of dryness, puckering or rough mouthfeel and is associated with a number of beverages, including tea, coffee, wine, beer and vegetables and fruits like spinach and dates. All these beverages and foodstuff are similar in that they contain polyphenols.

The sensation of astringency is considered to derive from polyphenols and their ability to bind, and precipitate proteins within the mouth. The major proteins in the mouth are the proline-rich proteins (PRPs), which make up approximately 70% of the protein saliva and contain a high content of proline (25-45 %), glutamine and glycine. These salivary proline rich proteins can be divided in three groups: acidic (30%), basic (23%) and glycosylated (17%) PRPs. The acidic PRPs are believed to bind oral bacteria and to prevent the growth of hydroxyapatite crystals at the surface of the tooth *in vivo*. It has been proposed that the main task of the glycosylated PRPs is lubrication of the mouth surface and the basic PRPs are considered to bind and precipitate polyphenols.

There are two main structures of polyphenols: Condensed proanthocyanidins and gallic acid derivatives or hydrolysable tannins and minor structures such as phlorotannins and phloroglucinol. The affinity of binding increases with the number of aromatic rings which substantiates the theory that the main binding effect is a hydrophobic stacking of the phenolic ring over a proline, whereas hydrogen

Several samples of commercial and synthesized polymers such as iPP and PET have been used to provide evidence that SAXS does occur prior to WAXS during isothermal crystallizations. This has led to the theory that primary crystallization can be described as being a phase separation process rather than a nucleation and growth scenario as classical models predict during an initial induction period. Thus, the experimental SAXS data have been seen to follow the kinetics of spinodal decomposition and have been analyzed using the Cahn-Hilliard (CH) linearized growth theory. This describes the time evolution of the scattering intensity to follow an exponential growth from increased amplification of density fluctuations. The fitting of the CH theory to the scattering data gives an extrapolated value for the spinodal temperature. Below this temperature the polymer is said to spontaneously separate into two phases.

Data collected on both beam lines have shown evidence of SAXS before WAXS in isothermal

bonds are less important.

After the initial binding three mechanisms have been suggested that lead to precipitation:

*Multiple binding of polyphenols

*Polyphenol-polyphenol stacking interaction

*Multiple binding of the proteins

The formation of aggregates as well as the growing of the complexes is temperature dependent as well as pH dependent.

Swelling of normal and pathological corneal stroma.

S.Khan, S.Akhtar, K.M.Meek.

Optometry and Vision Sciences, Cardiff University, Cardiff CF10 3NB, Wales.

PURPOSE. Corneas swollen in vitro, at physiological pH with a bounding membrane will remain transparent even at pH8 (Huang Y and Meek KM, Biophysics J. 77, 1655-1665,1999) while corneas swollen in vivo become opaque. Our purpose was to compare the swelling of Fuchs' dystrophy and normal corneas to explain this anomalous behaviour.

METHOD.

Experiment 1: Bovine corneas were swollen at pH 8 and pH 5 and final pH3.2 and pH5 using a bounding membrane. Experiment 2 : Normal and Fuchs' dystrophy corneas were either swollen by addition of physiological saline or were equilibrated against different concentration of polyethylene glycol (PEG) in phosphate buffer to a range of final hydrations. The corneas were examined by x-ray diffraction (XRD) and transmission electron microscopy (TEM).

RESULTS. Experiment 1: At pH 8 the corneas at both hydrations appeared clear while at pH 5 the corneas at both hydrations appeared opaque. XRD revealed no correlation between collagen interfibrillar spacing, fibrilar diameter and appearance of tissue. But a correlation was observed between degree of order of the fibril packing and appearance of tissue. A high degree of order was found in the clear corneas while a low degree of order occurred in opaque corneas. Experiment 2: Both normal and Fuchs' dystrophy corneas swelled on addition of saline. All saline-swollen corneas

were opaque. Although the final hydrations were different, XRD revealed there was little difference in interfibrillar spacing between Fuchs' dystrophy and normal corneas, but a low degree of fibril packing order was observed. TEM revealed the presence of numerous large intra-lamellar 'lakes'.

CONCLUSION. Corneas swollen in vitro appear opaque because of the formation of collagen-free 'lakes' and an accompanying disordering of the fibril packing. Swelling with a bounding membrane in the region of neutral pH can reduce these effects and allow a more even water distribution and hence a clearer cornea.

Differences in the swelling behaviour of normal and Fuchs' dystrophy corneas may relate to compositional changes in the source of the osmotic force controlling hydration (probably including changes in proteoglycans) manifested here by a different response to equilibration against PEG. The X-ray diffraction and electron microscope results suggest the presence of more 'lake' formation as the Fuchs' cornea swells (compared to the swollen normal cornea) perhaps for the same reasons. The distribution of tissue water, and hence the resulting light scattering in Fuchs' dystrophy corneas, is probably a consequence of these compositional changes, which do not occur when normal corneas are swollen in vitro near neutral pH with a bounding membrane.

Structure, Fluctuations and Transitions of Lipid Model Membranes

Peter Laggner, Manfred Kriechbaum, Georg Pabst, Michael Rappolt, and Heinz Amenitsch

Institute of Biophysics and X-ray Structure Research, Austrian Academy of Sciences

The structural dynamics of lipid bilayers and non-bilayer phases are highly sensitive to their physical and chemical environment. Time-resolved X-ray diffraction covering both the small- and wide-angle region under different solvation conditions, in bulk liposome and solid-supported states, resp., have resulted in a host of novel information. Most strikingly, the liquid-crystalline state of hydrated multilayers shows discrete steps of solvation, which suggests a non-monotonous interaction potential between adjacent bilayers. Such states appear also as

transient intermediates in T-jump relaxation experiments as short-lived intermediates with sub-second life-times. These observations can be interpreted in terms of a foam model of liposomes. Undulation phenomena, as can be quantified by advanced methods of data analysis, play a central role in this model.

Myosin head configuration in relaxed *lethocerus* fibrillar insect flight muscle from low-angle x-ray diffraction

Hind A. AL-Khayat¹, Liam Hudson¹, Michael K. Reedy², Thomas C. Irving³ & John M. Squire¹

(1)Biological Structure and Function Section, Biomedical Sciences Division, Imperial College of Science, Technology & Medicine, London SW7 2AZ, UK

(2)Department of Cell Biology, Duke University, Durham, NC 27710, USA

(3)Department Biological, Chemical and Physical Sciences, Illinois Institute of Technology, Chicago IL, 60616

In the interest of studying the molecular structure and function of muscle, we are trying to determine the 3D structure of actin and myosin filaments and the structural changes underlying contraction and its regulation. Our main approach involves using simulated annealing and local refinement methods developed in a BBSRC-funded study of X-ray diffraction data from fish muscle. Here, these methods are being used with the aim to solve the full unit cell structure in relaxed insect flight muscle and also rigor insect muscle. Actin molecules and myosin heads are particularly well organized in insect flight muscles and give rise to semi-crystalline low-angle X-ray diffraction patterns.

We have already analysed and solved the structure of myosin thick filament in relaxed insect flight muscle. We are now refining this structure and propose to apply these methods to solve the full unit cell, including the actin filaments with troponin and tropomyosin, in both the relaxed and rigor insect flight muscle using new X-ray diffraction data. This will provide direct information on the actin-myosin interface and also on the conformation and the flexibility of the myosin heads in different defined states.

In this meeting, we will present a poster showing our latest results on this project.

Reaction kinetics and morphology development in flexible polyurethane foam

Wu Li, Ellen Heeley, Anthony J Ryan

University of Sheffield, Sheffield S3 7HF

Flexible polyurethane foams are formed from the simultaneous exothermic reaction between a diisocyanate with a polyether polyol and water. The morphology of these foams is determined by the competition between the polymerisation and the microphase separation of the 'hard' and 'soft' segments. The hard-segments are formed by the water and diisocyanate reaction producing a polyurea, whereas the soft-segments are formed by the polyether polyol chains¹.

Adiabatic temperature rise measurement (ATR) and forced-adiabatic FT-IR spectroscopy (FT-IR) have been employed to simultaneously monitor polymerisation on toluene diisocyanate (TDI) based

Two particular muscle systems have been discovered that because of their superb degree of order, provide technical advantages in structural studies. In the case of vertebrate muscles, it is the muscles of fish that are particularly useful for this, whereas in the case of the invertebrates it is insect flight muscles that are the most beautifully organised of all.

flexible polyurethane foam system, varying the content of surfactant and catalyst. The decay of isocyanate is correlated to the polymerisation kinetics². There is a good correlation between the conversion of isocyanate calculated from ATR and FT-IR data. As the catalyst concentration in the formulation is increased, it has been observed that the overall relative rate of reaction increases. However, the overall relative rates of reaction are the same among the foaming systems with different surfactant concentration.

Forced-adiabatic, time-resolved synchrotron small angle X-rays scattering (SAXS) has been employed to investigate the dynamics of microphase separation during the fast bulk copolymerisation³. Initially, there is little scattering (homogeneous liquid), and the peak that starts to grow at $q^*0.06 \text{ \AA}^{-1}$ after 81 seconds is evidence for the structural development in the TDI sample. The peak position does not change during the whole process. Microphase separation was observed to occur at a critical conversion of isocyanate functional groups and is shown to follow the kinetics associated with spinodal decomposition. The presence of covalent cross-links is observed to delay the microphase separation of the urea hard-segments. Dynamic rheological measurements have been conducted during the bulk copolymerisation via a vane rheometer⁴. The increase of the modulus of the foaming mixture is resulted from the microphase separation of the hard-segment.

References:

- [1] Armistead, J.P., Wilkes, G.L., Turner, R.B., *J. Appl. Polym. Sci.* 1988, **35**, 601-629.
- [2] M.J. Elwell, Ph.D. thesis, University of Manchester, 1993.
- [3] Elwell, M.J., Stephen, M., Ryan, A.J., *Macromolecules*, 1994, **27**, 5428.
- [4] Zhang, X.D., Giles, D.W., Barocas, V.H., Yasunaga, K., Macosko, C.W., *J. Rheol.*, 1998, **42(4)**, 871.

Hanging by a Thread

Stephen King¹, David Bucknall², Haskell Beckham³ & Richard Heenan¹

1) ISIS Facility, RAL, Chilton, Didcot OX11 0QX, UK

(2) Dept of Materials, University of Oxford, Parks Road, Oxford OX1 3PH, UK

(3) School of Textile & Fibre Eng, Georgia Inst Tech, Atlanta, USA

Nylons (polyamides, polycaprolactams) are amongst the worlds truly great commodity polymers. First developed by Wallace Carothers and DuPont in the 1930's their use today extends beyond parachutes, ladies hosiery and related textile applications; 35% of world output is now directed into the automobile industry, chiefly for tyre production. The one thing that all these uses have in common is that nylons are excellent polymers to form fibres from.

The physical properties and the microstructure of nylons have been investigated by an array of techniques over the last 25 years, including SAXS/WAXS and SANS. Indeed, these scattering studies are a textbook example of the complementarity between X-ray and neutron methods. Of particular interest has been the effect of hydration on the properties of the fibres and how macroscopic changes can be explained at the microstructural level.

This talk, based on some recent SANS experiments and preliminary analysis, will be concerned with the effect of acid, alkali and surfactants on the microstructure of nylon-6 and the implications for a particular use of this polymer.

Collagen orientation in the human cornea and its implications for eye surgery

Keith M. Meek and Richard H. Newton

Cardiff University, Redwood Building, King Edward VII Avenue, Cardiff CF10 3NB

Collagen in the corneal stroma is laid down in the form of lamellae, each containing an array of parallel collagen fibrils. The lamellae are all in the plane of the eye globe, and the direction of collagen in one lamella is very different to that in the adjacent lamellae. Fibrils thus occur in all directions in the

plane of the cornea and give the tissue radial strength. X-ray scattering revealed that, in the human cornea, there are two preferred orientations of the collagen, nasal-temporal and inferior-superior. We have been quantifying this orientation across the cornea and into the limbus, where the radius of curvature changes abruptly. The results showed that the orthogonal arrangement of the preferred orientation is maintained across the cornea to within about 1.5 mm of the limbus at which point a continuous change to an annular disposition of collagen occurs. We have examined some of the features of this circum-corneal annulus. By producing a detailed map of preferred collagen orientation in the normal cornea and limbus, we have started to explain the different post-surgical results (particularly with respect to astigmatism) of corneo-limbal incisions made at different points in the tissue and in different directions. In the near future, these techniques could also be applied to understand structural changes that occur in various corneal diseases.

Micro-deformation of polyurethane foams

C.Martin^a, G.Eeckhaut^b, A.Mahendrasingam^a, D.Blundell^a, W.Fuller^a and C.Riekel^c

(a) Department of Physics, School of Chemistry and Physics, Keele University, Staffordshire, ST5 5BG UK.

(b) Polymer Science Group, Polyurethanes R & D, Huntsman (Europe) BVBA, Everslaan 45, B-3087 Kortenberg, Belgium.

(c) ESRF, B.P. 220, F-38043 Grenoble Cedex, France.

the first time and have enabled the calculation of the principal characterising parameters of the polymer comprising the struts together with information on the variation of structure as a function of strain. Pertinent comparisons with similar measurements made on bulk foams are made.

Crystallization from Sheared Melts of Linear and Branched Polyethylenes

G.R.Mitchell, J.J.Holt, S.A.Thornley and C.K.Chai

Polymer Science CEntre, University of Reading, Whiteknights, Reading RG6 6AF

BP snc Lavera France

The use of in-situ probes to explore the molecular and morphological changes which accompany polymer processing provides useful insight into the critical stages of such processes. We report on the application of in-situ time-resolving x-ray and neutron scattering techniques to the study of crystallisation of polyethylene and polyethylene blends from sheared melts. The combination of neutron and x-ray scattering provide details on several length scales both during shear flow and subsequent to flow during crystallisation. We have used these techniques to explore the relationships between shear history and the subsequent anisotropic crystal growth. These reveal the massive amplification in anisotropy which occurs on crystallisation and the dependence on a critical shear strain (i.e. shear rate independence) for anisotropic crystal growth. We have used ex-situ transmission electron microscopy to complement these in-situ techniques. We have used the information on the different length scales to construct a qualitative model of the crystallisation process.

A compact device based on a piezoelectric actuator has been developed for the deformation of micron-sized polymer fibres. Specifically designed for the collection of micro-SAXS on the Microfocus Beamline ID13 at the ESRF, the device has a built-in high-resolution force transducer and video imaging system.

Results from a series of time-resolved tensile deformation experiments on single structural units of elastomeric polyurethane foams, the struts, are presented. Measurements of true stress, local strain and correlated SAXS patterns have been possible for

Structural mechanisms of self-assembly and polymorphic supercoiling of the bacterial flagellum

Keiichi Namba

Protonic NanoMachine Project, ERATO, JST & Advanced Technology Research Laboratories, Matsushita Electric Industrial Co., Ltd.

The bacterial flagellum is a helical filament by means of which bacteria swim. Each flagellum is rotated by the flagellar motor at its base and works as a propeller. The filament is not a simply rigid propeller, but is designed to quickly change its helical handedness for alternating the swimming pattern of bacteria between running and tumbling for chemotaxis. Thus, the function of the filament involves a dynamic switching mechanism.

The flagellum is formed by well regulated self-assembly. The assembly starts with a rotor ring formation in the cytoplasmic membrane by FliF. To extracellular side, a short rod assembles on the FliF ring, and continues to the hook and the long helical filament, which grows to as long as 15 mm by self-assembly of about 32,000 flagellin molecules. The component proteins are exported through the central channel to the distal end. Cap proteins are attached to the growing end to promote efficient self-assembly of appropriate proteins. For the filament growth, the cap protein is FliD, also known as Hook Associated Protein 2 (HAP2). The structure of the cap-filament complex and the isolated cap dimer revealed by electron cryomicroscopy and single particle image analysis show a pentameric structure of the cap, composed of a pentagonal lid-like domain and five leg-like domains that extend into the hole at the distal end of the filament. The structures and the interactions between the cap and filament over symmetry mismatch indicate that the cap must rotate by rearrangement of the five leg domains upon every flagellin assembly to prepare always one binding site for the next flagellin assembly. The predicted movements look as if the five-leg table walks up the helical steps at the distal end of the filament tube.

The flagellar filament is a helical assembly of a single protein flagellin, and therefore its helical form is a supercoil. The filament can be described as a tubular structure made of 11 protofilaments. The supercoiling is thought to involve two distinct conformations and packing interactions of the

protofilaments. We used X-ray fiber diffraction, electron cryomicroscopy and X-ray crystallography to solve the structures of two types of straight filaments, L-type and R-type, which represent the two distinct subunit packing interactions. The filament structures revealed that the well-conserved terminal regions of flagellin form axially aligned α -helical bundles in a concentric double tubular structure in the filament core. The inner-tube domain folds up into a compact structure only upon assembly and that is how the self-assembly process is regulated. The polymorphic supercoiling is achieved by an axial lengthwise switch with sub-angstrom accuracy in the outer tube domain of the protofilament. We solved the crystal structure at 2.0 Å resolution of a 41-kDa fragment of flagellin, F41, which was prepared by truncating terminal segments. In the crystal, we identified the protofilament structure having the shorter repeat distance corresponding to R-type. By simulated extension of this protofilament model, we identified a possible switch region responsible for the lengthwise mechanical switch within the molecule. We are currently trying to build atomic models of the two straight filaments by using the F41 model and based on the structural data we have collected by X-ray fiber diffraction and electron cryomicroscopy, in order to look into the coupling mechanism of the twist and curvature that defines supercoiled forms of the flagellar filament.

Phase behaviour of block copolymers in solution

Alex Norman¹, Patrick Fairclough¹, Simon Turner¹, Shao-Min Mai², Colin Booth²

1. University of Sheffield.

2. University of Manchester

The phase behaviour of triblock copolymers of oxyethylene and oxybutylene are investigated by SAXS, Rheology and Optical Microscopy. As the concentration of polymer is increased the micelles which form pack into various geometric arrays forming gels. Generally they form in the order cubic to hexagonal to lamella with increasing concentration. Rheology and Optical Microscopy

show the existence of such phases. A hexagonal phase has been recognised using optical microscopy for a 45wt% sample of B11E47B11. This phase was confirmed by the rheological data and the SAXS data.

Simultaneous SAXS/WAXS/DSC experiments have been performed on beamline 8.2 of the SRS CCLRC Daresbury Laboratory, and on BM26 DUBBLE at the ESRF. All data were fitted to a Pearson VII function to monitor the d-spacing, peak width, and peak area, and intensity as a function of temperature. A double log plot of the reciprocal intensity versus reciprocal temperature can easily indentify the order-disorder transition temperature, ODT. The peak-to-peak ratio changed in many of the samples during the temperature ramp experiments, indicative of a phase change. It has been shown that the domain spacings get larger on heating the samples, and larger still on reducing the concentration of polymer.

For many of the samples simultaneous SAXS/Couette Cell experiments were performed at beamlines 2.1 and 16.1 of the SRS CCLRC Daresbury Laboratory. An applied constant or oscillatory shear will orient the domains within the sample. This has been done previously by Hamley *et al* (*Macromolecules*, **30**, 5721, (1997)).

For the samples of B25E90B25 at various concentrations this experiment has shown the existence of cubic, hexagonal and lamella phases with changes in temperature as well as concentration. Form Factor analysis has been carried out on some of the data collected. It has been deduced that for 32.5wt% B16E60B16 at low temperature the phase shown is cubic rather than hexagonal which is what the scattering pattern suggests), due to the position of a minimum in the form factor at root 2. From all the rheology, microscopy and scattering data it has been possible to construct phase diagrams for some of the samples studied. Work is now being done to attempt to study the kinetics of these transformations, which will be fitted to an Avrami curve.

Culture of *Escherichia coli* cells for the investigation of hydration patterns in fully deuterated DNA and synthesis of selectively deuterated DNA analogues for the investigation of base pair geometry in novel conformations of polymeric DNA

Ingrid Parrot^{1,2}, Trevor Forsyth^{2,1}, Watson Fuller¹, Paul Langan³

¹Physics Department, Keele University, Staffordshire, ST5 5BG England

² Institut Laue Langevin, 6 Rue Jules Horowitz, 38042 Grenoble Cedex 9, France

³ LANSCE, Los Alamos National Laboratory, New Mexico, USA

Neutron fibre diffraction, in conjunction with the isotopic replacement of H₂O by D₂O, provides a powerful way of investigating hydration patterns in DNA. The option of selectively deuterating particular residues in the DNA double helix also has huge potential for investigating DNA conformation, although this has not been done in the past because the labelling methods are complex.

Here we describe two kinds of biological study that can be carried out at the ILL: the high-cell-density cultivation of *Escherichia coli* and the synthesis of selectively deuterated DNA containing a strictly alternating sequence of adenine and thymine residues. In this last case, such sequences have unique biochemical/biological properties and adopt DNA conformations that in many cases can only be observed in the DNA polymers and not in oligonucleotides. The work is now at a stage where a neutron diffraction study of D-DNA containing deuterated adenine residues is foreseen using instrument D19 at the Institut Laue Langevin (ILL, Grenoble).

Determination of the Phalloidin Position in F-actin using Fibre Diffraction Data

Toshiro Oda^{1,2} Kenneth C.Holmes¹

1. Max Plank Institute for medical reserach, Dep. of Biophysics

2. RIKEN harima Institute, Lab. of structural biochemistry

it were determined with precision of ca 2 Å and 20 degree, respectively. Above all, when the center of one actin subunit in F-actin is put on the x-axis, the position of phalloidin was determined to be located at 8.5-11.0 Å in radial direction, at -1.9-1.2 Å in helical axis direction and at 84-103 degree in the rotation direction. Finally, we refined the orientation and position using the F-actin model and the diffraction data. The final result supports the phalloidin position refined in the Lorenz model.

Some small peptides, such as phalloidin etc, bind to F-actin and control the regulation of the cytoskeleton. Detailed knowledge about the control of the cytoskeleton is important for medical science. Lorenz *et al.* refined an F-actin with phalloidin model that was consistent with fibre diffraction patterns from phalloidin-F-actin sols and stereochemical constraints by allowing modifications of the crystal structure of actin and the NMR-structure of phalloidin. In this study, we determined the position of phalloidin in a more straightforward way using fibre diffraction patterns and confirmed their model. We developed a simple method of determining a binding position of a small peptide on F-actin at low resolution.

We obtained fibre diffraction patterns from well-oriented F-actin sols with and without phalloidin. We extracted the amplitudes along the layer-lines from the diffraction patterns at a resolution of 8 Å. First, we calculated J_0 -differential Patterson map (cylindrical averaged Patterson map) to determine the radial position of the phalloidin. Peak positions in the map approximately correspond to the relative positions of palloidin, showing that phalloidin is located at 8.5-11.0 Å from the helical axis of F-actin. Second, we refined the radial position and determined the orientation of phalldoin in a similar way to the crystallographic refinement of heavy atom derivative without knowledge of protein phase information. Although the precise orientation could not be determined with high confidence, two candidates with the fittest orientation were determined. Third, on the basis of the position and orientation of phalloidin, we calculated the phase angles along the layer-lines for F-actin and determined the relative position against the F-actin model, the position along the filament helical axis and the rotation about it, using the phase difference between the calculation and the model. The position along the filament helical axis and the rotation about

The three-dimensional structure of type I collagen

Joseph P.R.O. Orgel*, Andrew Miller*, Thomas C. Irving, Robert F. Fischetti, Andrew P. Hammersley, and Tim J. Wess*

*Department of Biological Sciences, University of Stirling, UK.

CSRRI and Dept. BCPS, Illinois Institute of Technology,

Collagen is the most abundant protein in mammals, where it functions as the main component of the connective tissues which maintain the structural integrity of the organism. We present here for the first time a directly determined three-dimensional image of the arrangement of collagen molecules in the fibrils of tendon in the native state. This is in the form of an electron density map which has been obtained by the multiple isomorphous replacement (MIR) method used in protein X-ray crystallography; it immediately reveals the quasi-hexagonal packing of the collagen molecules and the sites of the cross-linked telopeptides which are central in understanding the function of both normal collagen fibrils and those in connective tissue diseases. It also shows a novel regular arrangement of ordered and disordered domains in the fibril.

The Fab and Fc fragments in the antibody subclass IgA2 exhibit a different arrangement from that in the IgA1 subclass: a study by solution scattering, ultracentrifugation and homology modelling

Alex Robertson, Patrick W. Whitty, Michael A. Kerr, Jenny M. Woof and Stephen J. Perkins

Department of Biochemistry and Molecular Biology, Royal Free Campus, Royal Free and University College Medical School, University College London, Rowland Hill Street, London NW3 2PF, U.K.

correct IgA2 models can be generated, a small subset of which is able to satisfy a set of constraints based on the parameters from the scattering and ultracentrifugation data. From these searches, it is concluded that the observed compact IgA2 structure is the consequence of its much shortened hinge peptide length. As this makes IgA2 structurally distinct from IgA1, it is possible that IgA2 may have a distinct immune role from that of IgA1 in plasma and mucosa, and evidence for this will be discussed.

Effect of homopolymer addition to the morphology of a block copolymer in the bulk and in thin films

C. L. O. Salou, A. J. Ryan and J. P. A. Fairclough

Department of Chemistry, University of Sheffield, Dainton Building, Sheffield, S3 7HF

Human immunoglobulin A is an abundant antibody that occurs as two major subclasses, IgA1 and IgA2. It mediates immune protection at mucosal surfaces as well as in plasma. Both isotypes contain two four-domain Fab fragments and a four-domain Fc fragment analogous to that in immunoglobulin G. In IgA2 these are linked by a hinge region made up of 8 amino acids from each of the heavy chains, while the length of this hinge in IgA1 is 23 residues. IgA2, like IgA1, also has two 18-residue tailpieces at the C-terminus of each heavy chain in the Fc fragment. X-ray scattering using H₂O buffers and neutron scattering using 100% 2H₂O buffers were performed on recombinant monomeric IgA2. The radius of gyration R_G from Guinier analyses is 5.1 nm, which is significantly smaller than that of IgA1 at 6.11-6.20 nm. The cross-sectional radii of gyration R_{XS} were similar for both IgA2 and IgA1. The distance distribution function P(r) for IgA2 showed a single peak and a maximum dimension of 17 nm, while that for IgA1 showed two distinct peaks and a maximum dimension of 21 nm. The sedimentation coefficient of IgA2 was determined to be 6.2 S. These solution data indicate that IgA2 is structurally significantly more compact than IgA1. The homology modelling of the IgA2 structure showed that the intact structure can be readily assembled using known crystal structures for IgG Fab and Fc fragments. We have now initiated an automated curve fit search constrained by these homology models in order to model the experimental IgA2 scattering curves and its sedimentation coefficient. This is based on the use of molecular dynamics to generate random IgA2 hinge structures to which the Fab and Fc fragments could be connected in any orientation. Our results to date show that a large number of stereochemically

Diblock copolymers upon cooling (from the melt) or upon solvent evaporation (from solution) exhibit different microphase-separated morphologies including spheres, hexagonally packed cylinders and lamellar structures. The relative volume fraction of each block along with the Flory-Huggins interaction parameter (c) and the degree of polymerisation dictates the morphology formed, and surface effects are important for determining the ordering process in thin films.

The requirements for the lamellar morphology are that the volume fraction of one block being $0.4 < f < 0.6$, to obtain alternating layers. If asymmetric starting materials are used, it is possible to obtain a lamellar morphology by preparing blends with homopolymer(s). In these blends, the free energy is reduced when the homopolymers segregate to the appropriate domains of the ordered structure reducing the number of unfavorable segmental A/B contacts. The microdomains swell in order to accommodate the homopolymers resulting in transitions from one type of microstructure to another in the process¹.

Solutions of a commercially available diblock copolymer, polystyrene-polybutadiene(PS-b-PB) (SB-83, ~83,00g/mol) with homopolymer(s) were prepared in toluene. The homopolymer(s) was added to the diblock copolymer in order to obtain series of samples with different volume fractions of homopolymer but with lamellar morphology (i.e.,

$0.4 < f_{PS} < 0.6$). The solutions were spin-cast onto polished silicon wafers, covered with a native oxide layer. The uniform thin films were investigated by X-ray reflectivity to determine their total film thickness and by Neutron reflectivity to determine the lamellar spacing and the distribution of the labeled homopolystyrene. From the evaporated solutions, bulk samples were prepared and used to determine the d -spacing by Small Angle X-ray Scattering, and by Transition Electron Microscopy.

From this work, it was shown that the d -spacing increased upon increase in volume fraction of homopolymer in the blends. From our neutron reflectivity results it was suggested that the distribution of the homopolymer was mixed, with a part of homopolymer located in the middle of the domain and the rest completely solubilised in the domain. The effects of processing rate and thermal history were also studied. The mixed distribution disappeared upon annealing

[1] K. I. Winey *et al*, *Macromolecules*, **24**, (1991) 6182.

Investigation of the phase behaviour of block co-polymer gels containing inorganic salts

Ben Shaw

Sheffield University

The phase behaviour of aqueous gels of E-B-E (where E = polyethyleneoxide and B = polybutyleneoxide) block co-polymers containing inorganic salts has been investigated. Ternary mixtures of either E17B14E17 or E43B14E43 with water and hexachloroplatinic acid have been analysed using small angle x-ray scattering and rheology. The effect of shear alignment on such mixtures has also been investigated.

Fibre Diffraction Analysis of Fish Muscle Structure

John Squire, Carlo Knupp, Shing Mok, Jeffrey Harford

Biological Structure & Function Section, Biomedical Sciences Division, Imperial College, London SW7 2AZ.

The crossbridge power stroke on actin appears to involve a change in angle between the actin-attached motor domain and the neck region of the myosin heads. We are using X-ray diffraction methods applied to plaice fin muscle to define these structures *in situ*, to determine the kinetics of the transitions and to study structural aspects of its regulation by tropomyosin/ troponin. Studies involved are: (i) low-angle X-ray diffraction from resting muscle to define the arrangement and shape of the (M. ADP.Pi) myosin heads on their ordered structure on the thick filament backbone; (ii) low to medium-angle X-ray diffraction with 3D reconstruction of skinned fish muscle labelled with exogenous myosin S1 in the rigor and ADP-bound states; (iii) analysis of actin filament structure using X-ray diffraction data from 'steady state' resting and active muscle; and (iv) fast (1ms) time-resolved low-angle X-ray diffraction from contracting fish muscle during the rising phase of an isometric tetanus to study the kinetics of the crossbridge cycle. The head arrangement in relaxed fish muscle has been defined. Two different myosin head configurations on actin have been identified in active intact muscle. The shift of tropomyosin associated with regulation (steric blocking) has been confirmed and the role of troponin is being determined. Time-resolved X-ray diffraction has started to separate the weak and strong crossbridge states in the contractile cycle and to provide kinetic data between various states. Our best current estimate of the two actin-attached structural states in the fish muscle tetanus is that at the tetanus plateau there are about 46% of the heads in the low-force (mainly weak) state and about 28% of the heads in the high-force (strong) state with 26% detached and resetting.

Some Relevant Publications:

Harford, C J.J., Denny, R.C., Morris, E., Mendelson, R. & Squire, J.M. (1996) '3-D reconstruction from fibre X-ray diffraction patterns: Myosin-decorated actin filaments' *Fibre Diffraction Review*, **5**, 27-29.

Hudson, L., Harford, J.J., Denny, R.J. & Squire, J.M. (1997) "Myosin head configurations in relaxed fish muscle: resting state myosin heads swing axially by 150Å or turn upside down to reach rigor". *J. Mol. Biol.* **273**, 440-455.

Squire, J.M. & Morris, E.P. (1998) "A new look at thin filament regulation in vertebrate skeletal muscle" *FASEB J.* **12**, 761-771.

Squire, J.M., Cantino, M., Chew, M., Denny, R., Harford, J.J., Hudson, L. & Luther, P.K. (1998) "Myosin rod packing schemes in vertebrate muscle thick filaments" *J. Struct. Biol.* **122**, 128-138.

Squire, J.M. (1998) "Time-resolved X-ray Diffraction" in 'Current Methods in Muscle Physiology: Advantages, Problems and Limitations' IUPS Commission on Muscle Physiology (H. Sugi, Ed.) pp. 241-285. Oxford UP.

Harford, J.J., Cantino, M., Chew, M., Denny, R., Hudson, L., Luther, P., Mendelson, R., Morris, E. & Squire, J. (1998) "Myosin head configurations in equilibrium states of vertebrate skeletal muscle: heads swing axially or turn upside down between resting and rigor" In 'Mechanisms of Work Production and Work Absorption in Muscle' (Eds. H. Sugi & G.H. Pollack), pp. 297-308, Plenum Press, New York.

Harford, J.J., Denny, R.C., Hudson, L., Mendelson, R., Morris, E.P. & Squire, J.M. (1998) 'Myosin head configurations in relaxed, active, rigor and S1-labelled fish muscle; Evidence for characteristically distinct states' *Fibre Diffraction Review*, **7**, 45-50.

Cantino, M.E., Brown, L.D., Chew, M., Luther, P.K. & Squire, J.M. (2000) 'A-band architecture in vertebrate skeletal muscle: polarity of the myosin head array' *J. Mus. Res. Cell Motil.* **21**, 681-690.

Squire, J.M. (2000) 'Fibre and Muscle Diffraction' in 'Structure and Dynamics of Biomolecules' (E. Fanchon, E. Geissler, L-L. Hodeau, J-R. Regnard & P. Timmins, Eds), pp. 272-301. Oxford University Press, Oxford, UK.

Multipole wiggler 6.2 - A world class facility for the study of materials processing

N.J. Terrill

CLRC Daresbury Laboratory, Warrington, WA4 4AD

In collaboration with the University of Aberystwyth, Birkbeck College, the University of Cambridge and the University of Sheffield.

X-ray crystallography achievements have won more Nobel prizes than any other scientific discipline and over the last 50 years during which time X-rays have revolutionised the way in which we visualise and interpret the atomic structure of matter. However, advances in technology mean that scientists using the SRS today want sample cells that mirror real conditions and facilities that are able to follow reactions from one form of a material to another. Pressure, temperature, pH, humidity and the presence of corrosive atmospheres are all part of the current experimental trend.

The centrepiece of the new station, and its most significant development, is the gas multiwire detector combination based on the RAPID technology. Funded by the EPSRC, the curved position sensitive detector for measuring wide-angle scattering has a complex and rapid way of interpolating the diffraction peaks. This enables the detector to obtain a peak resolution of better than 0.06° and data in milliseconds. This timescale and statistical precision will be a much better match for the complementary small-angle scattering and spectroscopy techniques. The new facility will allow the study of reactions, chemical processing and solid state reactions with unprecedented accuracy and millisecond speeds.

The development of MPW 6.2 will keep the SRS at the cutting edge for at least seven years. It is anticipated that the new materials processing facility will be transferred to DIAMOND when the new synchrotron is built.

Microphase Separation of Block Copolymers: Confirmation of the universality of chi.

S.C.Turner*, S. Mai+, W. Mingvanish+, C. Chaibundit+, J.P.A. Fairclough*, A.J. Ryan*, F. Heatley+, C. Booth+, M.W. Matsen

* Chemistry Dept., University of Sheffield, Dainton Building, Brook Hill, Sheffield, S3 7HF

+ Chemistry Dept., University of Manchester, Oxford Road, Manchester M13 9PL

Dept. of Physics, University of Reading, Whiteknights, P.O. Box 220, Reading, Berkshire, RG6 6AF

X-ray diffraction study of human hair as a model of epithelial tissue

A.Vazina¹, P.Sergienko¹, V.Gerasimov¹, N.Lanina¹

I.Snigireva², A.Snigirev², M.Drakopoulos²

I.Dolbnya³, W.Bras³

(1)Institute of Theoretical and Experimental Biophysics of RAS, Russia

(2)ESRF, France

(3)DUBBLE CRG/ESRF Netherlands Organisation for Scientific Research

It has been known for some time that the molecular architecture at constant chain length and composition will dramatically influence the processes of microphase separation and crystallisation, and consequently the physical properties of block copolymers. The effect of block copolymer architecture on these important processes has been studied in terms of triblock and diblock copolymers of oxyethylene (E) / oxybutylene (B) systems.

Investigation of the microphase separation behaviour of EmBnEm, BnEmBn and EmBn systems was conducted using small angle scattering (SAXS) and rheology. These techniques yielded values for the temperature of the order-disorder transition (Todt) and domain spacings (d) in the ordered phases of the melt. The symmetry of the ordered phase behaviour could be deduced by a combination of 1D and 2D SAXS data analysis and rheology.

Values of the Todt for the BnEmBn triblock copolymers were 100 degrees lower if compared to EmBn diblock copolymers of identical composition and chain length, however they were 30 degrees higher when compared to diblock copolymers with half the triblock length. The d spacing results suggested that the triblock copolymers are 10% more stretched than their corresponding diblock counterpart. The phase diagram was evaluated in terms of chi_{RV} versus the volume fraction of the E or B component, where chi is the Flory Huggins interaction parameter, and RV is the length of the copolymer chain defined by the number of segments of given reference volume. The resultant phase diagrams were then compared with theoretical predictions.

X-ray diffraction investigations of human hair were carried out using SR of VEPP-3 (Novosibirsk, Russia), the X-ray generator with rotating anode GX-20 (Pushchino, Russia), ID22 and ID27 SAXS/WAXS of ESRF (Grenoble, France). We studied more than five hundred hair samples and carried out more than one thousand different experiments. In the experiments we collected hairs of different age donors from 1 to 92 years with their hair length from 3 to 1000 mm. Scalp-hair samples from donors of different regions with anthropologic 'pressure' and hair of patients from specialized hospitals were analyzed. The samples of hair were obtained from the following sources: Blokhin Scientific Center of Oncology, Department of Breast Tumor, Moscow; Mammological Institute, Altay Region; the 12 th Municipal Hospital, Department of Gastroenterology, Novosibirsk; Institute of Gynecology and Obstetrics, Novosibirsk B Phthisiology Clinic, Novosibirsk; the public school-pensionat of tundrian nenets, Chelyabinsk 4-th Branch Office of Biophysics Institute. The archaeological samples from Pazyryk mound of mountainous Altay were also investigated (undamaged state of hair samples is due to constancy of cold temperature conditions).

It was shown that the hairs demonstrate a classic X-ray pattern of fiber diffraction. X-ray patterns vary for different people by the presence or absence of diffuse ring of spacing 4.5 nm, the patterns were called 'ring' and 'no ring' respectively. A set of diffraction patterns from 'no ring' to 'ring' can be obtained from the hair of individual donor by scanning along the sample point by point from the root region to the tip. There are some donors, whose

hairs have not got the ‘ring’ X-ray patterns along the hair length which were called ‘ring free’ patterns. We were lucky to discover that a prolonged soaking of hairs in 1M CaCl₂ at pH 10-11 can transform the hair sample which initially gave a typical ‘ring free’ X-ray pattern in such way that it will be able to produce the ‘ring’ X-ray pattern. It was shown that there is correlation between significant quantities of major and trace elements of endogenous and exogenous origins: Ca-Br, Sr-Br, Ca-Sr.

We propose a two-component structural model of hair tissue, which consists of a flexible component of extracellular matrix (ECM) in series with an inflexible component of keratin intermediate filaments (IF). The weak diffuse arc at spacing 4.5 nm was interpreted as arising from interference between assemblies of flexible ECM units consisting of glycoproteins that can be either fibrillar and ribbon-like or random-coil in morphology and with low electron density.

The positively charged metals can transform the configuration of glycoprotein chains due to electrostatic interaction with multiple anion groups of polysaccharide chains and this results in the increasing of electron density. The structure of keratin intermediate filaments in hair tissue is invariable; the extracellular matrix structure is varied.

Thus, all of epithelial cells display extensive keratin filament frameworks around which the cell shape and polarity are defined. The primary cytoskeletal components *in vivo* regulate and affect the interaction of epithelial cells and extracellular matrix developing the oriented structure of the whole tissue and at the same time in which flexible extracellular matrix is transformed into fibrillar matrix. Our results propose also the regulatory role of metal content in matrix assembly.

So the hair tissue has to be considered as a structurally continuous organization providing the resistance to mechanical stresses externally applied to the tissue. Mutations that weaken this structural framework and any exogenous factors that change the extracellular matrix increase the risk of cell rupture and cause a variety of human disorders.

We are grateful to N.V. Polos'mak, V.A. Trounova, T.I. Savchenko, L.P. Osipova, Yu.P. Kolmogorov, A.N. Panpantonopulo and all colleagues from

Pushchino and Novosibirsk for providing hair samples.

The work was supported by RFBR grants No. 97-04-49237 and No. 99-02-17879.

X-ray scattering studies of Archaeological bone; tracking changes in mineral reorganisation

Wess T.J. Alberts I.L. Collins M. Pollard M. Nielsen- Marsh C. Hiller J. Drakopoulos M.

Centre for Extracellular Matrix Studies, Department of Biological Sciences, University of Stirling

The archaeological degeneration within the mineral component (calcium hydroxyapatite) of bone structures involves a number of processes probably most important of which are diagenesis, Ostwald ripening and pore formation. The exact nature of these rearrangements is poorly defined although alteration of the crystal habit is known to occur resulting in recrystallisation or accretion of bone mineral. These factors are essential in determining the dynamic changes in bone and archaeological preservation. Small angle x-ray scattering provides information on changes in crystallite organisation size and habit that are ideal for monitoring changes in bone porosity, diagenetic durability and ripening. Recent advances in technology now mean that these local variations can be monitored down to a micron length scale. We have combined measurements from standard x-ray scattering experiments with microfocus x-ray scattering experiments to establish the local changes that can occur to the size and shape of crystallites from a large variety of archaeological bones.

Crystallization of poly(oxyethylene)-b-poly(oxybutylene)/poly(oxybutylene) blends

J. T. Xu, S. C. Turner, A. J. Ryan

The University of Sheffield

Three poly(oxyethylene)-b-poly(oxybutylene) diblock copolymers with different chain length but the same volume fraction of poly(oxyethylene), E76B38, E114B56 and E155B78, were blended with pure poly(oxybutylene) to obtain different morphologies, such as lamellae, gyroid, cylinder, and sphere. The effect of chain length and morphology on the crystallization of poly(oxyethylene) segments in the blends were investigated using SAXS and DSC. It was found that the longer the chain length of the diblock copolymers, the larger was the extent of confinement in crystallization. On the other hand, the morphology also exhibited a marked influence on crystallization. The confinement of the morphology increased in the order: lamellae-cylinder-sphere.

Forthcoming Meetings

12th Annual Fibre Diffraction and Non-Crystalline Diffraction Workshop

July 2nd-4th, 2003, University of Cambridge

(Organised by Jane Crawshaw and John Squire)

[For further information and registration, see the web pages at www ccp13.ac.uk or contact tforsyth@ill.fr]

DARTS Bursaries

DARTS at Daresbury Laboratory has funded several bursaries for PhD students to attend the 12th Annual Fibre Diffraction and Non-Crystalline Diffraction Workshop at the University of Cambridge (see above and inside back cover). These bursaries will cover the cost of accommodation and registration and may include a contribution to travelling expenses. An application for a bursary can be made through the web pages at www ccp13.ac.uk

All bursary applications must be accompanied by the submission of a poster abstract to the Workshop.

Fibre Diffraction Review: Instructions to Authors

Submitted original papers, technical reports, mini-Reviews, comments/letters and meeting reports for inclusion in Fibre Diffraction Review are welcome.

Technical Reports:

These include presentations of the latest developments in CCP13 and other fibre diffraction/non-crystalline diffraction software and their scientific justification and also, for example, reports on developments at synchrotron beamlines used for fibre diffraction and non-crystalline diffraction studies.

Mini-Reviews:

These include summary presentations of the 'state of the art' in the structural analysis of particular fibrous or non-crystalline systems.

Original Papers:

These present previously unpublished results from fibre diffraction or small-angle scattering experiments using either X-ray, neutron or electron diffraction.

Expanded Poster-Prize Abstracts:

At each of the CCP13/ NCD Annual Workshops cash prizes are presented to the best poster presentations. The judges are always senior scientists in the field and are often from overseas. Winners of the Poster Prizes are invited to expand their abstracts into short papers for inclusion in Fibre Diffraction Review.

Refereeing:

All papers, of whatever category above, will be refereed by at least two people (from the CCP13 Committee or their nominated referees) and may be either (a) accepted as they stand, (b) returned for rapid revision, or (c) rejected. As well as their scientific content, papers will be judged on their clarity of presentation and the quality of their figures.

Meeting Reports:

Fibre Diffraction Review includes reports on relevant meetings and conferences which include an element of fibre diffraction or small-angle scattering and which will be of general interest to our readers. Such reports will often be solicited by the Editor from known meeting participants. Other potential contributors to this part of the Journal should contact the Editor prior to writing their report.

Comments/Letters:

Feedback from readers about CCP13, about the NCD community and about the Journal itself are welcome. These could be in the form of comments or letters to the Editor. Suitable contributions will be published in the Journal.

Advertisements:

Industrial/commercial adverts of interest to our readers are welcome. Potential advertisers should contact the Editor for details of current rates.

Submission:

Contributions should be sent to the Editor before the annual deadline (November 30th) for each issue. Contributions submitted after this date may be held over for the following issue.

Colour illustrations are welcome and are included without charge. Contributions should be submitted both in hardcopy (THREE complete copies) and in electronic format to the Editor (j.squire@ic.ac.uk).

Text should be in Word 6 format and illustrations should be submitted as separate files at high resolution in TIFF format.

References should be in the format specified for *J. Molecular Biology*, and should be complete with titles.

Reprints:

It is not economic for us to produce reprints of articles. However, in future, papers will be made available on the CCP13 website in downloadable pdf format.

Those wishing to purchase extra copies of the whole Journal should contact the Editor to find out costs.

Editor's Address:

Professor John M. Squire,
Head, Biological Structure and Function Section,
Biomedical Sciences Division,
Imperial College of Science, Technology & Medicine,
London SW7 2AZ, UK.

Editor 'Fibre Diffraction Review' (ISSN 1463-8401).

12th Annual Fibre Diffraction and Non-Crystalline Diffraction Workshop

2nd - 4th July 2003

Fitzwilliam College Cambridge

Speakers include:



A. H. Windle FRS
J. Blackwell (tbc)
J. Bordas (tbc)
J. Crawshaw
A. M. Donald
V. T. Forsyth
P. Fratzl (tbc)
R. Ganeshalingam
K. Gardner
A. He
T. Irving
T. Lodge
K. Meek
K. Namba
S. Perkins
L. Serpell

Cambridge, UK
Cambridge, UK
LLS, Spain
Cambridge, UK
Cambridge, UK
ILL, France/ Keele, UK
Leoben, Austria
Imperial College, UK
DuPont, USA
Imperial College, UK
Illinois, USA
Minnesota, USA
Cardiff, UK
Osaka, Japan
UCL, London
Cambridge, UK

For further information and registration,
see the web pages at
www ccp13.ac.uk

or contact Jane Crawshaw (jc10027@hermes.cam.ac.uk)
Supported by CCP13, DARTS and Daresbury Laboratory.

Useful World Wide Web addresses (URL)

CCP13	http://www ccp13 ac uk
NCD	http://www ccp13 org
SRS	http://www srs dl ac uk/NCD
DARTS	http://www srs ac uk/SRS